AD-A099 079 ROME AIR DEVELOPMENT CENTER GRIFFISS AFB NY F/G 17/9
NULL FILTER MOBILE RADAR (NFMRAD): CONCEPT VERIFICATION,(U)
OCT 80 W BUCHANAN, H GODLEWSKI, F S HOLT
UNCLASSIFIED RADC-TR-80-306 NL

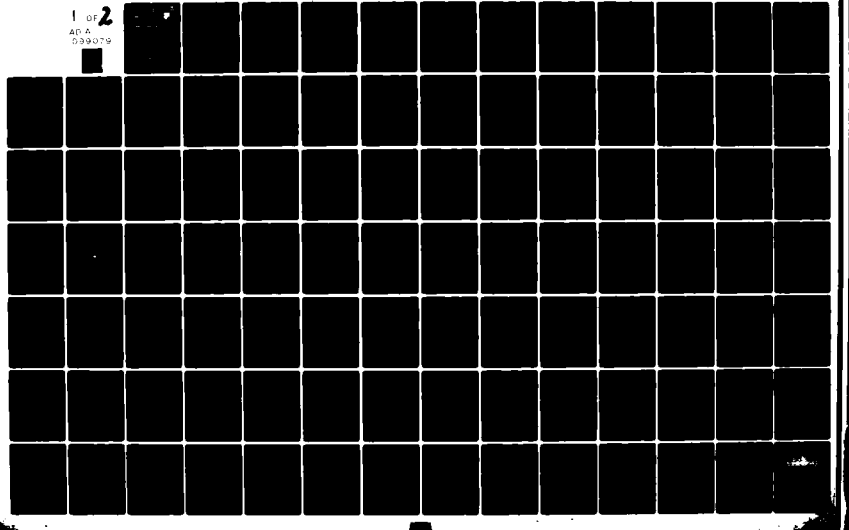

LEVEL II

12

14

RADC-TR-80-30

In-House Report

11 Oct 80

12 158

6

NULL FILTER MOBILE RADAR (NFMRAD): CONCEPT VERIFICATION,

D

W./Buchanan Capt, USAF
H. /Godlewski 1/Lt, USAF
F. Sheppard/Holt

16 460P 17 15

ROME AIR DEVELOPMENT CENTER
Air Force Systems Command
Griffiss Air Force Base, New York 13441

309050

This report has been reviewed by the RADC Public Affairs Office (PA) and is releasable to the National Technical Information Service (NTIS). At NTIS it will be releasable to the general public, including foreign nations.

RADC-TR-80-306 has been reviewed and is approved for publication.

APPROVED: John K. Schindler

JOHN K. SCHINDLER, Assistant Chief
EM Techniques Branch
Electromagnetic Sciences Division

APPROVED: Allan C. Schell

ALLAN C. SCHELL, Chief
Electromagnetic Sciences Division

FOR THE COMMANDER: John P. Huss

JOHN P. HUSS
Acting Chief, Plans Office

SUBJECT TO EXPORT CONTROL LAWS

This document contains information for manufacturing or using munitions of war. Export of the information contained herein, or release to foreign nationals within the United States, without first obtaining an export license, is a violation of the International Traffic in Arms Regulations. Such violation is subject to a penalty of up to 2 years imprisonment and a fine of $100,000 under 22 U.S.C 2778.

Include this notice with any reproduced portion of this document.

If your address has changed or if you wish to be removed from the RADC mailing list, or if the addressee is no longer employed by your organization, please notify RADC (EEC) Hanscom AFB MA 01731. This will assist us in maintaining a current mailing list.

Do not return this copy. Retain or destroy.

Unclassified

SECURITY CLASSIFICATION OF THIS PAGE (When Data Entered)

REPORT DOCUMENTATION PAGE	READ INSTRUCTIONS BEFORE COMPLETING FORM
1 REPORT NUMBER RADC-TR-80-306	2 GOVT ACCESSION NO AD-A099079
3 RECIPIENT'S CATALOG NUMBER	
4 TITLE (and Subtitle) NULL FILTER MOBILE RADAR (NFMRAD): CONCEPT VERIFICATION	5 TYPE OF REPORT & PERIOD COVERED In-House
	6 PERFORMING ORG. REPORT NUMBER
7 AUTHOR(s) W. Buchanan, Capt, USAF H. Godlewski, 1/Lt, USAF F. Sheppard Holt	8 CONTRACT OR GRANT NUMBER(s)
9 PERFORMING ORGANIZATION NAME AND ADDRESS Deputy for Electronic Technology (RADC/EEC) Hanscom AFB Massachusetts 01731	10 PROGRAM ELEMENT, PROJECT, TASK AREA & WORK UNIT NUMBERS 62702F 46001502
11 CONTROLLING OFFICE NAME AND ADDRESS Deputy for Electronic Technology (RADC/EEC) Hanscom AFB Massachusetts 01731	12 REPORT DATE October 1980 13 NUMBER OF PAGES 162
14 MONITORING AGENCY NAME & ADDRESS (if different from Controlling Office)	15 SECURITY CLASS. (of this report) Unclassified 15a DECLASSIFICATION/DOWNGRADING SCHEDULE

16 DISTRIBUTION STATEMENT (of this Report)

Approved for public release; distribution unlimited.

17 DISTRIBUTION STATEMENT (of the abstract entered in Block 20, if different from Report)

18 SUPPLEMENTARY NOTES

19 KEY WORDS (Continue on reverse side if necessary and identify by block number)

Foliage
Penetration
Mobile
Radar

20 ABSTRACT (Continue on reverse side if necessary and identify by block number)

The Null Filter Mobile Radar (NFMRAD) concept is described, and the need for narrow-band digital filters that can distinguish between positive and negative frequencies is explained. Two different procedures for realizing complex bandpass and bandstop filters of the infinite impulse response type are described, and their properties evaluated. A procedure for generating complex bandpass and bandstop filters of the finite impulse response type is also described, and the particular applicability of these filters to NFMRAD is discussed. The experimental NFMRAD system is described, and the field

DD FORM 1 JAN 73 1473 EDITION OF 1 NOV 65 IS OBSOLETE

Unclassified

SECURITY CLASSIFICATION OF THIS PAGE (When Data Entered)

20. Abstract (Continued)

installation and test program is explained. A ground based experiment using a truck traveling at about 30 mph (13.4 m/s) as the radar platform is described. Under these experimental conditions, the performance of NFMRAD is computed theoretically and compared to expected performance of systems using Chebyshev and uniform-fed antenna arrays with and without filters. Real-time processing tasks such as antenna pattern synthesis, Doppler filtering, and detection processing are described. Hardware performance and a functional description of the radar hardware is presented. NFMRAD transmitter, receiver, and digital processing specification are reviewed, and experimental system restrictions are made clear. The NFMRAD system is found to have its greatest superiority over other systems for cases in which the differences between the radial velocities of the target and the local clutter is not large.

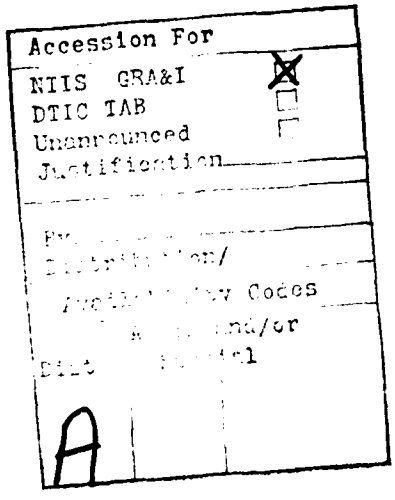

Preface

The authors are indebted to the following individuals for their contributions during the course of this work:

Dr. William B. Goggins for original system concept and system design work.[1]

Dr. August Golden for system design, software development, consultation, and continued project guidance.

Mr. Radames Gonzalez, Jr. for system fabrication and support during field testing.

Mr. L. McWilliams for artwork and drafting done in support of this report, and for his perserverance throughout field testing.

Dr. J. K. Schindler and Dr. J. Leon Poirier for providing guidance, suggestions, and relevant questions throughout this effort.

TSgt Dion Shannon for system fabrication, field testing support, and the ADC alignment procedure.

Mr. Richard Taylor for development of efficient real-time radar data processing software which made system realization possible, and for his continued support and interest.

---

1. Goggins, W.B., Jr., Sletten, C.J., and Holt, F.S. (1974) New concepts in AMTI radar: Nulling effect of Doppler filter/multielement horn array, Microwave J. 17(No. 1):29-33.

Contents

1. INTRODUCTION 11

2. THE NFMRAD CONCEPT AND EXPERIMENTAL SYSTEM 15

2.1 The Null Filter Mobile Radar (NFMRAD) 15
2.1.1 Concept Description and Filter Requirements 15
2.1.2 Optimum Receive Antenna Pattern 16
2.2 Experimental Radar System 22
2.3 Theoretical Investigations Relative to the NFMRAD Experiment 29
2.3.1 The NFMRAD Experiment 29
2.3.2 Optimization of FIR Filters 30
2.3.3 Comparison With Other Systems 31

3. NFMRAD RF HARDWARE 33

3.1 Transmitter 35
3.1.1 RF Sources 35
3.1.2 Generation of Carrier 36
3.1.3 Transmit Pulse Formation 38
3.1.4 Traveling Wave Tube Amplification 43
3.1.5 Transmit Antenna 43
3.1.6 Diagnostic Facilities 46
3.1.7 Summary of Transmitter Specifications 47
3.2 Receiver 50
3.2.1 Receive Antenna 50
3.2.2 Receiver Front End 53
3.2.3 Receiver Gain Control 54
3.2.4 IF Bandpass Characteristics and Detection of Moving Targets 56
3.2.5 Summary of Receiver Specifications 60

Contents

4. RECEIVER DIGITAL HARDWARE 61

4.1 NFMRAD (AMTI) System Timing 64
4.2 Ultra-High-Speed Sample and Hold 67
4.3 Ultra-High-Speed Analog-to-Digital Converter 67
4.4 Radar Data Buffer 68
4.4.1 Mantissa Buffer 71
4.4.2 Base 2 Exponent Buffer 72
4.5 Data Format Conversion Logic 72
4.5.1 Analog-to-Digital Converter (Input and Output Specifications) 73
4.5.2 8-Bit Inverted Offset Binary Format Conversion to 8-Bit Sign/Magnitude Format 73
4.5.3 8-Bit Sign/Magnitude Mantissa with Positive 3-Bit Base 2 Exponent Conversion to 16-Bit Floating Point Format with Base 16 Exponent 74
4.5.4 Normalization of 16-Bit Floating Point Word 77
4.6 Input/Output Scroll (IOS) Interface 77
4.6.1 16-Bit Normalized Floating Point Word Transfer from Radar to IOS Interface 77
4.6.2 Radar/MAP-300 IOS Interface Control and Timing Signals 78
4.6.3 Data Status Indicator 79
4.7 Receiver Simulator Hardware 80

5. SYSTEM SOFTWARE 83

5.1 CSP-30/MAP-300 System Initialization Software 83
5.2 CSP-30/MAP-300 Real-Time Operation 84
5.3 Maintenance Software 85
5.4 MAP Software 86
5.4.1 MAP Initialization 86
5.4.2 MAP Real-Time Processing 87
5.4.3 MAP Software Test Mode 90
5.5 MAP-300 Double Buffered Input 90

6. FIELD INSTALLATION AND TESTS 93

6.1 Experimental Set-Up 94
6.1.1 Van Installation 94
6.1.2 Remote Test Facility 94
6.1.3 Enhanced Radar Target 97
6.1.3.1 Pickup/Corner Reflector Combination Target 97
6.1.3.2 Flat Plate Reflector 97
6.2 Field Tests 100
6.2.1 Measurement of Two-Way Antenna Patterns 102
6.2.2 Measurement of Doppler Filter Characteristic 105
6.2.3 Target Detection Threshold Voltage Determination 107
6.2.4 NFMRAD (AMTI) P_d Determination 110

7. EXPERIMENTAL RESULTS AND CONCLUSIONS 116

7.1 Two-Way Antenna Patterns 116
7.1.1 Uniformly Weighted Antenna Pattern 116
7.1.2 NFMRAD Antenna Pattern 117
7.2 Doppler Filter Characteristic 118

Contents

7.3 Threshold Voltage Determination 118
7.4 Receiver I/O Characteristic 118
7.5 Receiver Noise Histogram 120
7.6 Preliminary Conclusions and Future Direction 121

REFERENCES 123

APPENDIX A: Complex Recursive Infinite Impulse Response (IIR) Digital Filters 125

APPENDIX B: Complex Nonrecursive Finite Impulse Response (FIR) Digital Filters 137

APPENDIX C: Control Panel Operational Range Equations 141

APPENDIX D: ADC Alignment Procedures 145

APPENDIX E: System Component Identification 159

Illustrations

1. Example of Doppler Clutter Interference 14

2. NFMRAD Antenna Patterns, Filter Power Transfer Functions, and Clutter Distributions 17
   (a) Transmit Antenna Pattern
   (b) Doppler Filter Power Transfer Function
   (c) Bandstop Filter Power Transfer Function
   (d) Optimum Receive Array Pattern
   (e) Composite Doppler Filter Characteristic
   (f) Clutter Power vs Azimuth After Filtering but Before NFMRAD Processing
   (g) Clutter Power vs Azimuth After Filtering and NFMRAD Processing
   (h) Two-Way NFMRAD Antenna Pattern

3. Simplified NFMRAD System 23

4. NFMRAD/AMTI Experimental Radar System 23

5. NFMRAD/AMTI Transmit and Receive Antennas 24
   (a) Transmit and Receive Array (Front View)
   (b) Transmit Antenna (Three Views)
   (c) Eight-Element Receive Array (Side View)
   (d) Eight-Element Receive Array (Top View)

6. Radar Van and Target Tracks for NFMRAD Experiment (Diverging Case) 30

7. Improvement of NFMRAD System Over a System Using Uniform Patterns on Both Transmit and Receive (a) Without Filters, (b) With Filters 32

8. Improvement of NFMRAD System Over a System Using Chebyshev Array Patterns on Both Transmit and Receive (a) Without Filters, (b) With Filters 32
9. NFMRAD System Functional Breakdown 34
10. Simplified Diagram of NFMRAD Receiver and Transmitter 35
11. Typical Microwave PIN Diode Switch 39
12. Timing Diagram: Transmit Pulse Formation 41
13. Diode Switch Firing Circuitry 42
14. TWTA Gain Characteristic 43
15. Transmitter Horn 44
16. Theoretical and Experimental Transmit Horn Azimuth Power Patterns 45
17. Experimental Transmit Horn Elevation Power Pattern 45
18. Doppler Target Simulator 47
19. NFMRAD Transmitter Subsystem 49
20. Theoretical and Experimental Receive Horn Single Element Directivity Pattern 50
21. Illustration of Relationship for Derivation of Single Receive Element Pattern 51
22. Theoretical and Experimental Azimuth Power Pattern for Receiver Eight-Element Array 53
23. Receiver Front End 54
24. Diagram of I and Q Outputs with Respect to Reference Signal Vector 59
25. NFMRAD Receiver Subsystem 62
26. Receiver Realization 63
27. Timing Signal Binary Counter Outputs 65
28. ADC Board Timing Signals 68
29. Mantissa and Exponent Shift Register Buffer with 8-Bit Wide Data Multiplexer 70
30. Radar Receiver Mantissa Buffer (256 8-Bit Words) 71
31. Radar/IOS Interface Control and Timing Signals 78
32. Receiver Digital Hardware 81
33. Receiver Simulator Hardware 81
34. Double Buffered Input Timing 91
35. Radar Van Installation with Generator 95
36. Radar Equipment Layout (Top View of Van) 95
37. Radar Equipment Layout (End View of Van) 96
38. Floating Radar Platform with Shocks and Sway Braces 96
39. Base Plate Shocks 97

40. Sway Braces 98
41. Remote Test Facility 99
42. Enhanced Radar Target 99
43. Corner Reflector 100
44. Flat Plate Reflector 101
45. Field Site Used for Antenna Pattern Measurements (Top View) 101
46. Field Site Used for Antenna Pattern Measurements (Side View) 102
47. Field Site Used for Measurement of Doppler Filter Characteristic (Top View) 103
48. Field Site Used to Determine NFMRAD {AMTI} Threshold Voltages and NFMRAD {AMTI} P_d Curves (Top View) 108
49. Taxiway Whiskey Divided into Tape Records 113
50. AMTI Two-Way Azimuth Pattern (Theoretical and Experimental) 117
51. NFMRAD Two-Way Azimuth Pattern (Theoretical and Experimental) 118
52. Doppler Filter Characteristic (Theoretical and Experimental) 119
53. Receiver I O Chararacteristic 119
54. Receiver Noise Histogram 120
55. Effect of Uniformly Distributed Error in the Scattering Matrix on the Null Region of Receive Pattern 122
A1. Power Transfer Loss Function of a Cayer C04a Type Filter 127
A2. Power Transfer Functions of Filters Used to Realize an Asymmetrical Single-Band Lowpass Filter 129
A3. Power Transfer Functions of Filters Used to Realize an Asymmetrical Single-Band Lowstop Filter 131
A4. IIR Digital Filter Response Times 135
B1. Specification of Filter Response Values for BP 33-3-2 F.I.R. Filter 139
C1. Radar Control Panel 141
D1. 8-Bit ADC Alignment Configuration 146
D2. Receiver Digital Hardware (Backplane Connector Panel) 147
D3. 8-Bit ADC Assembly 148
(a) Pin Locations (Top View)
(b) Calibration Adjustments (Side View)
D4. 8-Bit ADC Calibration 150
D5. LED Display 150
D6. 4-Bit ADC Assembly 152
D7. 4-Bit ADC Bias Adjustment 154
D8. ADC Dynamic Test Configuration 156

Illustrations

E1. Receiver Transmitter Equipment Racks 162
(a) Receiver
(b) Transmitter

E2. CSP-30/MAP-300 Equipment Racks 162
(a) CSP-30
(b) MAP-300

Tables

1. NFMRAD AMTI System Characteristics Summary 26
2. IF Attenuation as a Function of Base 2 Exponent 56
3. Timing Command Sequence 66
4. System Timing Signals 67
5. Mantissa Buffer Data Multiplexer Pecking Order 69
6. Datel ADC Output Format 73
7. Sign/Magnitude Format 74
8. Radar Base 2 Floating Point Format 75
9. MAP Base 16 Floating Point Half-Word Format 76
10. Radar/IOS *Interface Control and Timing* Signals 79
11. Receiver Digital Circuit Card Functions 82
12. Tape Record 105
B1. FIR Filters Used in NFMRAD Investigation 139
C1. Radar Operating Range Mode 142
C2. $DCBA_{10}$ Equivalent for Range Calculations 143
D1. 4-Bit ADC Output 153
D2. ADC to Digital Hardware Backplane Cable List 155

Null Filter Mobile Radar (NFMRAD): Concept Verification

I. INTRODUCTION

Pulse-Doppler radars may be used in a side-looking airborne configuration for the detection of slow-moving stand-off targets embedded in clutter (that is, foliage). Such a radar experiences interference from this background clutter. Clutter signals received through the mainbeam may be distinguished from a target of interest by appropriate Doppler filtering. This is possible, since the mainbeam clutter returns possess near-zero Doppler and can be effectively separated from a moving target signal possessing a Doppler frequency shift. However, clutter received through receive antenna sidelobes possesses motion relative to the moving radar platform. This sidelobe clutter can easily possess a Doppler equal to that of a moving target in the receive antenna mainbeam. Doppler filtering of this sidelobe clutter signal will not separate it from the target Doppler signal received through the mainbeam. Hence, with sufficient power, the sidelobe clutter signal can obscure the mainbeam target; thus, moving target detection is rendered difficult or impossible. The detection of a moving target will be made where no such target exists in the mainbeam.

This phenomenon results from the mechanism which generates a Doppler frequency and may be referenced to the forward motion of the radar platform by the following relation:

(Received for publication 3 October 1980)

$$f_d = \frac{2V_o}{\lambda} \cos \theta$$

where λ is the wavelength of the radar frequency; V_o is the forward velocity of the airborne radar platform; θ is measured from the line of forward motion of the radar platform, and f_d is the resultant Doppler frequency. Targets with motion parallel to the radar platform and with position in the receiver mainbeam would be at a θ angle of 90° and produce a zero Doppler frequency in their radar returns.

Targets illuminated by the mainbeam and producing nonzero Doppler frequencies are following courses nonparallel to that of the radar platform; hence they possess radial velocities with respect to the radar platform. A problem arises when ground clutter possesses a radial velocity with respect to the moving radar platform. This is true of ground clutter received through the receive antenna sidelobes.

To illustrate this matter, assume that the radar platform possesses a forward velocity of 180 miles per hour (mph) (80 meters per second (m/s)). A signal is being received in an antenna sidelobe from a large patch of ground clutter at a bearing of roughly 95° from the radar platform course heading. The return signal power would be large and detectable above the radar systems minimum discernible signal level. In addition, the sidelobe signal Doppler would be 14 m/s λ. For a radar wavelength of 1.8 ft (0.6 m or 500 MHz), the Doppler frequency of the return would be 23.3 Hz, indicating a target moving away from the radar platform with a radial speed of 31.3 mph (14 m/s).

The returned signal Doppler frequency may also be referenced to radial velocity from the moving radar platform with the following relation:

$$f_d = \frac{2V_r}{\lambda}$$

where V_r is the apparent target radial velocity from the moving radar platform. A moving target in the mainbeam may possess the same radial velocity as sidelobe clutter:

$$V_r = V_o \cos 80^{\circ} .$$

Such a target, embedded in foliage, could be traveling away from the radar platform at 31.3 mph (14 m/s). The course of the mainbeam target would be 80° from that of the radar platform, with a velocity of approximately 32 mph (14.2 m/s) on its own course.

Examining the two cases illustrated above highlights the problem from the radar reception standpoint. With reception of clutter alone, an erroneous detection of a target may be made. With the reception of the discrete clutter at a bearing from the radar line of travel of 95^{o}, and the simultaneous presence of the moving target in the receive antenna mainbeam, detection of the mainbeam target is rendered a difficult if not impossible task. Figure 1 illustrates the situation of clutter at 95^{o} and the above target on a course 80^{o} from that of the radar platform.

One possible answer to this sidelobe clutter problem is the use of a narrow-beam, low-sidelobe high-gain antenna. Unfortunately, this approach suffers from physical unmanagability. The radar operating frequencies that afford good foliage penetration performance lie well below 900 MHz.[2] The antenna apertures required to realize a narrow mainbeam become prohibitively large at these optimum foliage penetration frequencies, and would result in an antenna size physically unmanageable in a side-looking airborne configuration.

One approach to the solution of the Doppler clutter problem is the use of antenna receive-pattern nulls placed or stirred such that the interfering clutter is attenuated. This technique could be used in conjunction with mainbeam target Doppler filtering to reveal the presence or absence of a tactical target in the mainbeam. It is for the investigation of this antenna null filtering technique that the Null Filter Mobile Radar (NFMRAD) project has been conducted.

NFMRAD is a proof-of-concept investigation. In any proof-of-concept program, economy of performance in the attainment of new information is important. To this end NFMRAD has been designed. Hardware design in both the areas of radio frequency and digital signal processing technology has been directed toward implementation of one antenna null and one Doppler filter with a similar design of processing software.

Rather than implementing NFMRAD in a costly airframe design, a truck-based moving platform has been used. This NFMRAD configuration is similar to that of a side-looking Airborne Moving Target Indicator (AMTI) on a moving platform. The moving system may be field tested against another moving target (truck), greatly simplifying field testing while addressing the objective of the most economic experimental investigation possible. Additionally, facility exists in the design for comparison of NFMRAD performance to that of conventional standoff, side-looking AMTI without the null filtering capability.

NFMRAD, as an experimental system, has been implemented in X-band. In keeping with constraints of simplicity and economy, the X-band implementation

---

2. Brown, Dr. Gary S., and Curry, William J. (1979) An Analytical Study of Wave Propagation Through Foliage, RADC-TR-79-359.

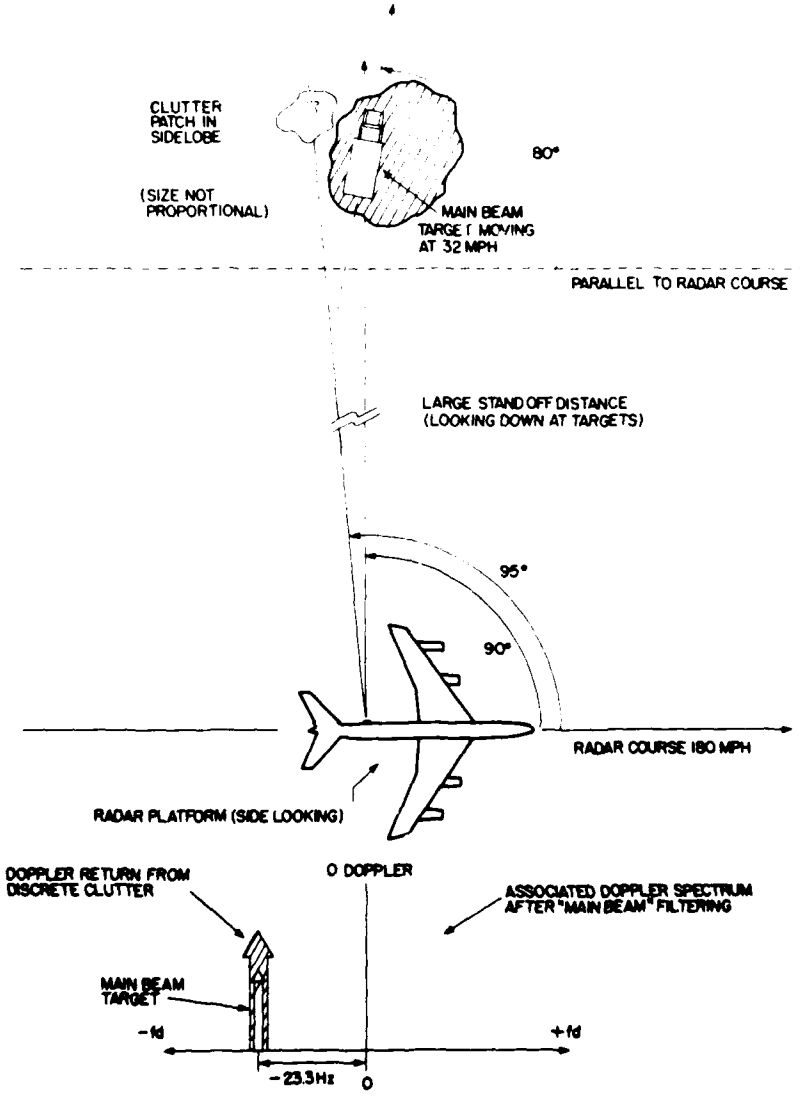

Figure 1. Example of Doppler Clutter Interference

affords the use of readily available components within a compact experimental configuration. This again not only simplifies the design of the experimental radar platform but also eases field testing requirements.

Section 2 of this report covers in detail the theoretical aspects of the NFMRAD concept. Sections 3 and 4 describe the hardware design, both radio frequency and digital circuitry. Section 5 covers the design of supporting system software, while Section 6 deals with the experimental system field installation and testing. Results and conclusions are presented in Section 7 of the report.

2. THE NFMRAD CONCEPT AND EXPERIMENTAL SYSTEM

2.1 The Null Filter Mobile Radar (NFMRAD)

2.1.1 CONCEPT DESCRIPTION AND FILTER REQUIREMENTS

The NFMRAD system operates from a moving platform and uses Doppler bandpass and bandstop filters together with null control in the receive antenna array pattern to reduce clutter return when detecting a target that is in motion relative to the ground. For a radar moving with velocity v relative to the ground, there is a simple relationship between the clutter Doppler frequency shift Δf_d and the azimuth angle θ given by the formula

$$\Delta f_d = \frac{2v \cos \theta}{\lambda}$$

where λ is the wavelength of the transmitted frequency and θ is measured clockwise relative to the direction of motion of the NFMRAD platform. By means of this relationship, all Doppler filter plots between the maximum and minimum clutter Doppler frequency shifts ($2v/\lambda$ and $-2v/\lambda$) can be exhibited as functions of azimuth angle θ, rather than clutter Doppler frequency shift. Throughout this report, we will assume that the clutter distribution is uniform in θ. The Doppler filter patterns in θ thus represent the clutter distribution as modified by the filters.

The NFMRAD system converts to baseband, using inphase and quadrature mixing. The received signal thus processed will contain only the Doppler frequency shifts; these will be positive or negative according to whether the objects producing the reflected signals are approaching or receding relative to the radar. Discrimination between these two cases is possible because both inphase and quadrature information is present. To quantitatively measure the frequency shifts and hence the relative velocities, bandpass filters must be designed that can measure both positive and negative frequencies and distinguish between them. At the same time, to discriminate against signals due to ground clutter, it is

necessary to design bandstop filters which pass all but a single band of frequencies that may be centered on either a negative or a positive frequency. If a filter has a real voltage transfer function (that is, real on the real axis), the power transfer function as a function of frequency must be symmetric with respect to zero frequency, and the filter cannot discriminate between positive and negative frequencies. What is needed is a filter that will produce a single passband (or stopband) that is not symmetric with respect to zero frequency. The voltage transfer function for such a filter will necessarily be complex (that is, complex on the real axis).

In the operation of NEMRAD, many different filters and many different antenna array patterns need to be implemented, and the only practical way this can be accomplished is by digital processing. Two general types of complex digital filters have been considered. One type has an infinite impulse response (IIR) and is realized by means of a recursive algorithm. The second type has a finite impulse response (FIR) and is realized by means of a nonrecursive algorithm.

2.1.2 OPTIMUM RECEIVE ANTENNA PATTERN

In the NEMRAD system concept, the spatial azimuth sector is covered by a set of fixed transmitting beam positions, and the Doppler frequency shift range is covered by a set of bandpass filters. Figure 2(a) shows a typical transmit antenna pattern and Figure 2(b) shows a typical Doppler bandpass filter power transfer function both plotted with θ as abscissa. For each transmitting beam position there is also an associated bandstop Doppler filter than blanks the clutter return from the main lobe of the transmitted pattern. Figure 2(c) shows the bandstop filter power transfer function corresponding to the transmit antenna pattern of Figure 2(a).

Assume there is a target located at the peak of the main lobe of the transmit antenna pattern of Figure 2(a) with radial velocity (relative to the NEMRAD platform) such that its return signal has a Doppler frequency shift that lies in the passband the Doppler filter of Figure 2(b). Then for the transmit antenna pattern of Figure 2(a) and the filter power transfer functions of Figures 2(b) and 2(c), there exists a unique receive antenna array pattern that is optimum in the sense that it maximizes the ratio of the power of the received target signal to the total clutter power.[3, 4] All optimum received patterns that appear in this report were computed [illegible]

---

3. Cherry, D.K. and Tseng, F.I. (1965) Gain optimization for arbitrary antenna arrays, IEEE Tr. AP AP-13(No. 6):973.

4. Drane, C.J., Jr. and McIlvenna, J.F. (1969) *Gain Maximization and Controlled Null Placement Simultaneously Achieved in Aerial Array Patterns,* AFCRL-69-0257.

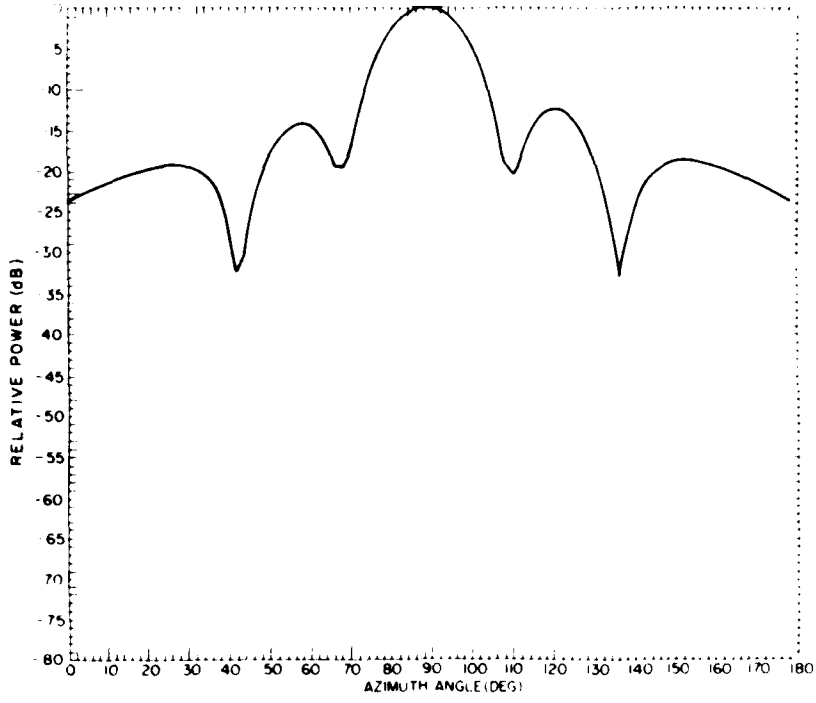

(a) Transmit Antenna Pattern

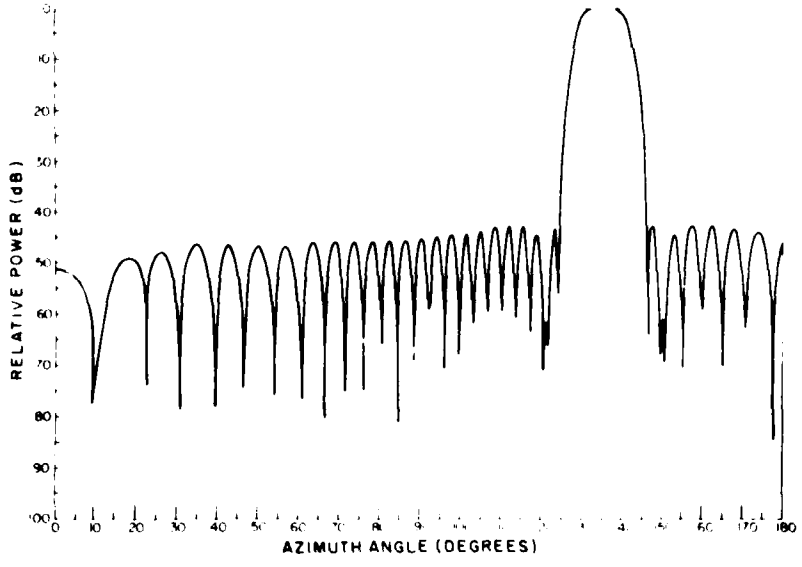

(b) Doppler Filter Power Transfer Function

Figure 2. NFMRAD Antenna Patterns, Filter Power Transfer Functions, and Clutter Distributions

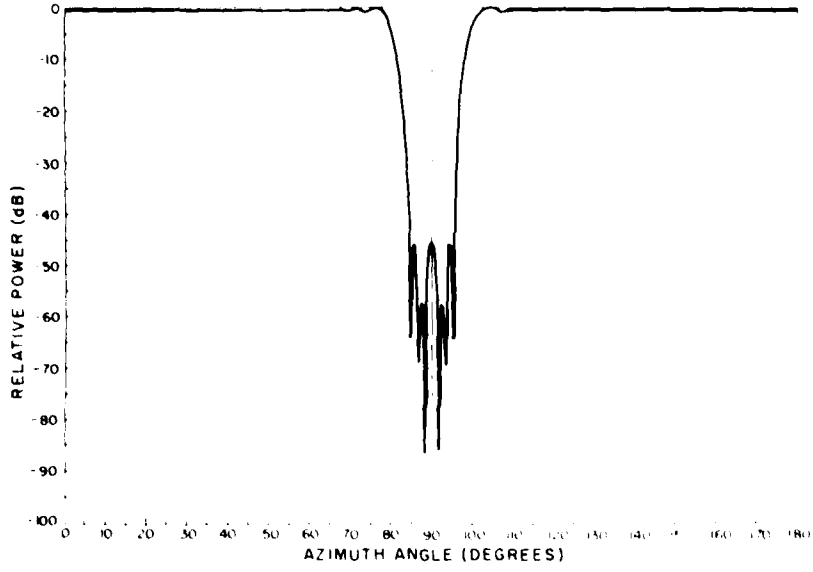

(c) Bandstop Filter Power Transfer Function

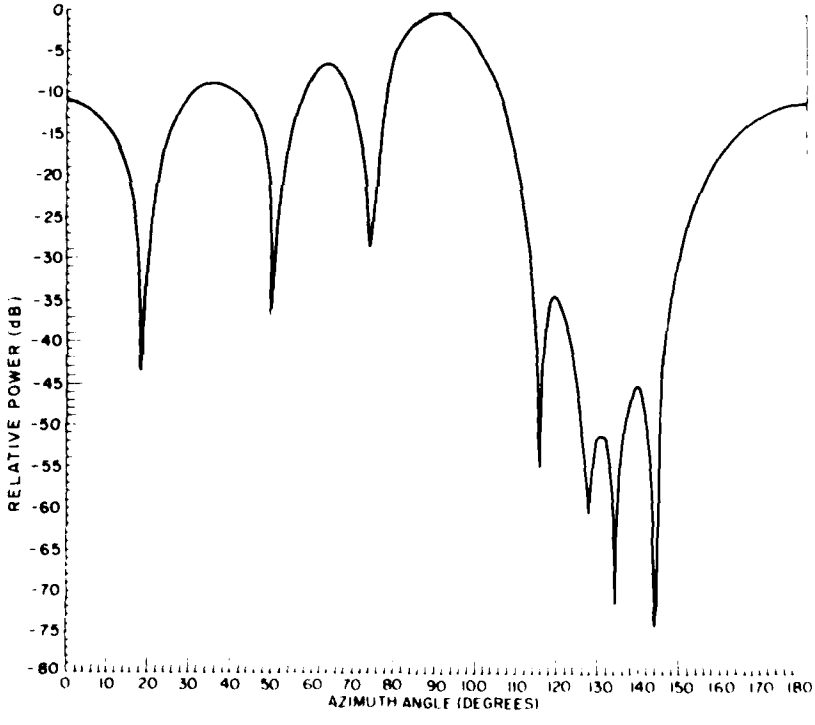

(d) Optimum Receive Array Pattern

Figure 2. NEMRAD Antenna Patterns, Filter Power Transfer Functions, and Clutter Distributions (Cont.)

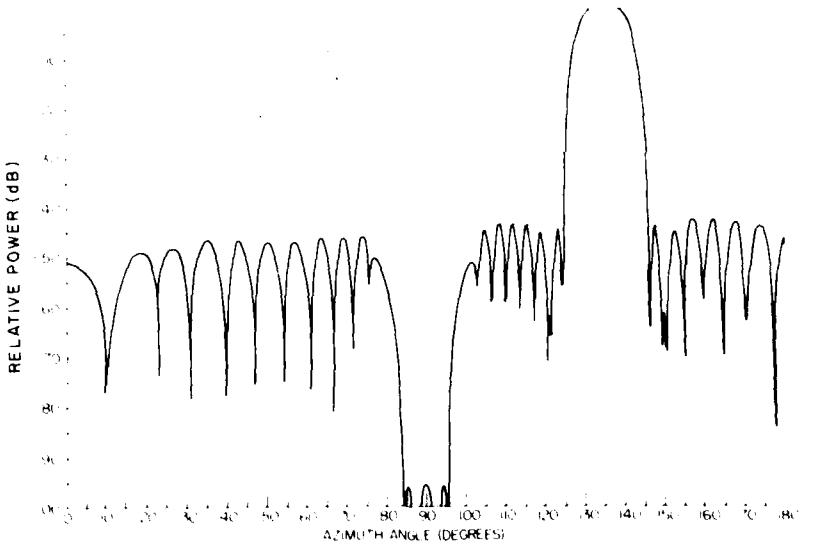

(e) Composite Doppler Filter Characteristic

Figure 2. NFMRAD Antenna Patterns, Filter Power Transfer Functions, and Clutter Distributions (Cont.)

CDC-6600, using modifications of a FORTRAN program devised by Goggins and Schindler.[5] Figure 2(d) shows a typical optimum receive antenna array pattern for the present case. It is characteristic of this optimum pattern that it has a null region in the angular sector whose clutter Doppler return lies in the passband of the Doppler bandpass filter.

The power filter transfer function for the composite filter obtained by cascading the bandpass filter (Figure 2(b)) with the bandstop filter (Figure 2(c)), is shown in Figure 2(e). A plot of clutter power vs angle, as observed after illumination of the assumed uniformly distributed clutter by the transmit antenna pattern followed by filtering but before receive antenna processing, is shown in Figure 2(f). The product of this distribution of clutter power vs angle with the NFMRAD receive antenna pattern represents the distribution of clutter power that is ultimately present in the NFMRAD system, and is shown in Figure 2(g). The integral of the clutter distribution shown in Figure 2(g) is a measure of the total clutter power in the NFMRAD system.

---

5. Goggins, W.B., Jr. and Schindler, J.K. (1974) Processing for Maximum Signal-to-Clutter in AMTI Radars, pp. 15-21, AFCRL-TR-74-0577, AD

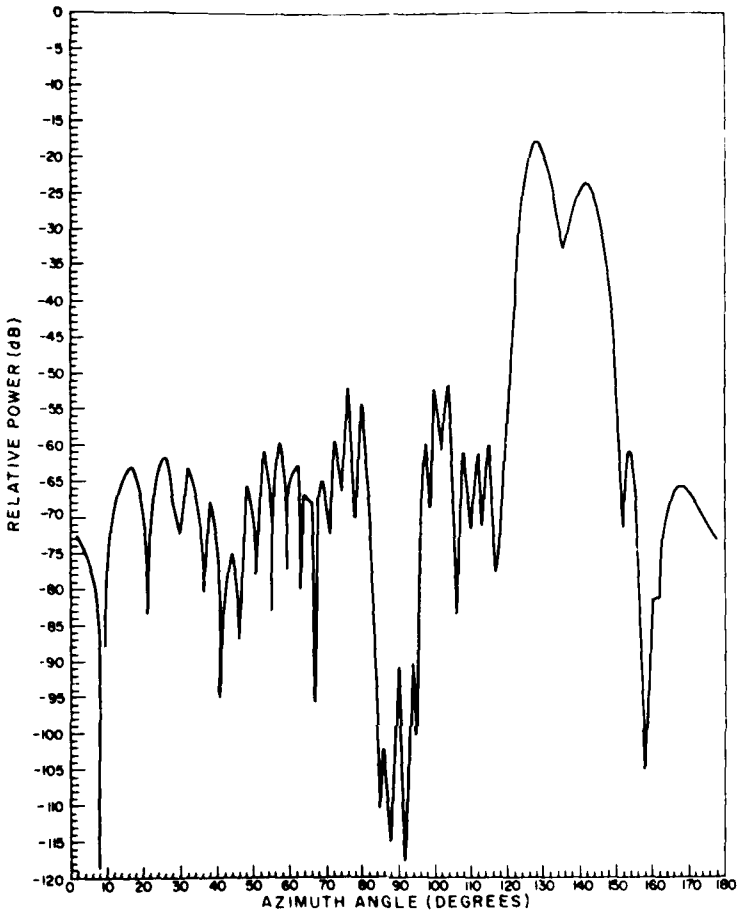

(f) Clutter Power vs Azimuth After Filtering but Before NFMRAD Processing

Figure 2. NFMRAD Antenna Patterns, Filter Power Transfer Functions, and Clutter Distributions (Cont.)

Figure 2(h) shows the composite antenna pattern (product of the antenna transmit pattern with the NFMRAD receive pattern). Note that the composite filter transfer function, Figure 2(d), and the composite antenna pattern, Figure 2(h), are complementary in that the composite filter transfer function has a reject region in the angular range where the composite antenna pattern has a mainlobe, and vice versa.

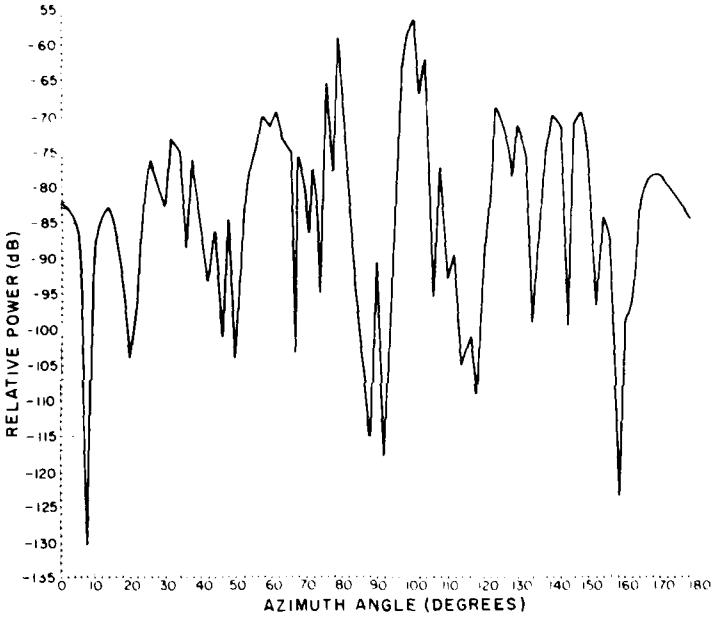

(g) Clutter Power vs Azimuth After Filtering and NFMRAD Processing

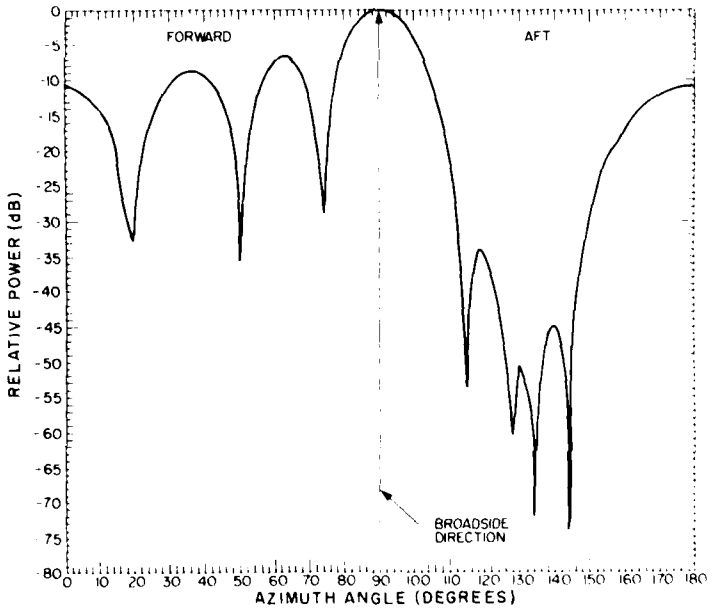

(h) Two-Way NFMRAD Antenna Pattern

Figure 2. NFMRAD Antenna Patterns, Filter Power Transfer Functions, and Clutter Distributions (Cont.)

2.2 Experimental Radar System

A simplified block diagram of the experimental NFMRAD system is shown in Figure 3. A low-power X-band transmitter is shown in conjunction with an eight-channel coherent receiver. An eight-element linear receive array feeds the RF front end of the eight-channel coherent receiver. Inphase and quadrature signals for each channel are generated at the output of the receiver. The receiver output signals are converted to a digital format and transferred into an array processor. The array processor forms the receive antenna pattern and filters the radar data. Filtered data is transferred into the host minicomputer where it is stored and displayed. Detection processing takes place in the minicomputer, and detection outputs are also available for display on a CRT. Filtered data is stored on magnetic tape for more sophisticated off-line detection processing, to be performed on a CDC 6600.

The experimental radar system uses conventional AMTI processing as a basis for performance comparison. Figure 4 depicts a block diagram of the total NFMRAD AMTI experimental radar system. The experimental system implemented incorporates two forms of radar processing, NFMRAD and AMTI. The two radar processing algorithms use common data as input; however, the NFMRAD algorithm differs from the AMTI algorithm in that the antenna patterns synthesized in processing are different. AMTI processing forms an antenna pattern by uniformly weighting each receive channel, while NFMRAD antenna pattern synthesis weights each channel so as to form a clutter notch in the receive pattern. Sidelobe clutter falling outside the NFMRAD antenna pattern clutter notch is not in the bandpass of the NFMRAD Doppler filter. Antenna beam-forming coefficients are a function of the Doppler filter bandpass center frequency, therefore, to detect a wide range of target velocities, several Doppler velocity filters are needed, with each filter requiring a separate antenna pattern and clutter notch. The NFMRAD and AMTI Doppler velocity filters that follow the antenna pattern processing are identical.

The block diagram of the NFMRAD system shown in Figure 3 depicts a low-power monopulse transmitter operating at 9.410 GHz. The experimental transmit pattern shown in Figure 16 indicates an azimuth beamwidth of 18^{0}. The experimental transmit elevation pattern of Figure 17 indicates a 3-dB elevation beamwidth of 12^{0}. The transmit horn shown in Figures 5(a) and 5(b) was placed in an anechoic chamber for the pattern measurements.

The eight-element receive array shown in Figures 5(c) and 5(d) feeds the RF front end of the eight-channel coherent receiver. A theoretical and experimental single-element pattern is shown in Figure 20. The measurements were made in an anechoic chamber, and the pattern is indicative of a waveguide opening into free space.

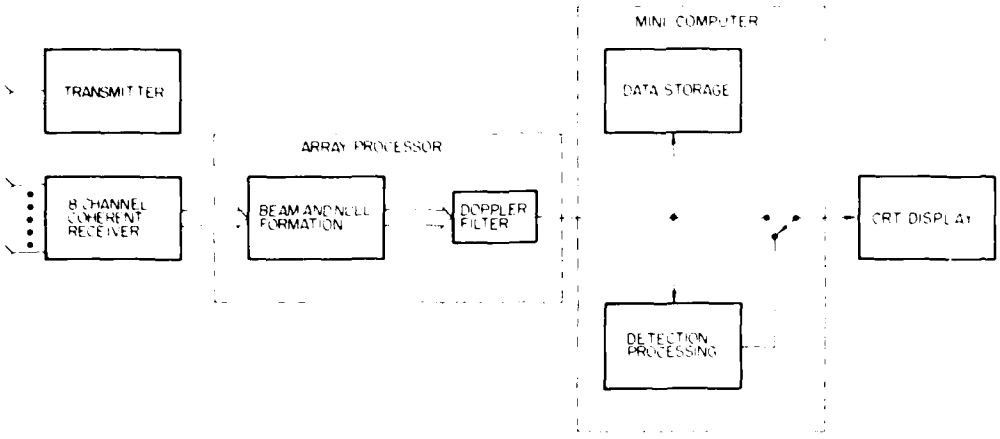

Figure 3. Simplified NFMRAD System

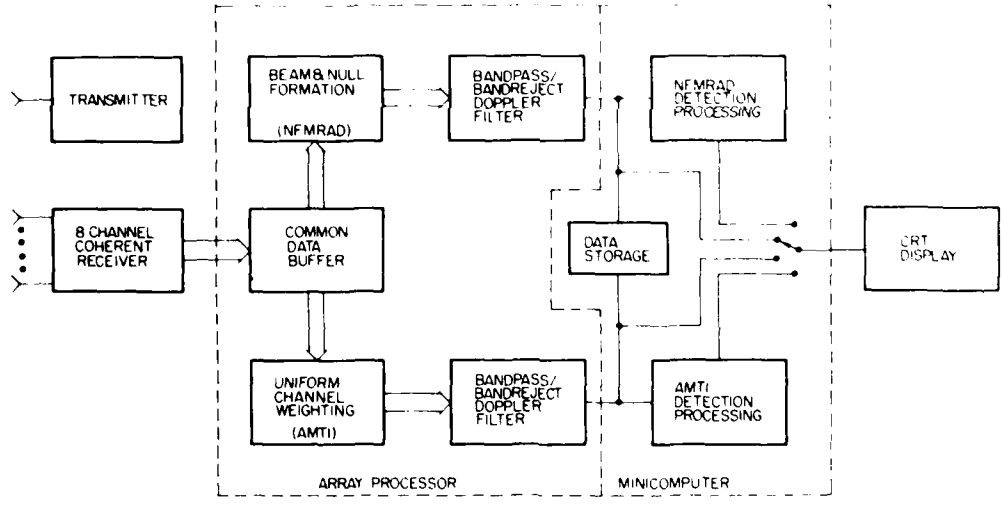

Figure 4. NFMRAD AMTI Experimental Radar System

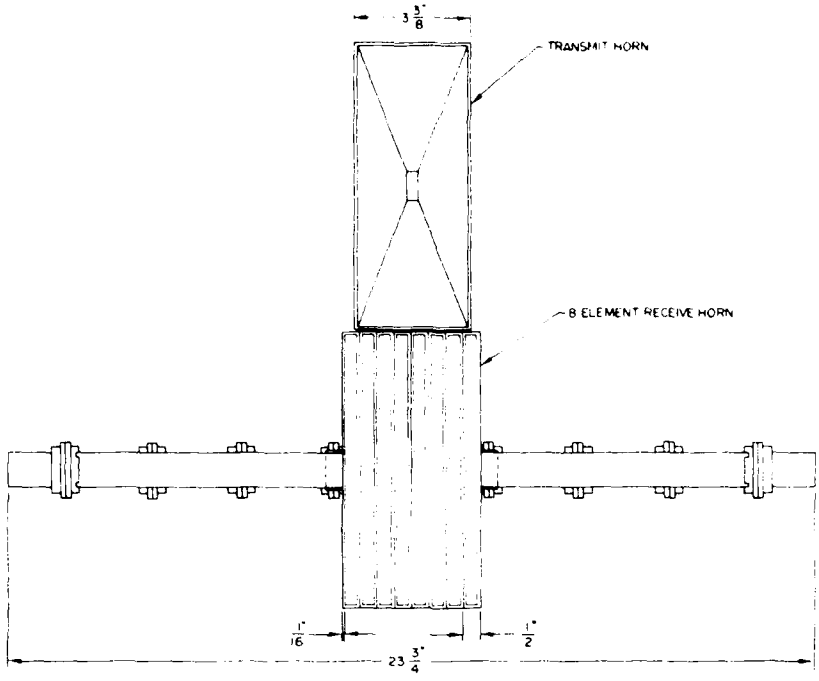

(a) Transmit and Receive Array (Front View)

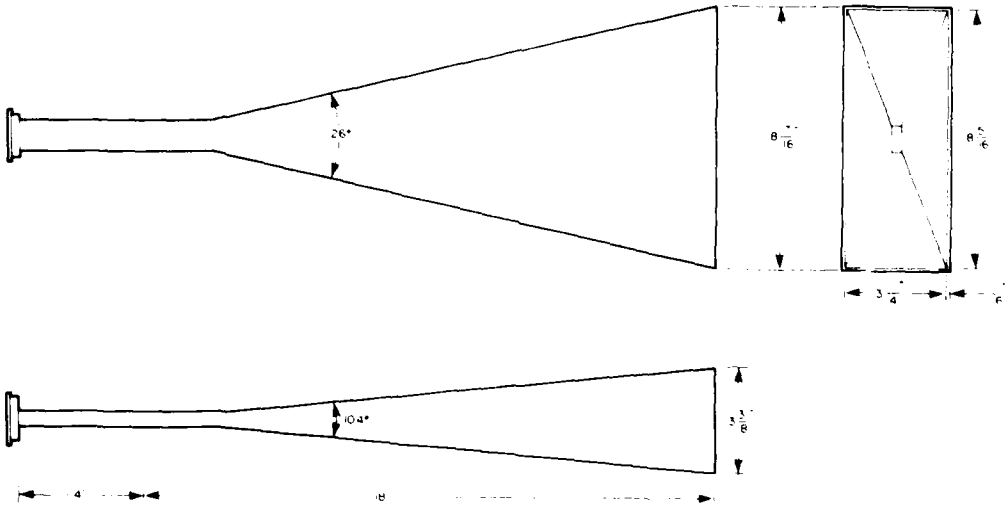

(b) Transmit Antenna (Three Views)

Figure 5. NFMRAD AMTI Transmit and Receive Antennas

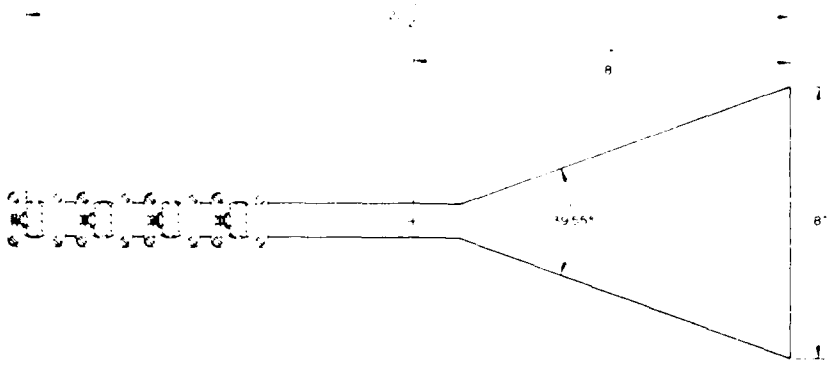

(c) Eight-Element Receive Array (Side View)

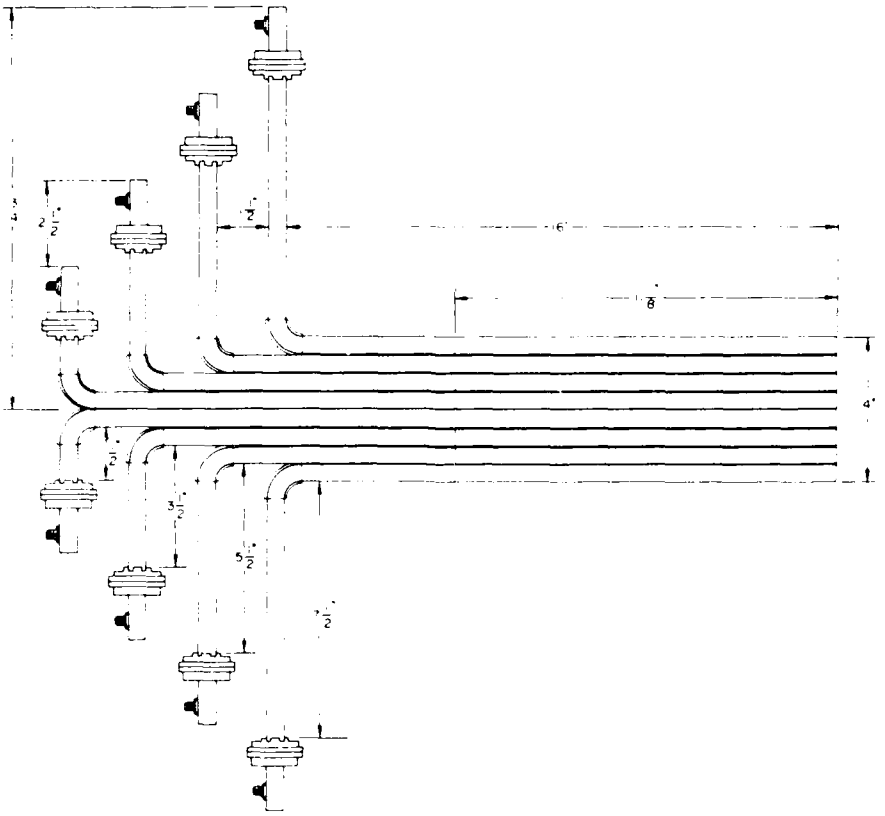

(d) Eight-Element Receive Array (Top View)

Figure 5. NEMRAD/AMTI Transmit and Receive Antennas (Cont.)

Figure 6 shows NFMRAD and AMTI real-time beam steering weights being supplied to the beamformer. The array processor forms the receive patterns and filters the radar data before storing the data into the host computer. The vertical sidelobe control, AMTI and NFMRAD patterns are shown in Figures 40 and 41. The array patterns are discussed in Sections 7.1 and 7.2. The Doppler filters are both a broadside and a bandpass filter. The Doppler filter characteristics are shown in Figure 42 and is discussed in Section 7.3. Filter designs are discussed in Appendices A and B. The location of the Doppler filter bandstop notch is controlled by the host computer, while the bandpass frequencies correspond directly with the NFMRAD clutter notch location in azimuth. The experimental radar system implements a single NFMRAD clutter notch and two corresponding Doppler filters. In addition to the NFMRAD pattern and filters, one uniformly-weighted AMTI pattern is synthesized, and an identical Doppler filter is also implemented in the radar array processor. Following 64 pulses (one coherent processing interval), the NFMRAD and AMTI Doppler filters produce one voltage amplitude per range cell.

Filtered NFMRAD and AMTI data is transferred into a high-speed minicomputer for further processing, recording, and display. Detection processing is implemented in real time for both NFMRAD and AMTI data. Detection output data or filtered voltage magnitude data may be displayed on the CRT. NFMRAD or AMTI detections or voltage amplitude may be displayed as a function of range cell on the CRT. Filtered NFMRAD and AMTI voltage magnitudes are recorded on magnetic tape in the format shown in Table 12 for off-line detection processing on a CDC 6600. Detection processing is also performed by the host minicomputer. This processing compares each filtered voltage amplitude with a programmable threshold voltage. Detection processing results are not recorded.

Table 1 summarizes system characteristics, some of which were discussed above.

Table 1. NFMRAD AMTI System Characteristics Summary

Experimental Operation
Limited broadside search (selectable search range)
Real-time antenna pattern synthesis, Doppler filtering, and detection processing achieved in radar van
Filtered data recorded for off-line additional detection processing on a CDC 6600
Operational Frequency
9.410 GHz

Transmitter	
Transmitting Antenna (Figure 4) Two-element vertical array	
Aperture Size	[illegible]
Power Density at Aperture (Figure 4) [illegible]	
Peak	[illegible]
Azimuth Half-power Beamwidth	75
Elevation Half-power Beamwidth	12
Beam Direction	[illegible]
Transmitter	
RF pulse length	≈ 2 [illegible]
PRF	187 [illegible]
Power	
peak	22. 5 W
average	11 mW
Receive Antenna (Figure 5) Eight H-plane sectoral horns in linear array	
Aperture Size	
composite	3.875 × 7.875 in. (9.84 × 20.0 cm)
single element	0.375 × 7.875 in. (0.953 × 20.0 cm)
Polarization	Horizontal
Azimuth Beamwidth	
composite	22^{O}
single element	134^{O}
Elevation Beamwidth	12^{O}
Receiver	
Minimum Detectable Signal	-95 dBm
Noise Figure	11 dB
RF Bandwidth	4 GHz
IF Bandwidth	16 MHz
Full Word Dynamic Range (8-bit mantissa with 3-bit base 2 exponent)	
Theoretical (no RF noise)	90 dB
Experimental	≈ 66 dB

Table 1. NFMRAD/AMTI System Characteristics Summary (Cont.)

A/D Conversion

Number of Range Cells	16
Sampling Rate	4 MHz (266 ns per range cell)
Interval per Range Cell	131 ft (40 m)
8-bit Conversion Rate	10 MHz

RF Noise Level as a Function of Receiver Sensitivity

IF Attenuation dB	Number of Mantissa Bits Consumed by RF Noise	
	Average Value	Worst Case
0	4	5
6	3	4
12	2	3
18	1	2
24	0	1
30	0	0
36	0	0
42	0	0

Switching noise on the A/D boards consumes one mantissa bit, independent of IF attenuation. A combination of RF and switching noise yields the following:

IF Attenuation dB	Number of Mantissa Bits Consumed by RF and Switching Noise	
	Average Value	Worst Case
0	4	5
6	3	4
12	2	3
18	1	2
24	1	1
30	1	1
36	1	1
42	1	1

Array Processor

6 asynchronous microprocessors	
32-bit word	
3 memory buses	
Performs real-time beam formation and Doppler filtering for NFMRAD and AMTI processing	
1 Doppler filter implemented	
3 dB Doppler filter passband	-238.6 Hz to -401.5 Hz (diverging case)
Angular sector of clutter in Doppler filter passband	105.1° to 116° (diverging case)

Table 1. NFMRAD/AMTI System Characteristics Summary (Cont.)

Minicomputer	
Memory	32 K interleaved core 4 K bipolar
Cycle Time	100 ns
Word Length	16 bits
Performs real-time detection processing, data storage and display functions	
Recorded Data Display (Table 12)	Filtered NFMRAD and AMTI data recorded voltage amplitude or detection output as a function of range cell

2.3 Theoretical Investigations Relative to the NFMRAD Experiment

2.3.1 THE NFMRAD EXPERIMENT

The following parameters and specifications are pertinent to the NFMRAD truck experiment:

Radar Van and Target Parameters

Truck velocity = 32.7 mph (14.6 m/s)

Target velocity = 34.4 mph (15.4 m/s)

Target velocity relative to truck = 11.2 mph diverging (5.02 m/s)

Target bearing relative to truck = 90° (constantly broadside)

Target Doppler Frequency = -315 Hz (diverging case)

Angle between truck track and target track = 19°

Angle at which clutter return has target Doppler frequency = 110.12° (diverging case)

The layout of the tracks for the radar van and the target is shown in Figure 6. This is a constant-bearing diverging case and ideally results in constant relative velocity and therefore constant target Doppler. However, experimental errors in truck and target velocities and in relative bearing will be present. As the experiments are performed using just one Doppler filter, it is necessary that the filter passband be wide enough to accommodate the anticipated experimental errors.

A constant-bearing converging experiment is generated by reversing the directions of the target velocity and truck velocity. For this case, the target Doppler frequency changes sign to +315 Hz, and the Doppler filter is designed with its passband centered on this frequency.

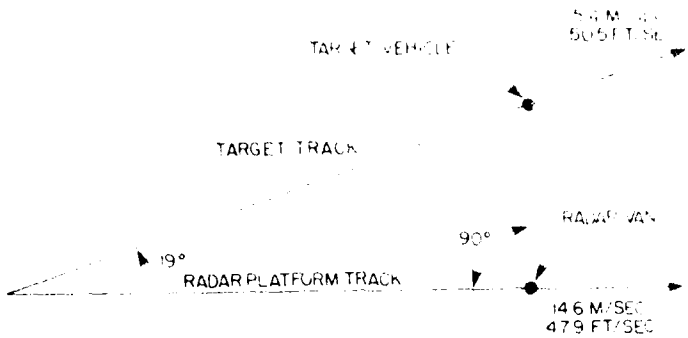

Figure 6. Radar Van and Target Tracks for NEMRAD Experiment (Diverging Case)

2.3.2 OPTIMIZATION OF FIR FILTERS

In order to determine the proper FIR filter response for optimum system performance, various widths and magnitudes of passband and stopbands were considered. For each cascaded filter (that is, bandpass filter combined with a Doppler filter), an optimum receive pattern was determined and a figure of merit obtained for the performance of the systems. For each system, the figure of merit was directly related to the ratio of the received power from the target to the total received clutter power. In order to compare systems using different transmit and receive patterns, as well as different filters, the figure of merit was normalized by that obtained from a system transmitting and receiving with the same patterns but with no filtering. Thus the figure of merit indicates the improvement in performance of any system over that of the omnidirectional, unfiltered system described above.

The investigation showed that two filter characteristics have significant effect on the figure of merit. One is the width of the filter passbands, and the other is the sharpness of rolloff from bandpass to bandstop. As would be expected, the wider the filter passband the higher the figure of merit, but this improves the MTI system, reducing the width of the individual filter passband increases the number of filters required, and this increases cost and complexity. For these reasons, there are other considerations. Because the target must remain in a resolution element to process through more than one pulse-to-pulse filter, the passband of the filter must be large enough to accommodate the expected target Doppler shift changes in the dynamics of the experiment as discussed earlier. In the particular case chosen for the truck experiment, the relative target velocity is small, and this results in the clutter angular sector associated with the passband of the Doppler filter being close to the angular sector associated with the antenna mainbeam. If

the cascaded filter does not have a rapid rolloff in the region between these sectors, the figure of merit will be reduced.

Generally, it was found that discriminations greater than about 40 dB for bandstop of bandpass filters did not improve the figure of merit. This is due in part to the noise produced on reception by the analog-to-digital converter because of truncation. Analysis of the experimental system to be used in the truck predicts that if theoretical nulls of the order of -55 dB were desired in the optimum receive pattern, truncation in the A/D converters would result in nulls only of magnitude -48 to -50 dB. The effect of the truncation is therefore equivalent to a noise source in the receiver system at a level 48 to 50 dB below the peak of the optimum (NFMRAD) pattern.

Taking into account the effect of the A/D truncation noise on the optimum receive pattern, the figures of merit for many different cascaded pairs of FIR filters were computed and compared. Bandwidth considerations, based primarily on expected errors in relative velocity in the truck experiment, indicated that cascading a BP33-2-1 bandpass filter with a BS33-14-1 bandstop filter was the best compromise solution (that is, high figure of merit together with adequate bandwidth).

2.3.3 COMPARISON WITH OTHER SYSTEMS

NFMRAD was compared with systems using Chebyshev and uniform array transmit and receive patterns with and without filters. In all cases the antenna apertures used were equivalent to those as specified for the truck experiment. Comparisons were made for targets located broadside to the truck and moving at various radial velocities in the interval -11.2 mph to -32.7 mph (-5.02 m/s to -14.6 m/s). Figure 7 shows the improvement of NFMRAD over systems using uniform array transmit and receive patterns with and without filters. The cascaded FIR filters used for this analysis were composed of a BP33-3-2 bandpass filter and a BS33-14-1 bandstop filter. Figure 8 shows the improvement of NFMRAD over systems using -40 dB Chebyshev patterns for both transmit and receive with and without filters. The filters used here were a BP33-2-1 bandpass and a BS33-13-1 bandstop.

Without filters, the performance of both the uniform array system and the Chebyshev array system are far inferior to NFMRAD. Even with filters, the uniform array system performance is 35 dB or more below NFMRAD over most of the clutter frequency range that was considered. The Chebyshev array system performance with filters is at least 8 dB below NFMRAD except for clutter frequencies in a range corresponding to low radial velocities relative to the ground where NFMRAD improvement was 20 to 35 dB. For a given aperture size, the composite Chebyshev pattern (the product of the transmit and receive patterns) has a broader mainlobe than the composite NFMRAD pattern, and for targets with

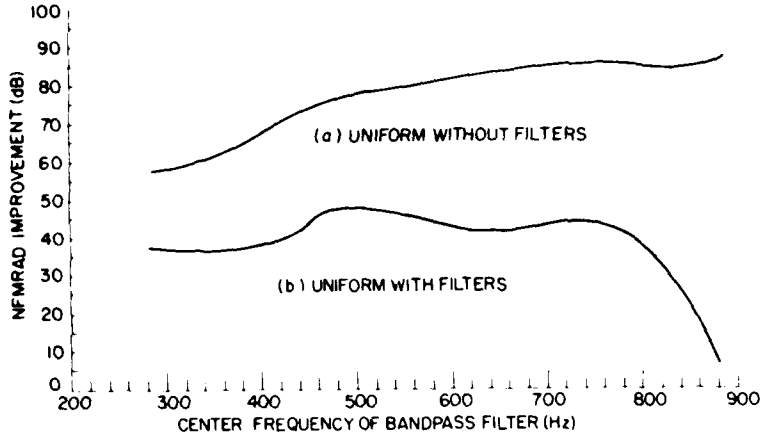

Figure 7. Improvement of NFMRAD System Over a System Using Uniform Patterns on Both Transmit and Receive (a) Without Filters, (b) With Filters. Filters were BP-33-3-2 and BS-33-14-1

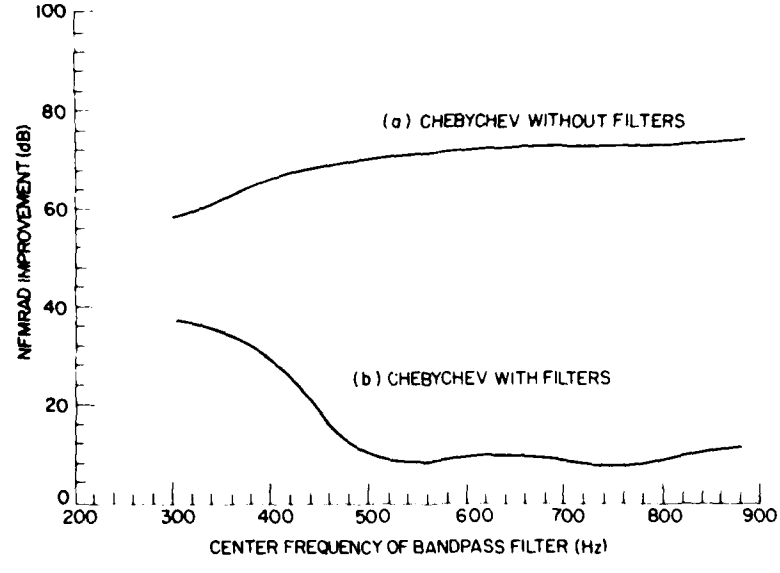

Figure 8. Improvement of NFMRAD System Over a System Using Chebyshev Array Patterns on Both Transmit and Receive (a) Without Filters, (b) With Filters. Filters were BP-33-2-1 and BS-33-13-1

radial velocities close to the radial velocity of the local ground and [illegible] broadening deteriorates the performance considerably. For the Doppler [illegible] system with filters, the performance improves as the difference between the radial velocity of the target and that of the local ground clutter decreases.

3. NFMRAD RF HARDWARE

NFMRAD is a "proof-of-concept" system, and the objective was the [illegible] construction of a radar capable of performing the postulated functions with the greatest economy. This economy involved simplicity in design at a minimum monetary cost in the addressing of the program objective. A unique and sophisticated experimental tool is the product of this "economic" consideration.

NFMRAD was created in order to experimentally investigate and evaluate the use of antenna pattern null filtering to reduce Doppler clutter. As a result, NFMRAD performance capabilities are limited in extent. NFMRAD, as a proof-of-concept design, is not a fully operational side-looking, stand-off, airborne moving target indicator radar design based on the antenna null-filtering concept.

The principle performance characteristics of NFMRAD are highlighted here. As a side-looking Airborne Moving Target Indicator (AMTI) radar, NFMRAD does not possess the performance capability of angular scanning (azimuth or elevation). NFMRAD responds to targets in its main beam and is capable of nulling Doppler clutter received through one antenna sidelobe. This is possible since the NFMRAD possesses a multichannel receiver design. However, the antenna null is developed through digital signal processing of information from the eight receive channels. The NFMRAD also performs conventional Doppler filter processing. However, here again only one Doppler filter of experimental interest is implemented, and, as with the antenna null formation, it is created through the digital processing of the eight-channel receiver information. These performance capabilities and limitations are a direct result of the intended purpose of the NFMRAD hardware design.

The NFMRAD may be subdivided into three major functional subsystems: the RF system, containing the transmitter and the receiver mixing preamplification stage; the Signal Conditioning section, consisting of the intermediate frequency amplifiers, the gain control, detectors, sample and hold circuits, analog-to-digital converters, output, timing, and control logic; and the Signal Processor, consisting of a high-speed array processor slaved to a host CSP-30 minicomputer. Figure 9 illustrates this simple functional subdivision of NFMRAD.

Discussion of the NFMRAD RF hardware design and operation will encompass the RF section and portions of the Signal Conditioning section critical to the proper functioning of the NFMRAD RF design. Remaining topics dealing with the digital hardware will be developed in Section 4.

Figure 9. NEMEAD System Block Diagram

NEMEAD is a pulse-Doppler radar that uses [illegible] for clutter suppression. The [illegible] of NEMEAD [illegible] of the transmitter subsystem and the receiver-beamsteering block. The [illegible] signal generator is developed [illegible] 9-GHz signal [illegible] output and subsequently selecting the 9.41-GHz signal [illegible] designated f_0. The received signal [illegible] 9-GHz mixer [illegible] to develop a 60-MHz IF signal which is phase-and-amplitude detected to obtain the magnitude and phase of the target signal vector. In this section, [illegible] true rate of change of the phase of the target signal vector is processed [illegible] essing.

The above receiver design approach is extended to eight parallel receiver channels. This receiver configuration, coupled with an eight-element receiver antenna, allows null placement in the digital processing of the eight-channel receiver information. Each receiver channel contains a [illegible] system, referenced to channel 1. This gain-control approach was used to provide the receiver with a broad linear dynamic range.

Referring to Figure 10, the pulsed wave's [illegible] through the action of transmit/receive pin diode switches. These switches are located before the transmitter mixing stage and after the transmitter [illegible] amplifier stage (TWTA). The pin diode switch trigger pulses are designed and synchronized to produce a periodic waveform of the desired pulse [illegible] transmitter antenna is coordinated with the receiver beamsteering, and [illegible] high-gain, sectorial horn. Figure 10 is a simplified schematic of the NEMEAD design. Note that delays are provided prior to the [illegible]

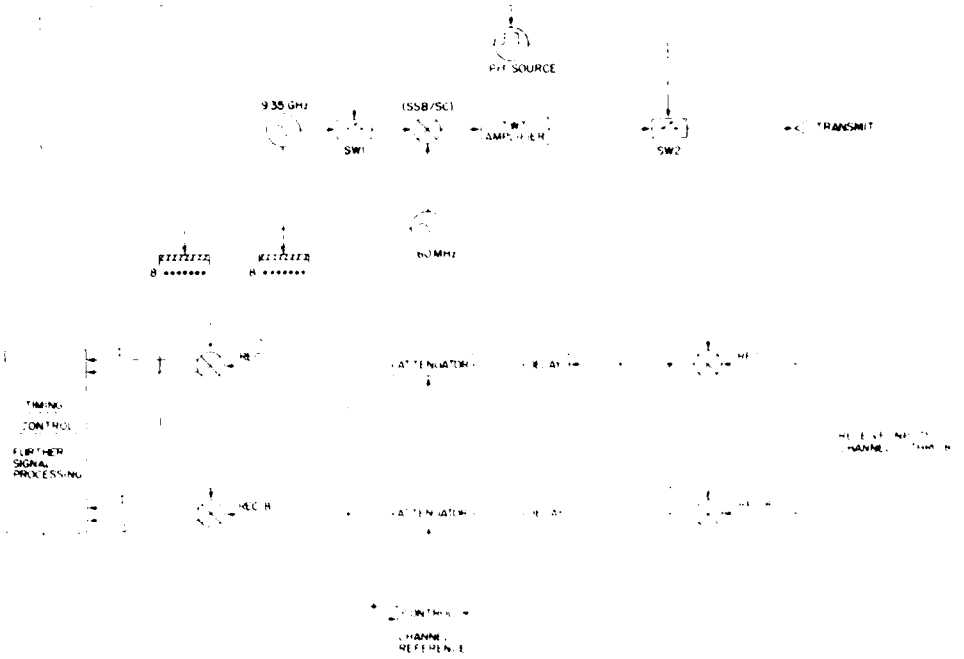

Figure 3.1 Simplified Diagram of SEASAT-A SAR Electronics

3.1 Transmitter

Frequency Stability: ±0.002 percent

Temperature Range: 32 to 140°F (0 to 60°C)

Harmonics: -60 dBc (minimum)

Sub-Harmonics: -52 dBc (-45 dBc minimum)

Spurious: -60 dBc minimum

Output Impedance: 50 Ω

The secondary source (a 60-MHz crystal-controlled oscillator (Greenray, model number Y-313B-60)) specifications are as follows:

Frequency Stability: ±0.005 percent

Temperature Range: 32 to 140°F (0 to 60°C)

Output Power: 300 mW (minimum)

Harmonics and Sub-Harmonics: -20 dBc (minimum)

Output Impedance: 50 Ω

[illegible] the 9.3-GHz source passes through a +6 dB directional coupler (Narda, model number 401C-6). Power at the +6 dB port of the directional coupler is provided to the receiver exciter stage of the receiver. This signal is at a frequency of 9.3 GHz, serves as the LO for the eight receiver channels. The [illegible] MHz is next divided, and the half-[illegible] at eight mW power. Inside the eight receiver exciter stages, the [illegible] with [illegible] GHz) and the half [illegible] with [illegible] MHz. [illegible]

4.2 GENERATION OF CARRIER

[illegible]

The mixing products of the 9.35 GHz and 60 MHz are free to propagate from both waveguide ports of this device. The 60-MHz residual is attenuated by the cutoff characteristics of the waveguide. However, the sum and difference signals, as well as the original 9.35 GHz, are within the passband of the waveguide.

Power consisting of reflected 9.35-GHz signal and the various mixing product propagate down the waveguide in the direction of the -6 dB directional coupler output port. The directivity of this directional coupler is specified at 15 dB. This enables the coupling of mixing product power into the LO signal path to the receiver. This spurious signal power consists of the sum, difference, original 9.35 GHz, and the intermodulation products. The presence of these mixing products in the LO path to the receiver mixing preamplification stages would desensitize the receiver by raising the mixing preamplification noise floor; that is, effectively "jamming" the receiver front end. In order to avoid this difficulty, an isolator and the first pin diode modulator have been placed between the -6 dB directional coupler and the orthomode mixer. An understanding of the mechanism involved may be obtained through examination of two distinct cases: diode switch "off" condition and diode switch "on" condition.

First consider the diode switch "off" condition. During this condition the pin diode switch provides -45 dB of nondirectional attenuation. This effectively attenuates the 9.35 GHz power (a maximum of 750 mW to a level of -16 dBm) available at the orthomode mixer to a level below that required to effect mixing (2-mW minimum required signal power). Hence, these mixing products cannot be generated by the "turn on" of the mixer by the 9.35-GHz signal power during this condition.

Given the possibility of sufficient signal current available for mixer turnon from the 60-MHz source, sufficient reverse signal attenuation exists to prevent receiver desensitization. The mixed signal would be at a level below the maximum mixer output (measured in this case at 20 mW). But for sake of argument, choose the level of 20 mW. This signal would traverse -45 dB of attenuation in the diode switch, -7 dB of directional attenuation in an isolator preceding the switch, a minimum of -1 dB of insertion loss available in the -6 dB directional coupler, as well as additional eight-to-six power division (-9 dB channel). This would give a total reverse path signal attenuation of approximately -126 dB. If one assumes 20 W of power available at the output of the diode switch, then a maximum of -106 dBm would be available at the first mixing stage of each receiver channel. This would be the -90 dBm noise floor of the receiver.

[illegible] of the [illegible] feedback to the transmit antenna during first [illegible] of [illegible] stages of both receivers. This is true since little or [illegible] exists actually exists at the [illegible].

Next consider the circumstances during the diode switch "off" state. During this period of system operation, radar tracking is not desired since the received signals are of no interest at this time. Hence, it is desirable to avoid receiver front end desensitization during transmitter pulse duration. It is important to note here that the -57 dB isolation also reduces any reflected signal in order to protect the primary 9.30-GHz source from potential damage. In any event, the power in the reflection path passes through a total of 32 dB. It reduces any feedback signal to a maximum of -89 dBm of signal power relative to the input to the first mixing stage of each receiver channel. Given the sensitivity of these mixers, this low signal level is insufficient to cause signal suppression.

The pulsed 9.30-GHz CW signal is mixed with the 30-MHz CW signal to produce sum, difference, and 9.30-GHz pulsed signals. A second stage of isolation (-21 dB) prevents any power reflected from the input side of the circulator from reflecting back to the ring hybrid mixer and producing spurious interference. The five-pole butterworth response waveguide bandpass filter selects the desired band pulsed signal (9.41 GHz). The 30-MHz separation between the input signal and the filter passband characteristic (9.41 GHz ± 30 MHz 60-dB bandwidth of 89.6 MHz) severely attenuates any leakage from the 9.30-GHz CW component of the mixer output.

3.1.3 TRANSMIT PULSE FORMATION

The desired transmit pulse characteristics are achieved through the use of two pin diode switches. One of these is located before the traveling wave tube amplifier, the other after the manual waveguide switch following the traveling wave tube amplifier.

The first modulates the primary source signal, thus generating the low-level pulse, and also provides RF feedback suppression during the transmit pulse. The second switch serves two functions as well. It blocks the relatively high power generated by the TWTA during the interpulse period, and also "shapes" the RF pulse.

The first diode switch is a Hewlett-Packard model 33142A, and the second is model 33222A. The model 33142A possesses SMA type RF ports and SMA control port, while the model 33222A possesses N-type RF ports with a BNC control port. Both switches are of compact physical design.

The diode switch is an absorption type and employs RF diodes shunting the RF path. A large negative going pulse applied to the switch control port is the control signal for switch turnon. In the absence of control signal bias, the shunting diodes provide a low-impedance path to ground. During this condition (shunting diodes biased on by the RF signal) no more than -4 dB of incident RF power is available at the RF output port. In this state the switch is in the "off" condition. With the

negative going control pulse applied, the shunting diodes are biased off, and incident RF power is available at the RF output port for the duration of the control pulse. Insertion loss of the switch during the "on" condition is specified to be less than 1 dB. Figure 11 illustrates the basic electrical structure of the pin diode switch.

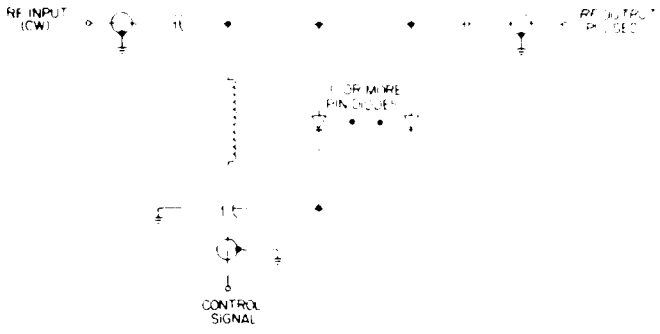

Figure 11. Typical Microwave PIN Diode Switch (Adapted from Hewlett-Packard Application Note, Fast Microwave Switch-SPST Series 33140 and 33640)

An RF pulse produced from the action of Model 33222A will possess rise and fall times no greater than 10 ns. Model 33142A will typically produce an RF pulse with a rise time of 5 ns and a fall time of 7 ns. Switch turn "on" or "off" is a function of control voltage threshold. Actual turn "on" or "off" times are a function of the switching characteristics of the diodes shunting the RF path. Once the negative going control pulse amplitude in fact falls below or rises above the negative control voltage threshold, the switch will turn on or off, according to the characteristic switching time of the switch diodes. Switch model 33142A is capable of absorbing 2 W of CW power in the off mode. Switch model 33222A, at the output of the TWTA, is capable of absorbing 2 W of CW power and sustaining a 75 W peak power at a maximum pulse width of one ms and 0.001 duty cycle.

Both switches are driven by a TTL compatible switch driver (device number DH0035G). The main band trigger is provided to integrated logic circuitry (TTL) which drives the switch driver of the first microwave diode switch. From the same main bang trigger source, the main bang trigger to the second diode switch is first supplied to an SN74123 (TTL retriggerable monostable multivibrator). This device delays and reshapes the main bang trigger. The output of the SN74123 TTL device is also supplied to integrated logic circuitry (TTL) which drives the switch driver of the second microwave pin diode switch.

Referring to Figure 12, the first diode switch precedes the orthomode mixer and the second diode switch follows the TWT amplifier. As a result, a finite and significant delay exists in the propagation of the RF pulse from the first diode switch to the second diode switch. To compensate for this propagation delay, the firing of the second switch driver is delayed through the action of the SN74123 TTL device. The rising edge of the main bang trigger latches the first stage of the SN74123 on. External RC timing circuitry is adjusted to yield a first-stage on-time of 300 ns, equal to the propagation delay from first to the second switch. At the down clock of the first SN74123 stage, the second stage is clocked on for the predetermined period of 266 ns. The output of this stage is used to drive the second microwave pin diode switch driver. The microwave switch is turned on at precisely the time the RF pulse generated by the first switch has risen to its maximum amplitude, and remains on for 266 ns. This action permits opening of the second switch when a stable RF pulse is incident at its input port and reshapes the wide RF pulse to desired pulse width.

The RF pulse generated by the first diode switch is wider than that desired for transmission. This is a result of the filtering action of the waveguide filter that eliminates the higher frequency components of the RF pulse. To eliminate this problem, the main bang trigger, as it originates from the Signal Processing Section—card nest board number 1 (System Timing I), is 320 ns wide. As a result, the RF pulse generated by the first microwave diode switch is 320 ns wide with rise and fall times less than 10 ns. The RF signal bandwidth is theoretically 400 MHz wide *at this stage of transmission pulse formation.* However, the waveguide filter bandpass is only 9.41 MHz wide. Consequently, the RF pulse incident at the input to the TWT amplifier is 320 ns wide, with rise and fall times of approximately 100 ns each. The 320 ns wide main bang trigger is delayed 300 ns by the 74123 device's first stage, which in turn fires the 74123 device second stage for the desired pulse period of 266 ns. The firing of the second stage of this TTL device enables the capturing of the degraded RF pulse (when it is present at the second switch), and reshapes the RF pulse to the desired transmit pulse characteristics. The RF pulse, incident at the transmit antenna input, has a slightly rounded peak and is 266 ns wide, with a rise time of approximately 6 ns and fall time of approximately 8 ns.

This reshaping process theoretically produces a final transmit pulse with leading and trailing edge "porches." However, these porches are of duration less than 30 ns and are no greater than 0.6 mW in intensity. These porches were not detectable during system bench testing using a linear detector of 30 mV/MW sensitivity. Figure 12 below illustrates the pulse firing sequence discussed above.

The rise and fall time of the switch driver output pulse is between 4 to 6 ns. This switching time is characteristic of the switch driver and independent of input pulse rise and fall time. In addition, the negative amplitude of the control pulse is

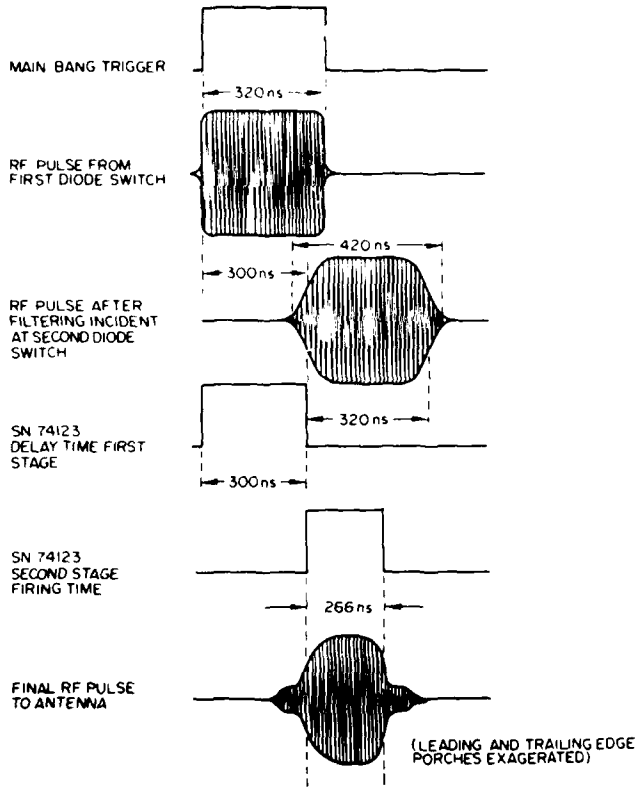

Figure 12. Timing Diagram: Transmit Pulse Formation

far larger than the voltage necessary for diode switch turnon. This insures precise and reliable operation of the diode switches. Figure 13 is a schematic of the microwave diode switch firing circuitry. The quad-Nand gate and inverter (TTL devices) driving the switch driver add minor delays in the firing of the switch drivers. These minor delays have been compensated for in the design of the firing circuitry.

The second switch also attenuates noise generated by the TWTA during the interpulse period. The characteristics of the Hughes X1277H TWTA are such that 1 mW of white noise is continuously generated across its bandwidth, in the absence of input signal. With the second switch turned off during the interpulse period, white noise is reduced to a level of at least -45 dBm. This, combined with the -65 dB coupling figure from transmit to receive antennas, prevents subsequent jamming of the receiver during the interpulse period.

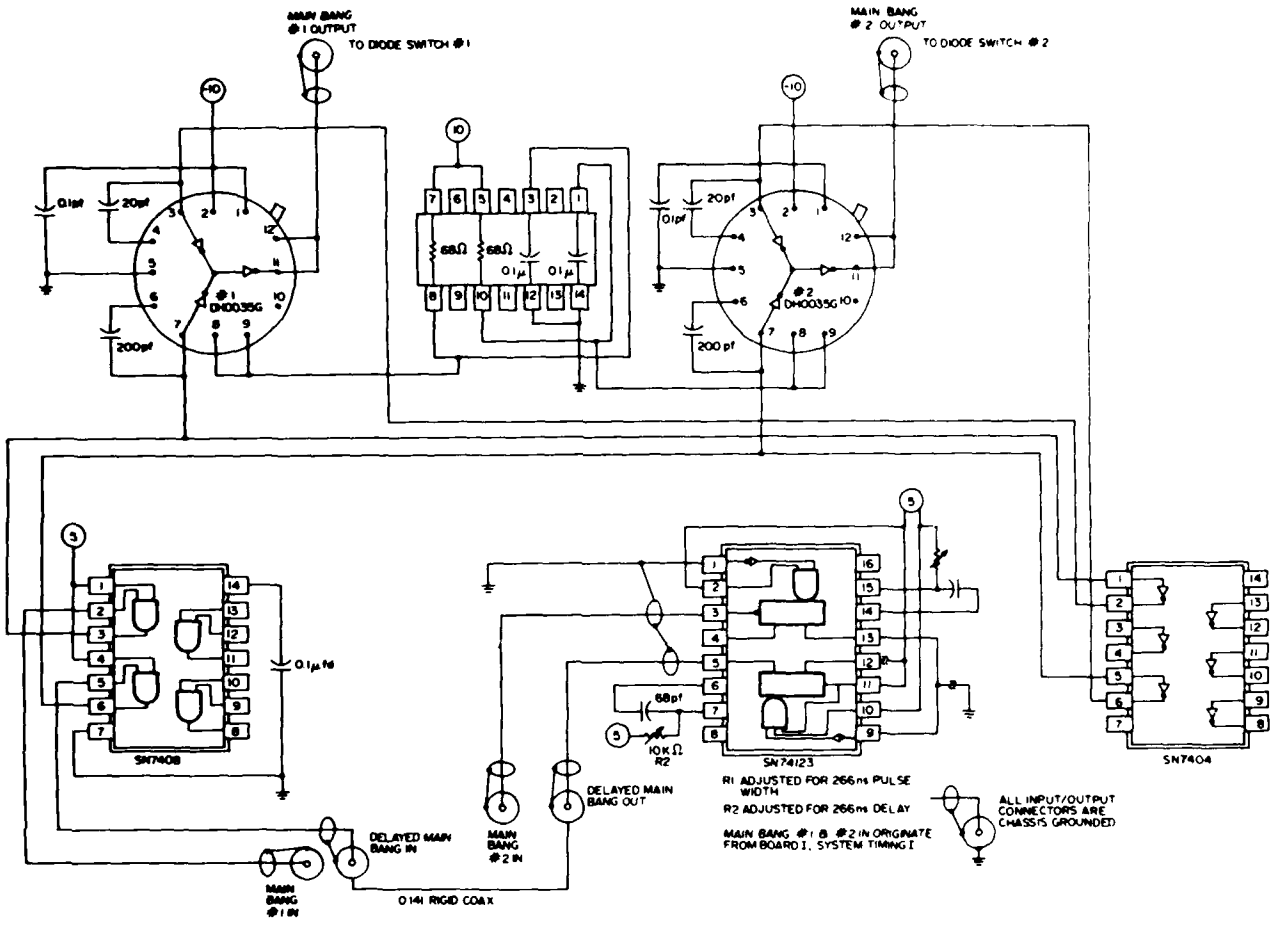

Figure 13. Diode Switch Firing Circuitry (Adapted From Hewlett-Packard Application Note, Fast Microwave Switch-SPST Series 33140 and 33640)

3.1.4 TRAVELING WAVE TUBE AMPLIFICATION

The filtered pulsed 9.41-GHZ signal must be amplified before transmission. Insertion losses through components between the orthomode mixer and the amplification stage yield a final peak signal power of 5 mW maximum incident at the amplifier input. The maximum safe permissible driving power for this TWT amplifier (Hughes, model X1277H) is 0.6 mW. This may be achieved by adjusting the variable attenuator (adjustment located on the transmitter rack front panel) to a setting of -9.2 dB. With 0.6 mW of drive power, the TWT amplifier output power is 22.5 W.

Continuously variable transmitter power is available in two power ranges. In the low range (0-5 mW), the TWTA is switched out of the circuit by two manual waveguide switches, one preceding and one following the TWTA. During low-range operation, the variable attenuator, preceding the TWTA, affords continuous adjustment of transmit power passing through the parallel waveguide transmission path. With the TWTA into the circuit, the same variable attenuator is used to continuously vary transmit output power from 1 mW to 22.5 W through variation of TWTA input power. Figure 14 is the measured gain characteristic of this particular TWTA. In order to protect the TWTA from reflected power, a -16 dB isolator has been installed between the amplifier output and the waveguide switch following the amplifier. This protects the TWTA during manual waveguide switch operation and during the second microwave pin diode switch off time.

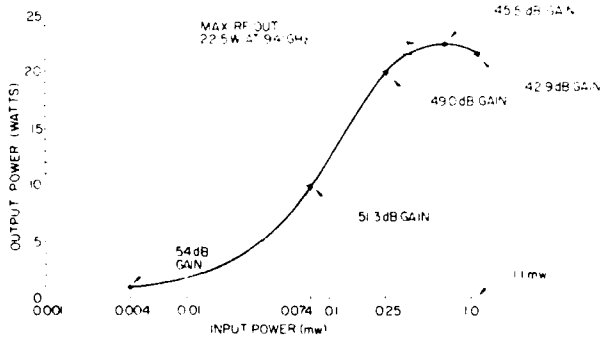

Figure 14. TWTA Gain Characteristic

3.1.5 TRANSMIT ANTENNA

The transmit radiator is a simple sectorial horn situated directly above the receive horn array and polarized in the horizontal direction (H-plane vertical). The horn aperture has an E-plane dimension of 3.3 in. (8.3 cm) and an H-plane

dimension of 8.3 in. (21.2 cm). The H-plane taper length is 18.7 in. (47.5 cm), with an E-plane taper length of 19.5 in. (49.5 cm). These dimensions yield a theoretical gain of approximately 20.3 dB. Figure 15 illustrates the transmit horn.

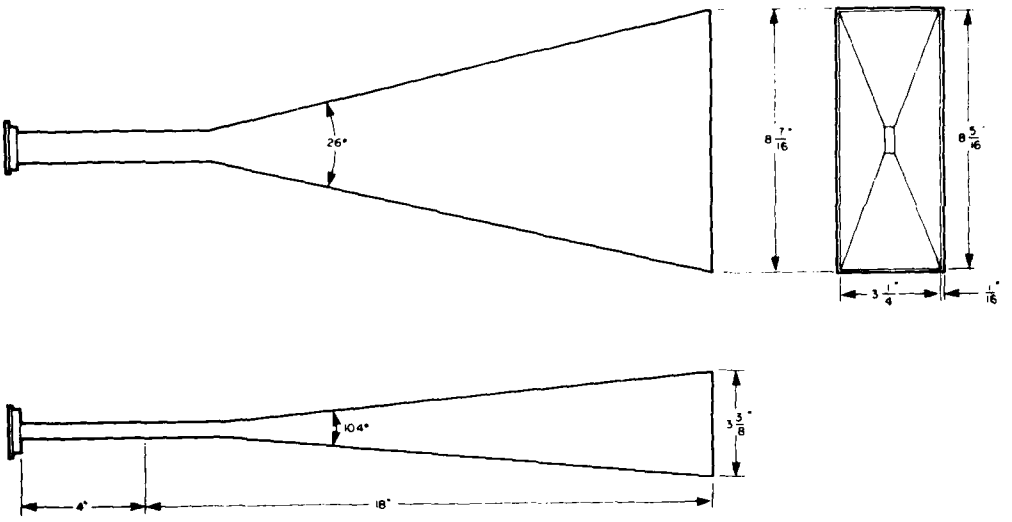

Figure 15. Transmitter Horn

Given the above horn aperture dimensions and uniform aperture excitation in the E-plane and cosine aperture excitation in the H-plane (TE_{01} mode excitation of waveguide feeding a flared horn), the theoretical azimuth 3-dB beamwidth is approximately 19.3°, and the theoretical elevation 3-dB beamwidth is 10.3°. The theoretical azimuth mainlobe beamwidth is approximately 44°, and the theoretical elevation main lobe beamwidth is approximately 25.8°. It is the azimuth directivity pattern which is of interest here, although the elevation directivity pattern determines the multipath characteristics of the system. Figure 16 compares the theoretical and experimental transmit directivity patterns, while Figure 17 illustrates the experimental elevation directivity pattern.

It is important to note that coupling between the transmit horn aperture and the aperture of any given receive antenna element aperture (located directly below the transmit horn) is approximately -65 dB. This coupling of transmitted power into the receive antenna element apertures results in the characteristic main band video at the start of range timing.

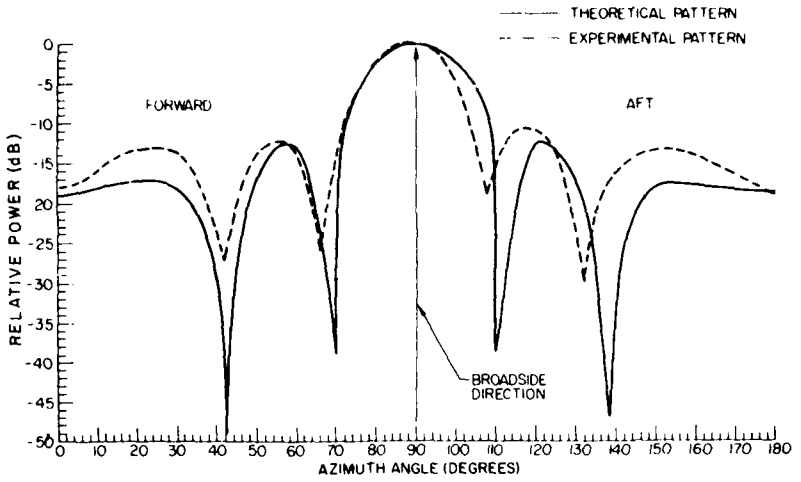

Figure 16. Theoretical and Experimental Transmit Horn Azimuth Power Patterns

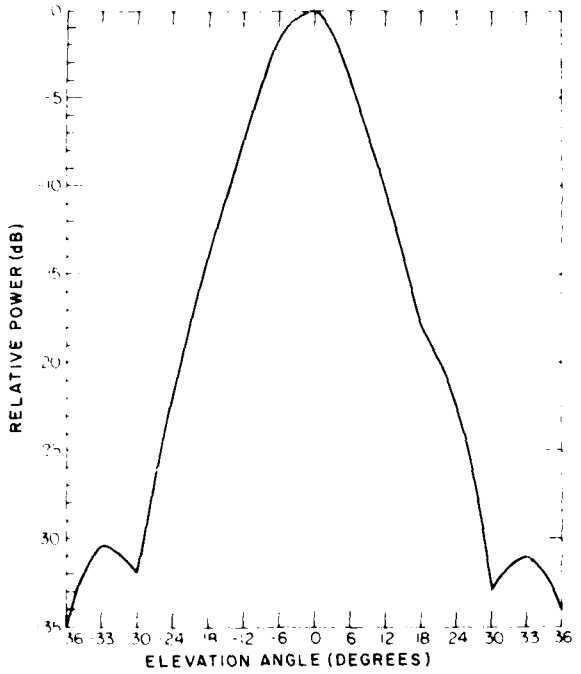

Figure 17. Experimental Transmit Horn Elevation Power Pattern

3.1.6 DIAGNOSTIC FACILITIES

Two continuously variable output power ranges may be selected; 0-5 mW, or 1 mW to 22.5 W. In addition, facilities have been provided for the synthesis of a Doppler offset frequency. The injection of this synthetic Doppler signal into the transmitter mixing process enables efficient diagnostic testing of the receiver hardware and software. The Doppler frequency is that of a target moving away from the radar platform at a speed of approximately 11.5 mph (5.14 m/s) (or Doppler frequency of -325 Hz). The signal is created by the single sideband suppressed carrier mixing of 325 Hz with 60 MHz prior to the orthomode mixing of 60 MHz with 9.35 GHz. The 60 MHz and 325 Hz undergo phase cancellation mixing and the subsequent selection of the first lower sideband of this single sideband mixing process. Phase cancellation mixing is the only effective single sideband suppressed carrier mixing technique available. The frequency separation of the first upper and lower sidebands from the carrier (325 Hz) renders the design of the necessary sideband filter very difficult (if not impossible) for this application.

Figure 18 illustrates the Doppler target simulator. Note that the schematic illustrates the selection of the first upper sideband. Selection of the first lower sideband is accomplished through the interchange of the GL ports of the Hewlett-Packard Balanced mixers shown in the offset signal generator section of the Doppler generator schematic. A simple Wein Bridge audio oscillator and amplifier comprise the 325-Hz simulated Doppler signal source. The power supplied to the orthomode mixer is the same (+9.3 dBm) whether it is a pure 60-MHz sinusoid or a sinusoidal 60-MHz plus Doppler sinusoid; thus, the signal level at the receiver is invariant to the selection of either mode.

Selection of the injected Doppler is accomplished by a switch provided on the front panel of the RF assembly (Transmitter Receiver Rack). With the radar platform stationary, the operator may select the injection of Doppler into the transmitter signal; thus, a Doppler target moving at the velocity of interest (-11.5 mph, -5.14 m/s) is synthesized. The signal may be directed at a convenient stationary radar target for operational check of the receiver hardware and receiver operating software, rather than attempting the simulation of this Doppler target through appropriate motion of either the radar platform and or radar target. The operation of the receiver, with respect to range, may be checked through the appropriate selection of either the low- or high-power ranges of the transmitter. This may be done with or without the synthesized Doppler target and the use of an appropriate stationary radar target.

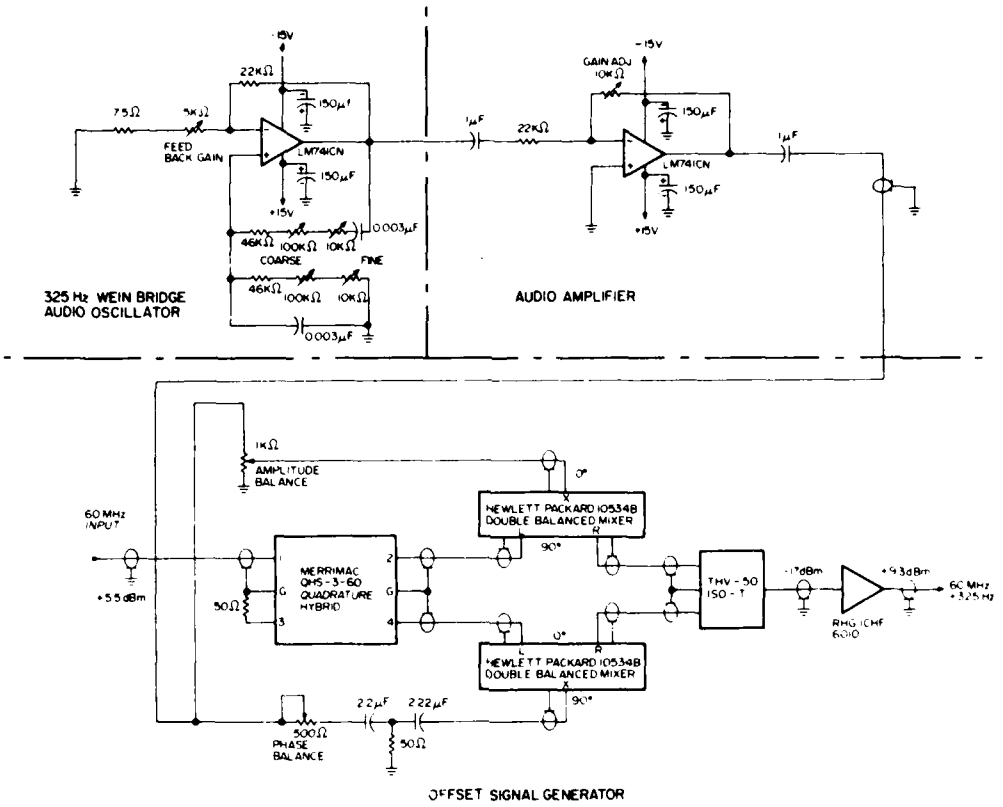

Figure 18. Doppler Target Simulator

3.1.7 SUMMARY OF TRANSMITTER SPECIFICATIONS

a. Frequency Sources

1. Primary Frequency Source (crystal controlled)
   Frequency: 9.35 GHz ± 0.0025 percent
   Power: 250 mW min to 1 W max, (typically 350 mW)
   Harmonics: -45 dBc (min), (typically -65 dBc)
   Spurious: -60 dBc (min)
   Supply: +28 V dc at 1A
   Unit is convection cooled
2. Secondary Frequency Source (crystal controlled)
   Frequency: 60 MHz ± 0.005 percent
   Power: 800 mW (min) (typically 950 mW)
   Harmonics: -20 dBc (min)

Supply: +28 V dc ± 5 percent Regulation

Unit is convection cooled

3. Offset Doppler Test Source

Wein Bridge Audio Oscillator

Frequency: 325 Hz, less than 1 percent distortion

Amplitude: typically 0.8 V peak to peak

Supply: ±15 V dc

b. Pulse Characteristics (Pulse Generation, TTL Controlled)

1. Pulse Generated by First Microwave PIN Diode Switch

Frequency: 9.35 GHz

Prf: 1531 Hz

Pulse Width: 320 ns

Pulse Rise Time: 5 ns

Pulse Fall Time: 7 ns

2. Pulse Characteristics after Filtering

Frequency: 9.41 GHz

Prf 1831 Hz

Pulse Width: 320 ns

Pulse Rise Time: 100 ns

Pulse Fall Time: 100 ns

3. Pulse Characteristics after Amplification and Action of Second Microwave PIN Diode Switch

Frequency: 9.41 GHz

Prf: 1831 Hz

Pulse Width: 266 ns

Pulse Rise Time: 6 ns

Pulse Fall Time: 8 ns

Leading and Trailing edge porches no greater than 30 ns in duration and at least -36 dB below pulse peak power.

c. Transmitter Emission Characteristics

1. Signal (Pulsed CW)

Frequency: 9.41 GHz

Prf: 1831 Hz

Pulse Width: 266 ns

Pulse Rise Time: 6 ns

Pulse Fall Time: 8 ns

Occupied Bandwidth: 60 MHz (approx.)

Maximum Peak Power: 22.5 W

Duty Cycle: 0.04 percent

Spurious: -40 dBc minimum

[illegible]

[illegible]

[illegible]

[illegible]

[illegible]

3. Source Power Supplied to Receiver and Other Processes

   1. Source Power Supplied to Receiver Quiet Power Control Unit

      Frequency: 9.35 GHz

      Power: +8 dBm below 9.35 GHz source output

   2. Source Power Supplied to Receiver Local Oscillator

      Frequency: 60 MHz

      Power: +8 dBm below 60 MHz source output

4. Synthesized Doppler Target

   1. Lower sideband is phasized for simulation of target moving at -11.1 mph (-4.14 m/s) relative to radar platform

   2. Suppression of unwanted signal components below desired lower sideband:

      Upper Sideband: -20.8 dB

      Carrier: -20 dB

5. Schematic of NEMRAD Transmitter Subsystem Figure 19

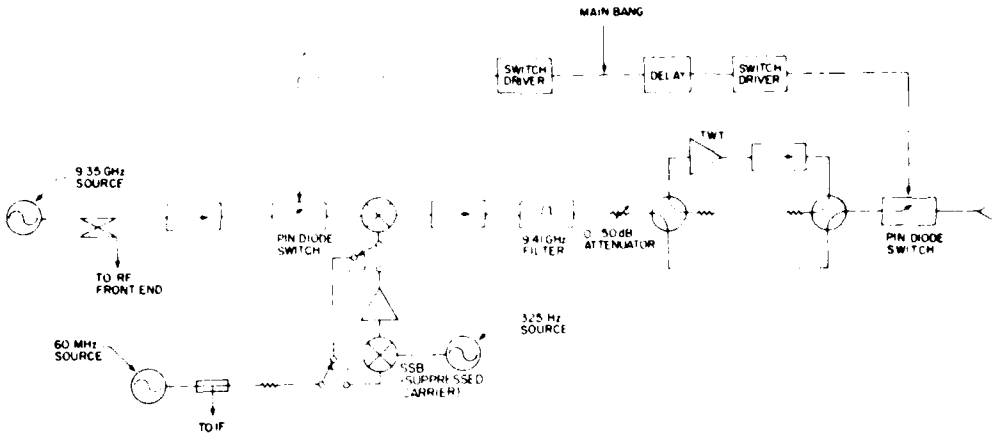

Figure 19. NEMRAD Transmitter Subsystem

3.2 Receiver

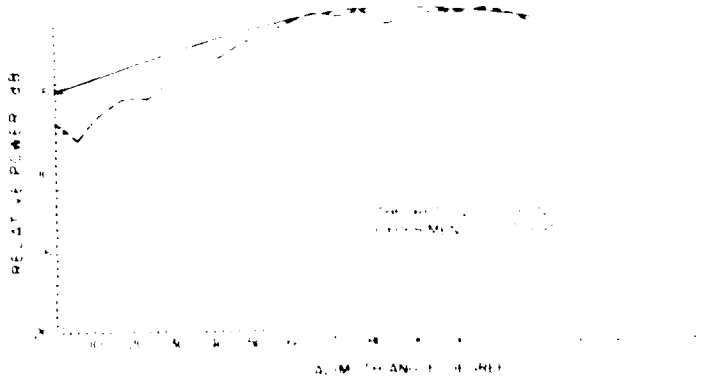

Figure 20. Theoretical and Experimental Elevation Directivity Patterns

Assuming uniform aperture excitation, the receive array produces an azimuth 3-dB beamwidth of approximately 16°. The calculated eight-element azimuth directivity pattern and the experimental pattern are illustrated in Figure 22. The eight-element directivity pattern was calculated using the principle of antenna pattern multiplication. The relationship for the single-element pattern was multiplied, point for point, with the equivalent value of a pattern produced by eight equally spaced point source radiators. The normalized relationship or array factor for eight equally spaced point sources is as follows:

$$E = \frac{\sin(n\psi/2)}{n\sin(\psi/2)}$$

where

n = no. of elements

$\psi = d_r \cos\theta + \delta$

δ = 0 for uniformly excited point sources,

θ is measured from the normal to the array face and

$$d_r = \frac{2\pi}{\lambda_0} d \qquad \lambda_0 = 3.188 \text{ cm}$$

with d = 1.27 cm, the element spacing (center to center of the receive elements). Each value of "E" achieved for a given θ is multiplied for the same value of "E_H" achieved for the single-element pattern to yield "E" or the composite amplitude pattern. The "E" is squared and the log to base 10 taken for development of the eight-element azimuth directivity (power) pattern. Note that all pattern calculations are normalized and referenced to 0 dB.

The above calculations yield a close approximation to the nature of the eight-element pattern. The correction of phase and amplitude errors, element by element, is reference to the first channel receive element. This calibration is accomplished in the signal processing of the rex radar information with the target and radar platform stationary. The calibration is performed on a daily basis, before and after a field testing sessions (refer to Pre-Initialization routine, software and field testing sections of this report).

Polarized in the horizontal direction (E-plane parallel to ground), the receive array is situated directly below the transmit horn. As a result of this configuration, energy from the transmit horn couples into each receive element at a level 6.5 dB below the peak transmit power. This results in the detection of main bang video at the beginning of range timing.

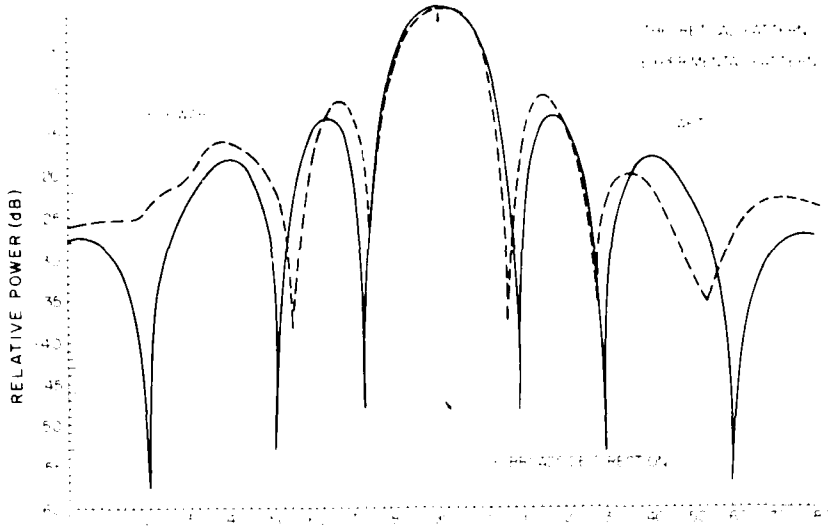

Figure 22. Theoretical and Experimental Azimuth Power Pattern for Receiver Eight-Element Array

3.2.2 RECEIVER FRONT END

Referring to the schematic in Figure 23, the received 9.41-GHz signal is mixed with the 9.35-GHz LO signal to produce a 60-MHz intermediate frequency (IF). The IF signal is then amplified. These two steps are accomplished in one unit (RHG Model MDM 8-12 12A mixer preamplifier). The LO power is derived from the primary (9.35 GHz) transmitter signal source. Power from this primary source is coupled at a level 6 dB below its output power. This coupled power is once again divided, eight ways (through a Merrimax eight way power divider, Model Number PDM 82-10C), and one each of the eight power divider outputs is supplied to the mixing stage of each of the eight receiver mixer preamplifiers. Typically, the LO power available to each of the receiver front end mixers is 11 mW or 10.4 dBm. The mixer/preamp requires 3 to 18 dBm of LO power to effect dependable mixing, and an LO injection level is excess of 23 dBm will cause damage to the double balanced mixer. Intermodulation products of signal and LO mixing are suppressed a minimum of 20 dB below that of the 60-MHz IF signal.

The RF bandwidth of the mixer/preamp is 4 GHz, centered at 10 GHz. The IF bandwidth is typically 16 MHz, centered at 60 MHz. The noise figure of the mixer/preamp is typically 11 dB. Mixer/preamp RF to IF gain is specified to be 20 dB minimum. With these specifications, the front-end signal sensitivity is

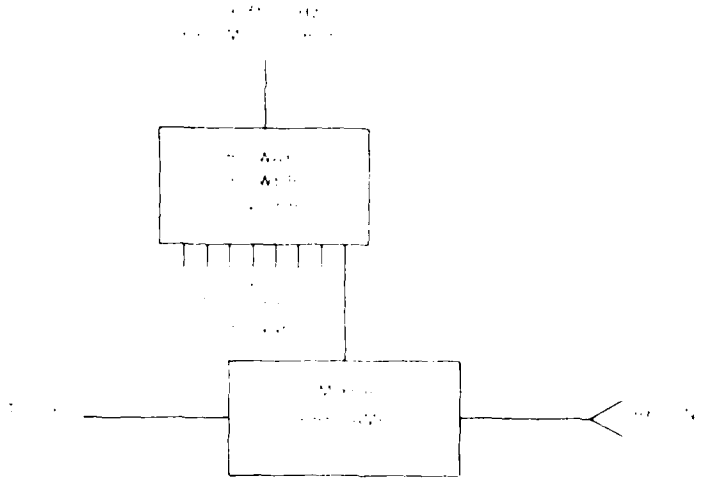

Figure 23. Receiver Front End

approximately -95 dBm per channel. This results in an approximately 1.4×10^{-8} W m^{-2} minimum incident signal power requirement per receiver channel for signal detection.

2.2.3 RECEIVER GAIN CONTROL

With the exception of channel 1, each IF signal passes through a variable attenuator (0-15 dB, Merrimac Model ARM-1) that is used to trim the gain of each channel. The signal in channel 1 is divided into two paths. One is sampled by a log amplifier whose output is ultimately used to automatically control the gain of all channels to insure linear operation over the complete range of expected input signals. The other forms the input for a linear receive channel (that is, channel 1). The variable attenuators in channels 2 through 8 enable balancing of these channels with respect to channel 1. Compensation of the element signals for dissimilar array elements is accomplished in the signal processing. This calibration procedure is accomplished daily to establish an antenna pattern measurement baseline, as well as to compensate for changes in receiver component operating characteristics.

The division of power in channel 1 enables the realization of an unorthodox gain control system. Unlike conventional AGC, the NEMRAD stepped gain control provides a broad but linear dynamic range. This is achieved through a feed-forward control approach. The signal derived from the logarithmic amplifier in channel 1 is amplitude sampled and converted to a 4-bit digital code. The digital amplitude

information is transformed in combinatorial logic into a 3-bit toggling code to control programmable attenuators in each of the eight linear receive channels.

Sufficient time for switching and settling of the attenuators is provided by delaying the IF signal 0.59 μs with a long RG-58 coaxial cable. With a delay of 1.6 ns/ft (5.25 ns/m), 360 ft (109.7 m) of RG-58 provides the necessary 0.59 μs delay. However, a considerable insertion loss is associated with this 360 ft (109.7 m) coaxial delay line. To compensate for the loss, the signal is preamplified prior to insertion in the delay line.

In addition to toggling the switchable attenuators, the 3-bit switching code is processed and provided to the systems logic interface. This information carries real-time values of received signal level. In this fashion, the order of magnitude of the received signal amplitudes are preserved for later adjustment of the digitized linear channel outputs.

The amplification of the received signal for gain control is accomplished through a logarithmic amplifier. The signal is amplified and the logarithmic value of the signal level is sampled and converted to the 4-bit digital amplitide code. This enables the use of a 4-bit analog-to-digital converter for the first step in generation of the 3-bit attenuator switching commands. The use of linear amplification would require the use of an analog-to-digital converter of much greater than 4 bits of dynamic range. Unfortunately, the required conversion speeds constrain this portion of the design to A/D converters of 8-bits capacity or less. The choice of a 4-bit A/D converter also simplifies the design of conversion logic for the generation of attenuator switching commands as well as the digital amplitude information for later digital processing of the received signals.

Amplifiers following and preceding the switchable attenuators in each channel serve as isolation amplifiers. The attenuators, during switching, are mismatched to the 50-Ω delay lines. In order to isolate reflected spurious power during attenuator switching, a stage of IF amplification has been inserted prior to the attenuators. In addition, a stage of IF amplification following the attenuator isolates the mismatch from the input of the I and Q mixers in each channel. These amplifiers also compensate for component insertion losses throughout the receiver system, as well as provide the required system gain.

Without the influence of this gain control system, the dynamic range of the receiver (per channel basis) would be only 48 dB. This is derived from the 8 bits of A/D conversion capacity for either the I or Q sides of the eight channels. Each toggling of a bit in the A/D converters corresponds to a doubling in signal level. Hence, 8 bits of conversion multiplied by 6 dB of signal dynamic range per bit yields 48 dB of dynamic range.

The attenuators extend this dynamic range by 42 dB for a total linear dynamic range of 90 dB. The attenuation occurs at the rate of 6 dB per step or 6 dB per bit change on the switching command code. This operation is illustrated in Table 2.

Table 2. IF Attenuation as a Function of Base 2 Exponent

Total Attenuation (dB)	Steps Set (dB)	Base 2 Exponent (IF attenuator switching code)
0	none	000
6	6	001
12	12	010
18	12 & 6	011
24	24	100
30	24 & 6	101
36	24 & 12	110
42	24 & 12 & 6	111

When the signal power present at the input to the mixer preamps approaches -53 dBm, the operation of the switchable attenuators is automatically initiated. At a level of -5 dBm of power incident on the input to the mixer preamps, the receiver will begin to saturate. It is important to note that the 90-dB dynamic range assumes a noise level such that no A/D conversion bits are set by noise rather than the signal of interest. The total dynamic range is linear as opposed to logarithmic (encountered with feedback control, AGC). This enables the signal processing that forms the NEXRAD and Doppler filters to be implemented.

3.2.4 IF BANDPASS CHARACTERISTICS AND DETECTION OF MOVING TARGETS

The three IF amplifiers serve various functions with regard to the receiver gain control system. In addition, their cascaded bandpass characteristics determine the overall IF bandpass characteristic. The composite IF bandpass is centered at 60 MHz with a 3-dB bandwidth of 8 MHz and a rolloff of 40 dB per decade.

The receiver IF bandwidth has been chosen to approximate the reciprocal of the pulse width (that is, 2×1.256 ns $\approx$ 7.5 MHz), which in turn approximates the performance of a matched filter. This filter characteristic only crudely approximates a matched filter characteristic (that is, the IF bandwidth characteristic passes only those signal components within 4 MHz of the 60-MHz IF). Many of the signal frequency components are attenuated, resulting in pulse spreading. This would cause two consecutive pulses that are very close in time to overlap or become indistinguishable as two unique pulses. This does not pose a problem with respect to range determination, since the range of any given target is a function of the associated target pulse position within a given range bin. This dictates the range

accuracy of the radar. This is opposed to continuous range determination referenced to the leading edge of a received pulse. Hence, no need exists to preserve exact pulse characteristics to enable separation of pulses, since pulse position as a time are of importance only with respect to their occurrence in a given range bin. Consequently, the IF bandpass characteristic is sufficiently broad to preserve the gross nature of a received pulse and yet sufficiently narrow to band limit noise (that is, the maximization of SNR is tantamount to the preservation of exact pulse shape and the avoidance of interpulse overlap or interference).

Information carried by the received pulses (per channel) encompasses not only position information (with respect to any given range bin) but return signal instantaneous phase information as well. The division of radar range into range bins, and the timing of returned pulses with respect to these range bins, enables the extraction of target range information. However, phase discrimination of the returned signal, with respect to the transmit signal, is accomplished for the extraction of instantaneous target signal phase information. This later phase information when compiled to form a time history of phase differences for a target of interest, constitutes information concerning the Doppler frequency of the target of interest and hence the target's radial velocity with respect to the NEMRAD platform.

The IF signal undergoes quadrature mixing with the 60-MHz reference from the transmitter. This quadrature mixing yields signal magnitudes proportional to the rectangular components of the signal vector. One product of quadrature mixing is proportional to the magnitude of the real component of the signal vector, while the other product is proportional to the magnitude of the imaginary component of the same signal vector. In addition, the positive or negative nature of the real imaginary parts of the signal are determined. Hence, the quadrature mixing of the IF signal and 60-MHz reference results in information regarding not only the amplitude of the received signal but knowledge of its complex component magnitudes as well. Later processing of the component magnitudes, on a per pulse basis, yields the instantaneous phase difference with respect to the transmitted signal. Compilation of a time history of these phase differences enables measurement of the time rate of change of received signal phase. This is the definition of frequency and is the Doppler frequency of the target. The positiveness or negativeness of complex component magnitude yields information on the positiveness or negativeness of the phase difference. With the time history of positive or negative phase differences, the sign of the target Doppler may be determined with successively increasing negative phase differences indicating a target with relative velocity diverging from the radar, and a time history of successively increasing positive phase differences indicating an approaching target.

The data processing of the target signal vector components not only yields target Doppler information but also enables the appropriate processing of each channel

output, carrying information on the same target, in order to form the receive antenna pattern null. This is covered in greater detail in Section 5.4.2 of this report.

The IF signal, after the attenuator post amplification stage, is power divided and inserted at the G-X ports of two Hewlett-Packard Double Balanced Mixers (MDL 10534B). A 60-MHz reference signal from the transmitter secondary signal source is power divided through a Merrimac Quadrature Hybrid (Model QHS3-20). This 60-MHz reference signal is typically of 500-mW power level, yielding approximately 50 mW, after eight-way power division, of reference signal power into each of the eight quadrature hybrids. In the quadrature hybrid, the 60-MHz reference signal is power divided. One portion is inserted directly into the R-G port of one of the model 10534B double balanced mixers. The other portion of the 60-MHz reference is phase delayed by 90° and provided to the R-G port of the remaining model 10534B double balanced mixer.

The portion of the IF signal mixed with the unshifted 60-MHz reference produces a signal in phase with the 60-MHz reference and with magnitude proportional to the magnitude of the inphase component of the signal vector. This is designated as the "I" component of the signal vector and is represented as the real component of the signal vector in phase with the reference. The portion of the IF signal mixed with the phase-delayed 60-MHz reference signal produces an output in quadrature with the 60-MHz reference and with magnitude proportional to the quadrature component of the signal vector. This signal is designated as the Q component of the signal vector and is represented as the imaginary component of the signal vector in quadrature phase relationship with respect to the reference signal. Figure 24 illustrates this I and Q signal relationship with respect to the 60-MHz reference vector.

Referring to Figure 24, a time history of consecutive I and Q values, indicating a change in Φ such that each new Φ value is successively greater than the last and changing in the positive direction, would indicate a positive target Doppler or target motion on a radial path away from the NFMRAD platform. The converse is true for Φ changing in the negative or clockwise direction.

There is conversion loss associated with the mixing process. In addition, the only mixing products of interest are the sum and difference frequencies. The original input mixing frequencies and the intermodulation mixing products are of no interest. To overcome these difficulties, both I and Q sides of each channel possess amplification and filtering of the quadrature detection output. Filtering is accomplished by virtue of the frequency response characteristics of components following the quadrature mixers. The wideband amplifier (Datel Model AM-193B) following the mixers compensates for conversion loss in the mixing process. The gain of this amplifier is set to equal the conversion loss of the power division and

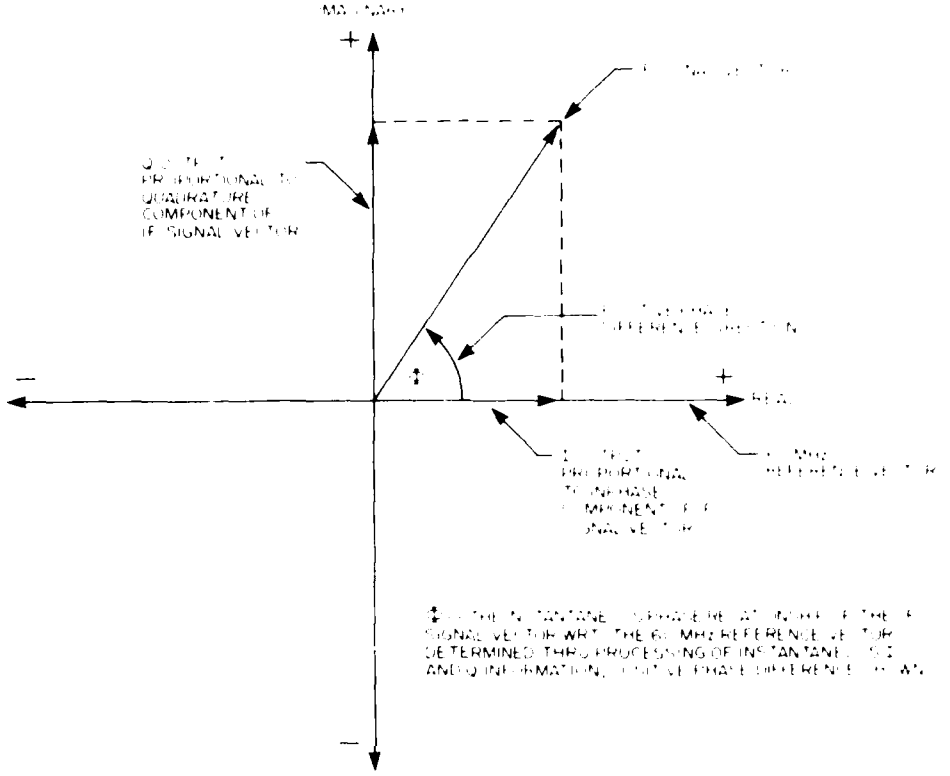

Figure 24. Diagram of I and Q Outputs with Respect to Reference Signal Vector

mixing process (typically 8.1 dB). The 3-dB bandwidth of this device is also established by the chosen gain setting. Gain and bandwidth characteristics of this device are coupled. By the selection of the sideband amplifier gain at 8.1 dB, the amplifiers 3-dB bandwidth is set at roughly 10 MHz. This not only compensates for conversion losses but also affords attenuation of all frequency mixing components above 10 MHz.

Further attenuation of unwanted high-frequency mixing products below 10 MHz is accomplished during the amplitude sampling of the amplified I and Q signals. The response time of the sample and hold device (Datel High Speed Sample and Hold, Model SHM-UH) is such that the highest sinusoidal signal frequency that can be accurately quantized is 5 MHz (that is, a maximum sampling rate of 10 MHz [minimum required Nyquist rate to accurately sample a 5-MHz sinusoid]). As a result, the 3-dB bandwidth of this device is 5 MHz; thus, additional attenuation of mixing products above 10 MHz is afforded, as well as attenuation of mixing products

between 5 and 10 MHz. Any remaining products of mixing above 5 MHz are present as noise riding the sampled signal.

The 10-MHz sampling rate is sufficiently fast in order to sample a signal of 2-MHz bandwidth. The signal bandwidth results from a pulse train of roughly 2 KHz prf, with each pulse carrying information of approximately 1-KHz bandwidth (1 KHz equals one-half the unfolded Doppler spectral bandwidth. This bandpass is sufficiently broad to preserve the approximate character of each pulse (1.256 ns = 3.8 MHz). This later characteristic minimizes amplitude error generated from off-peak sampling of individual pulses.

The sample signal for both I and Q channels of each of the eight receive channels is converted to an 8-bit amplitude code on a pulse-to-pulse basis (Datel A/D Converter Model VH8-B2). The analog-to-digital converter possesses a maximum conversion rate of 10 MHz (5-MHz conversion bandwidth), again providing sufficient conversion speed for a signal of 2-MHz bandwidth. This digital amplitude code for the eight I and Q pairs is sent in parallel to the Radar Data Buffer for eventual transfer into the array processor.

3.2.5 SUMMARY OF RECEIVER SPECIFICATIONS

a. Frequency: 9.41 GHz

b. Antenna

1. Eight sectorial horns flared in the H-plane only, horizontally polarized, forming an eight-element receive array
2. Array 3-dB Beamwidth
   Elevation (H-plane): 8°
   Azimuth (E-plane): 16°
3. Gain
   Array: 20.0 dB (approx.)
   Element: 11.1 dB (approx.)

c. Front End (Per Channel Basis)

1. LO Source: 9.3 GHz supplied from transmitter, typically 11-mW power level
2. RF Bandwidth: 4 GHz (centered at 10 GHz)
3. Maximum RF Signal Power: +23 dBm
4. Minimum Discernable Signal: -95 dBm
5. IF Bandwidth: 16 MHz
6. RF to IF Gain: 20 dB

d. IF Section (Per Channel Basis)

1. IF Bandwidth: 8 MHz centered at IF frequency with 40 dB per decade rolloff.
2. IF Frequency: 60 MHz
3. IF Gain: 60 dB (approx.)

e. Signal Detector (Per Channel Basis)

1. Quadrature Detector
2. Reference: 60 MHz from transmitter at typical power level of 50 mW

f. Composite Characteristics (Per Channel Basis)

1. Dynamic Range: 48 dB (without gain control)
2. Dynamic Range With Gain Control: 90 dB (no noise environment)
3. Gain Control: Referenced to channel 1, gain settings in 6-dB increments with fully automatic operation
4. Detected Signal Bandwidth: 2-MHz (approx.)
5. Doppler Bandwidth: 2 KHz (approx.) centered at 0 Doppler frequency
6. Signal information (on a per pulse basis) transferred to System Digital Logic Interface, I and Q from each channel (relative amplitude only, order of magnitude information obtained from gain control circuitry)

   Amplitude Word: 8 bits

   Order of Magnitude Word: 4 bits (base 2 notation)
7. Timing and Control: Digital (TTL) origin
   See Section 4 of report for complete discussion

g. Pattern Null Formation, Doppler Filtering Processing, and Target Detection accomplished in Digital Signal Processing of Digitized I and Q Information (See Section 5 of this report)

h. Schematic of NEMRAD RF Receiver Hardware, Figure 25

4. RECEIVER DIGITAL HARDWARE

Receiver digital hardware is tasked with the analog-to-digital conversion of I and Q detector outputs. Digitally formatted data is temporarily stored in mantissa and exponent buffers, but ultimately transferred to an array processor in which beam formation and Doppler filtering takes place. Digital hardware utilized to convert the outputs of the I and Q receiver to a format appropriate for input to an array processor will be discussed in the following sections.

A functional description of receiver digital hardware will be presented to yield insight into the tasks required of each digital system. An input-output approach will be used for explanation throughout the digital receiver hardware discussion, since a review of hardware design techniques is beyond the scope of this report.

Reference to Figure 26 shows that the receiver automatic gain control hardware establishes a base 2 exponent which is ultimately transferred to the array processor. Logically, the logarithm of channel 1 IF signal establishes the signal attenuation

---

Channel 1 illustrated. Existing gain control circuitry - channels 2 through 8 are identical except for presence of balancing attenuator after mixer preamp and absence of detector, logarithmic amplifier with 4-bit A/D conversion circuitry.

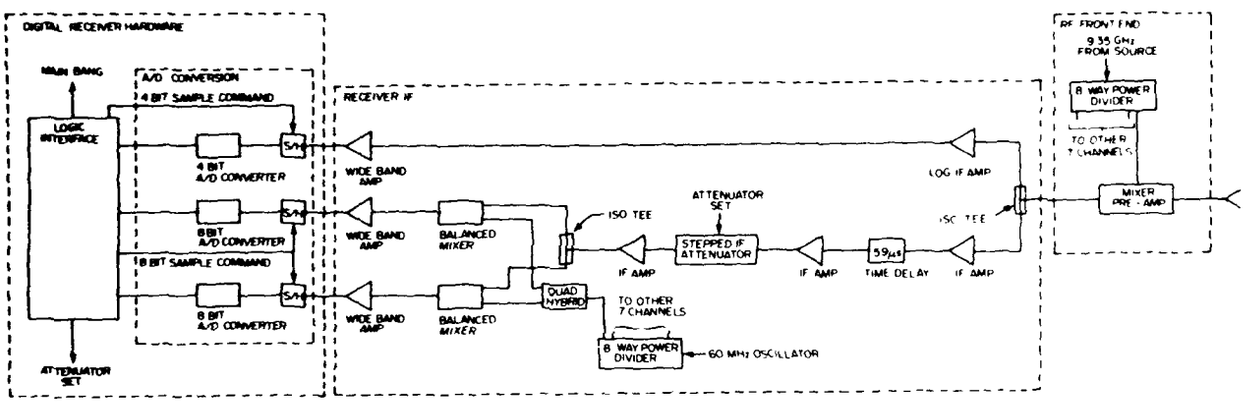

Figure 25. NRMRAD Receiver Subsystem

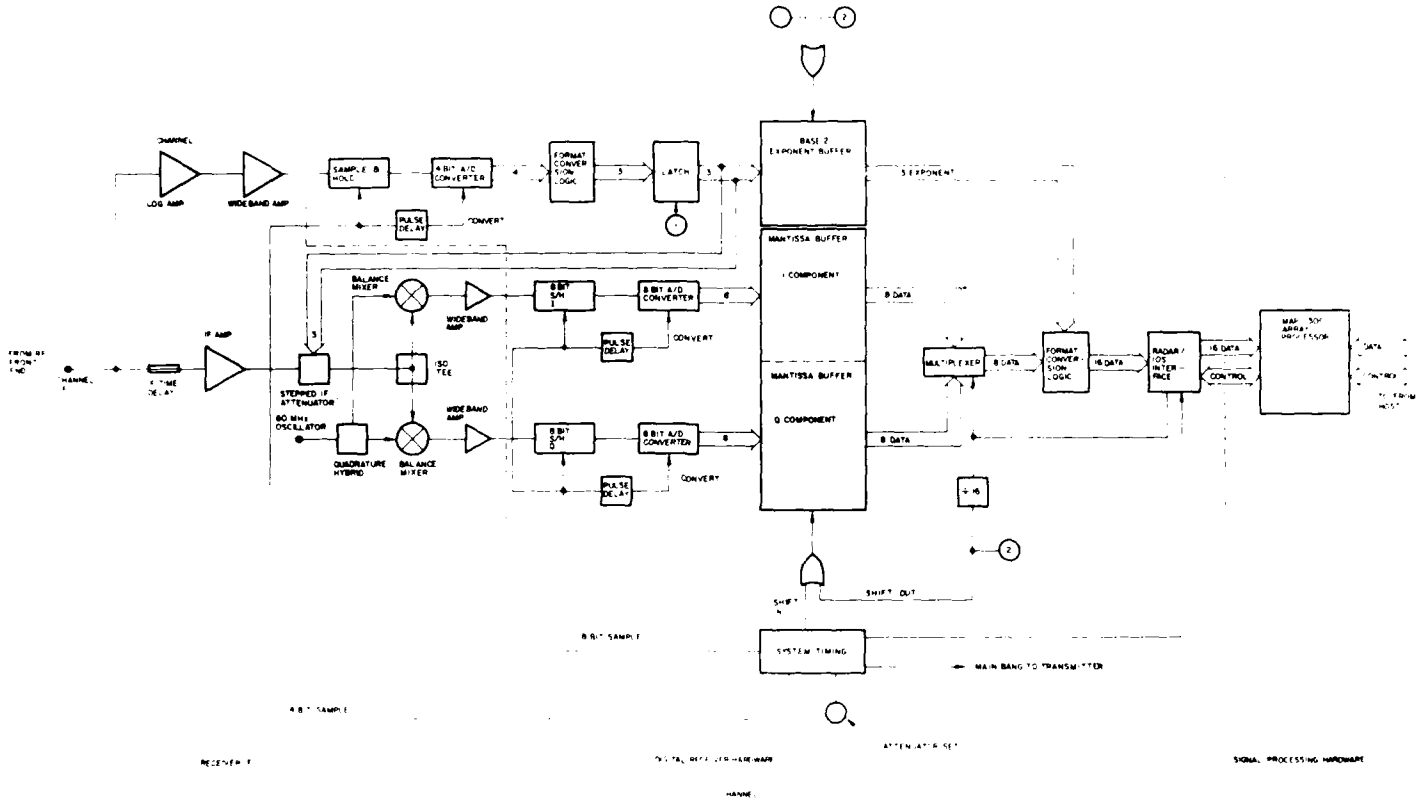

Figure 25. Receiver Realization. The receiver consists of eight I and Q channels. Channel 1 is shown with the log amplifier voltage scaling circuitry. Each receiver channel uses common scaling circuitry; that is, Channel 1 IF is used to determine the base 2 exponent for all eight channels. Seven of the I and Q receiver channels are not shown.

immediately preceding the acquisition [illegible]. [illegible] IF attenuator may be [illegible] [illegible] control lines which establish attenuation in the IF signal path. [illegible] available are 0, 6, 12, ..., 36, 42 dB. Scaled digital [illegible] voltage scaling mechanism installed in the IF signal path [illegible] has been derived. Scaling information contained within the [illegible] control lines serves as the 3-bit base 2 exponent. For example, if 12 dB is switched into the IF signal path in Figure 26, the IF voltage would be halved; then halved again; therefore the scaling factor must be 4 (2^2). Likewise, for 24 dB IF attenuation, the scaling factor is 2^4. With three control lines, the maximum base 2 exponent obtainable is 7, corresponding to 42 dB IF attenuation; minimum IF attenuation of 0 dB; corresponding to 2^0 or a scale factor of unity. Scaled I and Q analog components are input to wide-band amplifiers seen in Figure 26, then sampled for analog-to-digital (A/D) conversion. Timing of sequential events such as analog sample and pulse transmission are under control of system timing hardware. A/D conversion is initiated upon sample and hold output stabilization. The A/D converter digital output plus 3-bit base 2 exponent are temporarily stored in mantissa and base 2 exponent buffers. When data buffers are filled, the Massively Parallel Processor (MAP) array processor is informed of data availability via interface control logic. Under array processor control, the data is multiplexed from radar temporary storage through data conditioning logic into MAP memory for beam formation and Doppler processing.

The functional hardware discussion in the next section covers system timing, sample and hold circuits, analog-to-digital conversion, radar data buffers, format conversion logic, and radar processor interface.

4.1 NEMRAD (AMTI) System Timing

NEMRAD (AMTI) system timing circuitry, shown in Figure 28, sequences periodic transmitter and receiver functions (for example, pulse transmission and analog receiver signal sampling). The system timing circuitry consists of a 10-MHz clock oscillator, synchronous binary counters, and sense logic for detecting counter outputs.

The transmit pulse command (MAIN BANG), SAMPLE commands for the 4- and 8-bit analog-to-digital converters (ADC), the radar buffer memory shift in (SHIFT IN) commands, the ATTENUATOR SET command, and the radar buffer load (RADBUFFLD) command are derived from outputs of the binary counter string. A 10-MHz clock output is divided by 2^{15}, producing binary counter outputs Q_1, Q_2, ... Q_{15} and $\overline{Q}_1$, $\overline{Q}_2$, ... $\overline{Q}_{15}$. In addition to the original 100-ns clock pulse (CP) shown in Figure 27,

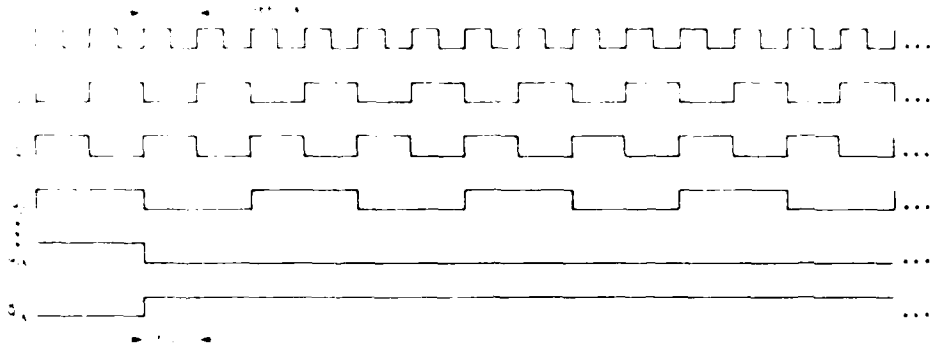

Figure 27. [illegible] Signal Binary Counter Outputs

Event [illegible] Q [illegible] Q_1, Q_2, ... Q_{13} = 0. Event time is calculated [illegible] 0. The relative time of each event is indicated [illegible] expressed in Q. For example, an event [illegible] Q [illegible] Q_{13} = 1; Q_{12}, Q_{11} ... Q_1 = 0; the relative event time would be calculated as:

Counter Output	Q_{13}	Q_{12}	Q_{11}	Q_{10}	Q_9	Q_8	Q_7	Q_6	Q_5	Q_4	Q_3	Q_2	Q_1
Binary Weight	2^{12}	2^{11}	2^{10}	2^9	2^8	2^7	2^6	2^5	2^4	2^3	2^2	2^1	2^0
Event Q [illegible]	1	0	0	0	0	0	0	0	0	0	0	0	0

$$\text{Event Time } (\Delta t) = \sum_{i=1}^{13} Q_i 2^{i-1} = Q_{13} \cdot 2^{12} \cdot 66.7 \text{ ns} = 273 \ \mu\text{s} .$$

Timing signals are derived from and locked to the radar 15-MHz [illegible]. The 15-MHz oscillator is not synchronized with the 60-MHz [illegible], 3-GHz [illegible], MAP clocks also run asynchronously with the radar 15-MHz system [illegible] oscillator. The 15-MHz clock is associated primarily with system timing [illegible] sampling events.

Typically, a timing command sequence would appear similar to Table 3. Timing signals referenced in Table 3 are defined in Table 4.

Table 3. Timing Command Sequence
Sixteen range cells are implemented in hardware; however, only three cells are shown in Table 3

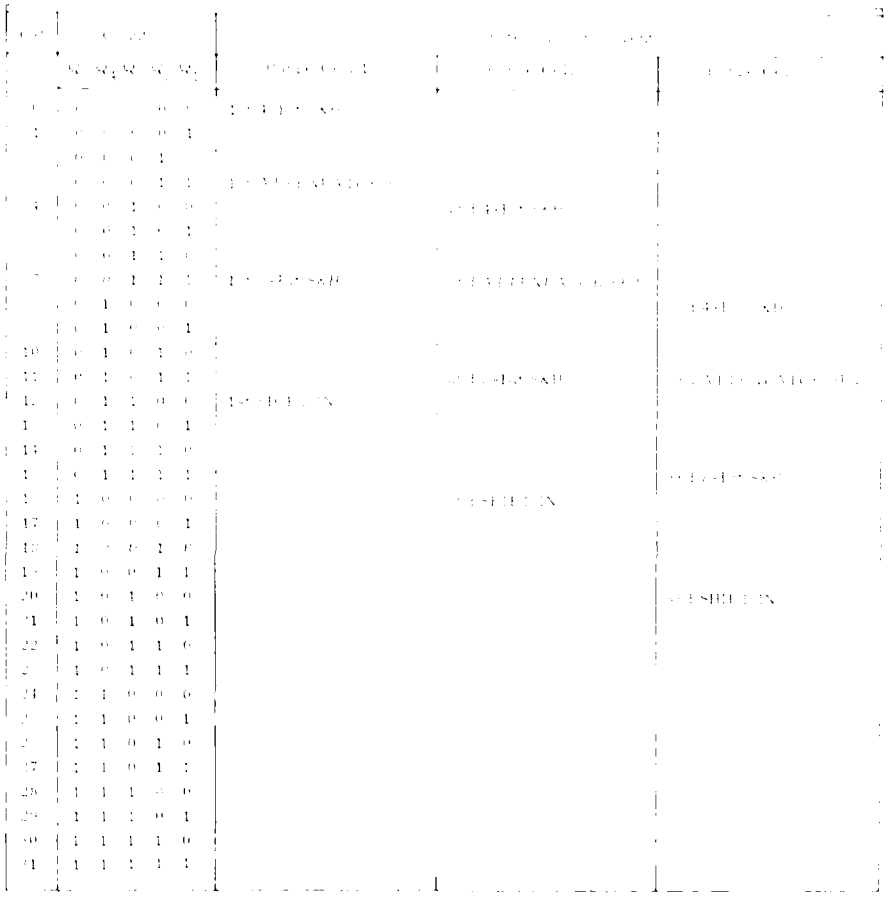

Table 4. [illegible]

[illegible]	
MAIN RANG	[illegible] pulse
4-bit SAMPLE	Sample [illegible]
8-bit SAMPLE	[illegible]
CONVERT	Begin [illegible]
END OF CONVERT	End [illegible]
ATTENUATOR SET	Set IF signal [illegible]
SHIFT IN	Shift [illegible]
SHIFT OUT	Shift [illegible]

1.2 Ultra High Speed Sample and Hold

[illegible] ultra-high-speed Sample and Hold (S&H) [illegible] I and Q wideband amplifier output [illegible] The S&H module utilized is [illegible] less than 20 ns with [illegible] [illegible] 4.1. [illegible] 4-bit SAMPLE [illegible] the S&H analog video and [illegible] During the SAMPLE [illegible] CONVERT control pulse is issued to the ADC. [illegible] The SAMPLE control pulse string [illegible] The SAMPLE control pulse group is issued [illegible] burst every 4 ms. Significant control signals used [illegible] are defined in the timing diagram of Figure 28.

1.3 Ultra High Speed Analog to Digital Converter

[illegible] Ultra-High-speed HI series 8-bit ADC's [illegible] The S&H analog input to an 8-bit binary [illegible] HADC-HI [illegible] ADC-HI series [illegible] 8-bit conversion at 10 MHz. The NEAREND CONVERT [illegible] 4 ns [illegible] 1 MHz. [illegible] following S&H output stabilization, CONVERT [illegible] A/D conversion. An END OF CONVERT (EOC) pulse is generated by the [illegible] ADC

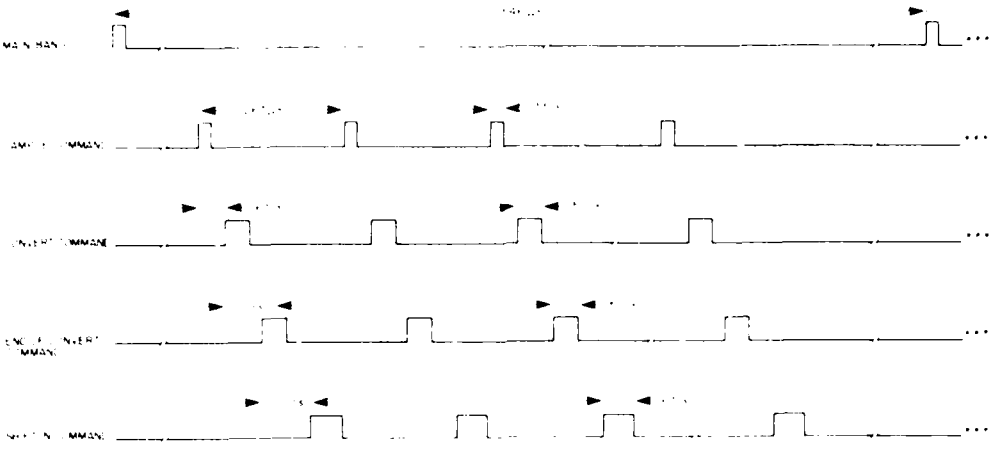

Figure 28. ADC Board Timing Signals

control. The EOC command is a TTL compatible 50 ns positive going pulse. EOC rising and falling edges are used to latch ADC output data in TTL buffer registers until SHIFT IN strobes output data into the Mantissa Buffer described in Section 4.4.1. Eight channels, one I and one Q component per channel, require 16 8-bit ADC's. Eight-bit SAMPLE command rising edge initiates synchronous S&H and ADC cycles for the A/D conversion hardware shown in Figure 28.

4.4 Radar Data Buffer

Two 8-bit mantissas (I and Q components), in conjunction with a 3-bit exponent, define the amplitude and phase of one channel range sample. Each channel is divided into 16 range samples separated in space by 131.0 (40 m). The mantissa storage buffer is loaded under control of radar system timing circuitry discussed in Section 4.1. Following the lapse of a selectable range counter timing interval (referenced to t = 0 of Section 4.1), system timing circuitry dictates the region where range samples will be taken. Sixteen sample and hold modules synchronously respond to the master timing 8-bit SAMPLE command. Following each sampling, a CONVERT command is issued to 16 A/D units. At the conclusion of A/D conversion, eight data channels consisting of two 8-bit words per channel are ready for loading into the radar mantissa buffer. One 3-bit positive base 2 exponent is stored per range sample in base 2 exponent storage buffer. Data representing one range sample over eight channels consists of 16 8-bit words stored in inverted offset binary format (defined in Section 4.5.1), plus one positive 3-bit base 2 exponent. Eight digital I components, plus eight digital Q components, are

synchronously loaded in parallel into the mantissa buffer under the control of the master timing circuitry. The base 2 exponent is loaded in parallel prior to the loading of the mantissa buffer (one 3-bit exponent per range bin). The mantissa and exponent buffers are implemented with TTL shift registers; therefore the first range bin loaded per channel will be the first range bin shifted out when unloaded into the array processor.

A diagram depicting the parallel loading of the radar data buffer is shown in Figure 29. The data load commands, hereafter referred to as SHIFT IN commands are generated by the radar system timing. The buffers are completely filled following the 16th SHIFT IN command.

Data is multiplexed out of the mantissa buffer in a serial string of 256 8-bit words. The unload buffer commands or SHIFT OUT commands are under software control of the array processor (MAP-300) Input Output Scroll (IOS) board. The IOS board is the input/output interface used to pass radar data to the array processor memory. Data contained in the mantissa buffer is read out by component, channel, and finally range bin. The pecking order of the data multiplexer is depicted in Table 5. The multiplexer strobes 16 words from one range bin and recycles with a SHIFT OUT command to advance shift register data forward toward the multiplexer in Figure 29.

Table 5. Mantissa Buffer Data Multiplexer Pecking Order

Position in Serial Word Train	Signal Component Description (8-Bits Wide at Output of Mantissa Buffer)
1	Channel 1, I Component, Range Bin 1
2	Channel 1, Q Component, Range Bin 1
3	Channel 2, I Component, Range Bin 1
4	Channel 2, Q Component, Range Bin 1
.	.
.	.
.	.
14	Channel 7, Q Component, Range Bin 1
15	Channel 8, I Component, Range Bin 1
16	Channel 8, Q Component, Range Bin 1
17	Channel 1, I Component, Range Bin 2
.	.
.	.
.	.
255	Channel 8, I Component, Range Bin 16
256	Channel 8, Q Component, Range Bin 16

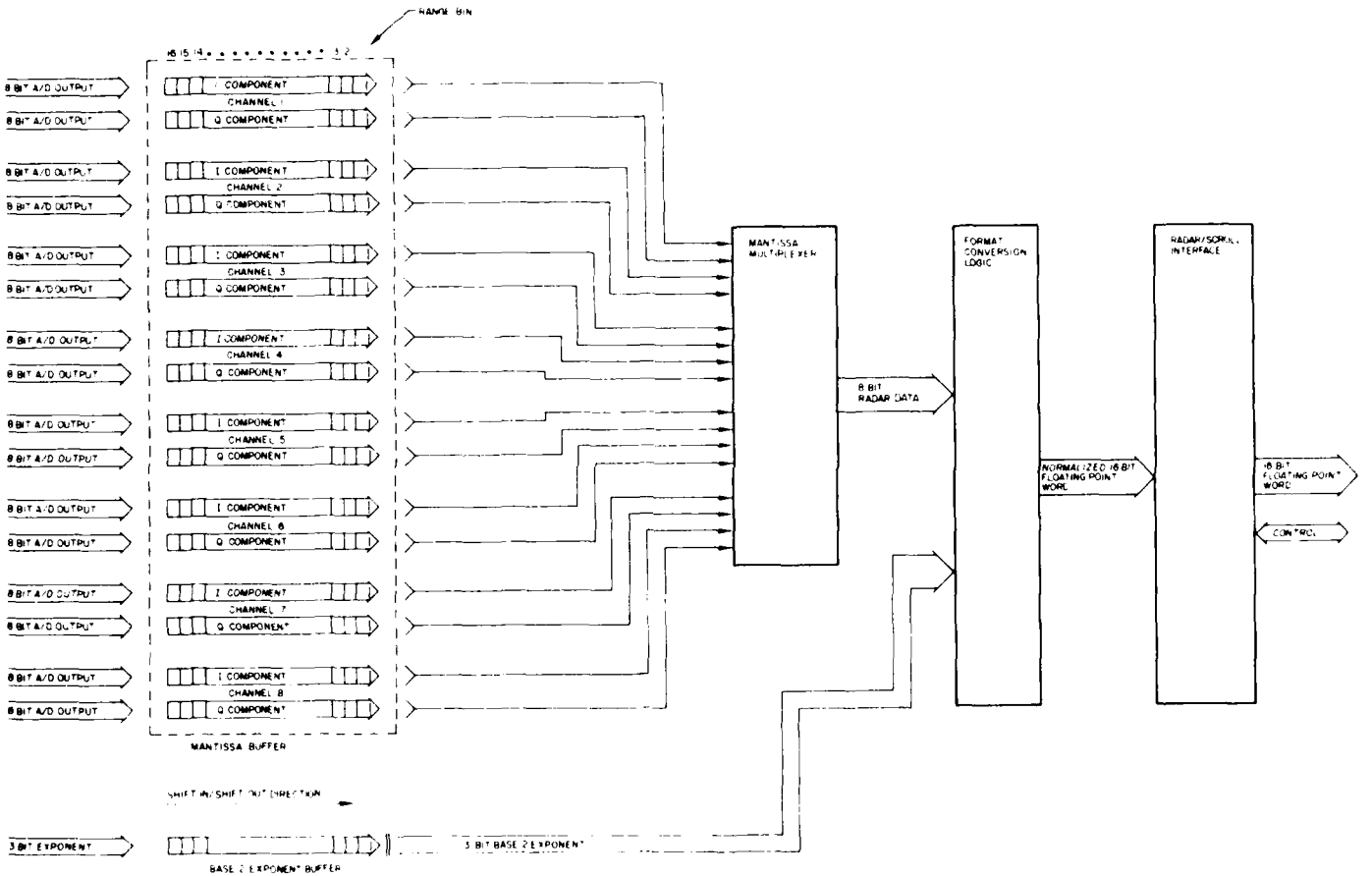

Figure 29. Mantissa and Exponent Shift Register Buffer with 8-Bit Wide Data Multiplexer. SHIFT IN commands originate from the radar master timing. SHIFT OUT commands originate from the array processor I/O interface

The output data train is combined with a 3-bit base 2 exponent and directed through format conversion hardware to insure radar data format compatibility with that of the array processor. Details of the format conversion hardware are discussed in Section 4.5.

4.4.1 MANTISSA BUFFER

Radar digital data is stored in shift register memory during the interpulse period until the radar initiates an array processor input cycle. The shift register memory may be visualized as a data matrix built of 8-bit word elements. The eight-channel receiver outputs an inphase and quadrature analog component per channel. Sixteen analog range samples are taken at 267-ns intervals; therefore, the data matrix is organized by row with regard to range cells and by column with respect to channels. A data matrix is loaded into shift register memory following every transmitted pulse. An I and Q 8-bit word is loaded for 8 channels and 16 range cells, generating a matrix of 16 range cell rows and 8 complex channel columns (256 8-bit words). The mantissa buffer shown in Figure 30 obtains input data from Datel 8-bit A/D converters. The output from the data buffer is directed into an array processor via Format Conversion Logic.

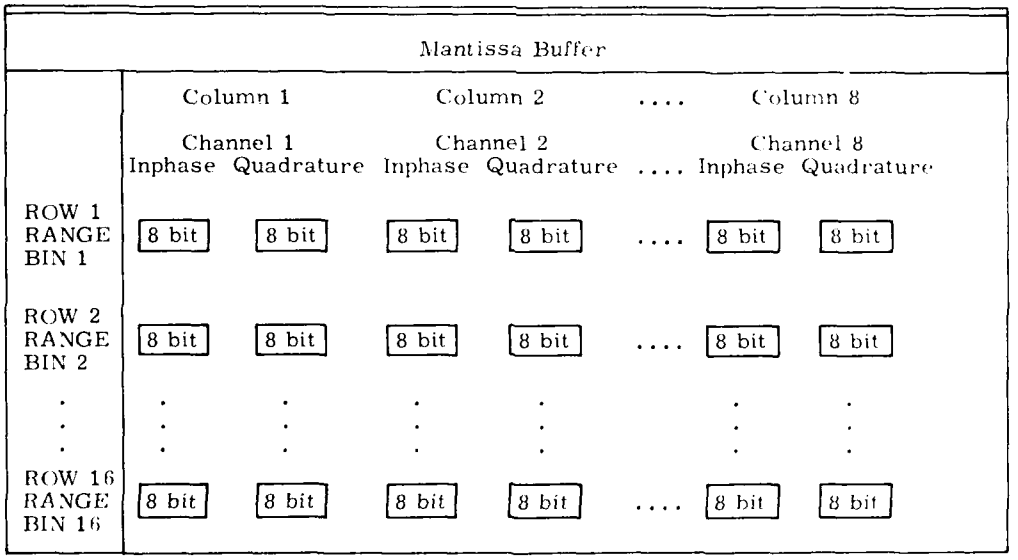

Figure 30. Radar Receiver Mantissa Buffer (256 8-Bit Words)

4.4.2 BASE 2 EXPONENT BUFFER

Each of 16 range bins is associated with one positive 3-bit exponent that characterizes the effective gain of 8 channels. The 3-bit exponent can vary from range bin to range bin if the stepped attenuators are in the automatic mode of operation. If the step attenuators are operated in the manual mode, the 3-bit exponent will stay constant for 16 range bins. The exponent is stored in a shift register array 3 bits wide and 16 range bins deep. The array input comes from conversion logic following the 4-bit A/D converter sampling the log of channel 1 IF when in automatic operation. The logarithm of the channel 1 IF signal is provided by an analog logarithmic amplifier. Channel 1 IF signal is split using an Isotec or power splitter. Half of channel 1 IF signal power is used as input to the logarithmic amplifier. The log amplifier output ultimately determines the IF signal attenuation required for eight channels. The remainder of channel 1 IF signal power is time delayed by utilizing coax cable. Channels 2 through 8 IF signal power is attenuated by 3 dB and delayed in a fashion identical to channel 1. The log amplifier output is sampled and converted to a 4-bit word. The 4-bit A/D output is converted to a 3-bit IF attenuator control word, which establishes the IF signal attenuation required in all eight channels and the base 2 exponent as a function of range bin. Establishing the necessary IF attenuation requires time for A/D conversion, 3-bit conversion, and attenuator setting and stabilization. Channels 1 through 8 are delayed for the time required to establish the appropriate IF signal attenuation. While in manual operation, the 4-bit A/D output is bypassed, and the 3-bit exponent is hardwired in and loaded following each 4-bit SAMPLE command.

4.5 Data Format Conversion Logic

Format conversion hardware transforms the 8-bit A/D output and 3-bit base 2 exponent into a normalized 16-bit floating point data word. The 16-bit floating point format is compatible with the input requirements of the CSPI MAP array processor. Format conversion logic follows the output of the radar data buffer multiplexer in Figure 26. Radar data is transferred from the mantissa and exponent buffers through data conditioning (format conversion) logic and into the array processor. Data format conversion could have been implemented in array processor software; however, due to the process speed requirements of our real-time operating environment, format conversion was necessarily implemented in hardware.

4.5.1 ANALOG-TO-DIGITAL CONVERTER INPUT AND OUTPUT SPECIFICATIONS

a. Input voltage range for 8-bit Datel hybrid input analog-to-digital converter ranges from -1.27 V to +1.28 V. Digital output coding for Datel model ADC-UH series is referenced as inverted offset binary, as defined in Table 6.

b. From Table 6, A/D input sensitivity is 10.0 mV per bit.

c. The A/D converters used perform an 8-bit conversion in 0.1 μs (10-MHz conversion rate).

Table 6. Datel ADC Output Format

Datel Analog to Digital Converter Inverted Offset Binary Output								
Analog Input Voltage + or - polarity (volts)	Output Bit Pattern bit position 7 (MSB)	6	5	4	3	2	1	0 (LSB)
-1.27	1	1	1	1	1	1	1	1
-0.64	1	1	0	0	0	0	0	0
0.00	1	0	0	0	0	0	0	0
+1.27	0	0	0	0	0	0	0	1
+1.28	0	0	0	0	0	0	0	0

4.5.2 8-BIT INVERTED OFFSET BINARY FORMAT CONVERSION TO 8-BIT SIGN MAGNITUDE FORMAT

The first stage of format conversion following the ADC output is dedicated to transforming the ADC output of sign magnitude format. If bit 7 is sensed to be set, the 8-bit data word is transferred directly through the first section of digital logic without modification. However, if bit 7 is not set, the conversion logic performs a 2's complement operation on bits 0 through 6 with one exception. If bits 1 through 7 are not set, bit 7 remains unchanged while bits 0 through 6 are set.

Table 7 defines logical input and output states for the first stage of format conversion circuitry. Equation (1) relates the A/D input voltage to sign magnitude binary components m_7, m_6, ... m_0 before combination with base 2 exponent.

Table 7. Sign Magnitude Format

Analog Input Voltage	Format Conversion Input								Format Conversion First Stage Output							
(volts)	Inverted Offset Binary bit position								Sign Magnitude bit position							
	7 MSB	6	5	4	3	2	1	0 LSB	7 SIGN	6 MSB	5	4	3	2	1	0 LSB
	d_7	d_6	d_5	d_4	d_3	d_2	d_1	d_0	m_7	m_6	m_5	m_4	m_3	m_2	m_1	m_0
-1.270	1	1	1	1	1	1	1	1	1	1	1	1	1	1	1	1
-0.640	1	1	0	0	0	0	0	0	1	1	0	0	0	0	0	0
-0.010	1	0	0	0	0	0	0	1	1	0	0	0	0	0	0	1
0.000	1	0	0	0	0	0	0	0	1	0	0	0	0	0	0	0
+0.010	0	1	1	1	1	1	1	1	0	0	0	0	0	0	0	1
+0.640	0	1	0	0	0	0	0	0	0	1	0	0	0	0	0	0
+1.270	0	0	0	0	0	0	0	1	0	1	1	1	1	1	1	1
+1.280	0	0	0	0	0	0	0	0	0	1	1	1	1	1	1	1

$$V^{smag} = (-1)^{m_7} (10\ mV) \sum_{i=0}^{6} 2^i m_i \qquad (1)$$

where

V^{smag} — input voltage to 8-bit A/D

$m_6, m_5, \ldots m_0$ — binary data bits

m_7 — sign bit .

4.5.3 8-BIT SIGN/MAGNITUDE MANTISSA WITH POSITIVE 3-BIT BASE 2 EXPONENT CONVERSION TO 16-BIT FLOATING POINT FORMAT WITH BASE 16 EXPONENT

The 12-bit radar data word is defined as shown in Table 8 following the combination of sign/magnitude format and positive base 2 exponent. The A/D input voltage expressed (as seen at output of sign magnitude format conversion logic after combination with base 2 exponent) in terms defined by Table 8 is seen by Eq. (2).

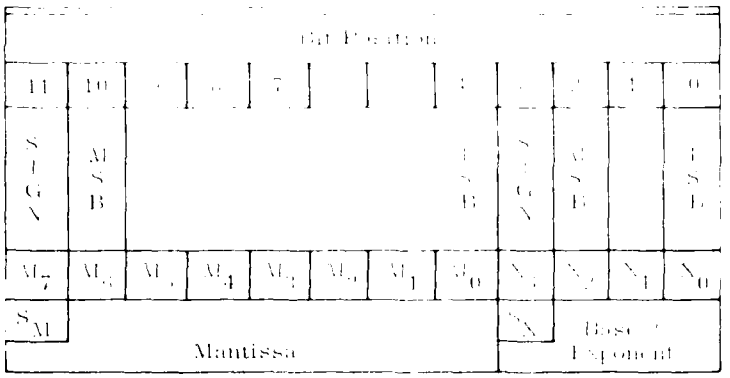

$$V^{smagx} = 2^{(4x_2+2x_1+x_0)} V^{smag}$$

$$V^{smagx} = (-1)^{S_M} (10\ mV)\, e^{(4x_2+2x_1+x_0)} \sum_{i=0}^{7} 2^{i} m_i \qquad (2)$$

where

S_M = Sign bit of mantissa

S_X = Sign bit of base 2 exponent (0 if $x_2x_1x_0$ positive or $S_X = 0$)

$m_7 m_6 m_5 \ldots m_0$ = binary mantissa bits

$x_2 x_1 x_0$ = exponent bits

Bit positions are defined in Table 8.

The radar data word of Table 8, following conversion to a 16-bit floating point word, is defined as shown in Table 9 and Eq. (3). Equation (2) yields the 2-to ADC input voltage as seen by the MAP.

$$V^{MAP} = (-1)^{S_E + S_M} \sum_{k=1}^{3} \frac{H_k}{10^k} \qquad (3)$$

where

exp is derived from S_e, e_2, e_1, e_0.

S_e is the sign of the base 16 exponent.

If exp > 0, (S_e = 0) then

$$exp = 4e_2 + 2e_1 + e_0$$

If exp < 0, (S_e = 1) then e_2, e_1, and e_0 are in 2's complement form. Perform 2's complement operation on e_2, e_1, and e_0, yielding e'_2, e'_1, and e'_0; then

$$exp = -(4e'_2 + 2e'_1 + e'_0) .$$

H1, H2 Hex digits converted to base 10.

H3' Hex digit with LSB deleted converted to base 10.

Bit position for arguments of Eq. (3) are defined in Table 9.

Table 9. MAP Base 16 Floating Point Half-Word Format

Bit Position															
15	14	13	12	11	10	9	8	7	6	5	4	3	2	1	0
SIGN	MSB										LSB	SIGN	MSB		LSB
h_{11}	h_{10}	h_9	h_8	h_7	h_6	h_5	h_4	h_3	h_2	h_1	h_0	e_3	e_2	e_1	e_0
S_h	H_1				H_2				H'_3			S_e	Exponent		
Hex Mantissa												Base 16 Exponent			

Equation (3) relates the voltage observed by the MAP to the hex components identified by Table 9.

Equation (2) is *not equivalent to* Eq. (3). The MAP defined voltage, V^{MAP}, differs from $V^{Strain gx}$ by a constant multiplier.

$$V^{Strain gx} = (10 \text{ mV})(2^7)V^{MAP}$$

$$V^{smagx} \quad (10\ mV)(2^7)(-1)^{S_h}\ 16^{exp} \sum_{k\ 1}^{3} \frac{H_k}{16^k} \quad .$$

Equation (4) allows one to predict the A/D output utilizing Table 9, MAP hex voltage representation, and the IF attenuator settings x_2, x_1, and x_0. Equation (4) allows the conversion of MAP base 16 data to A/D input voltage.

$$V^{smag} \quad (-1)^{S_h} (2^7) \frac{(10\ mV)(16^{exp})}{2^{(4x_2+2x_1+x_0)}} \sum_{k\ 1}^{3} \frac{H_k}{16^k} \quad . \tag{4}$$

Equation (4) is useful when relating A/D voltage input observations to MAP voltage observations used in processing. Equation (4) may also be used to insure A/D linear operation by insuring that the input voltage specifications are never exceeded.

4.5.4 NORMALIZATION OF 16-BIT FLOATING POINT WORD

The 16-bit data word is normalized in hardware to insure H1 ≠ 0 (unless H1, H2, and H3 = 0). If hex shifts are required for normalization, the base 16 exponent is decremented accordingly.

4.6 Input/Output Scroll (IOS) Interface

Discussion of the IOS interface will be developed primarily around data and control interface hardware. An event timing diagram is presented with references to RADAR/IOS handshake control signals. Interface test hardware is presented in addition to detailed discussion regarding real-time data status indication. Data transfer rates realized are presented, and the data double buffering input scheme implemented is discussed. Radar data is transferred from the radar data storage buffer through format conversion logic and into an array processor under control of the array processor interface board (IOS).

4.6.1 16-BIT NORMALIZED FLOATING POINT WORD TRANSFER FROM RADAR TO IOS INTERFACE

Real-time radar operational constraints require all signal processing and data transfers be completed within one interpulse period. Data transfer rates must be high to insure maximum signal processing. The radar/IOS interface and conversion logic realize a 16-bit MAP full word transfer in approximately 0.30 μs; 120 μs is needed for 32-bit MAP full word transfer (≈ 1.04 μs to transfer 128 MAP full words, ≈ 546 μs per interpulse period).

4.6.2 RADAR MAP-300 IOS INTERFACE CONTROL AND TIMING SIGNALS (Figure 31, Table 10)

The array processor (IOS interface) informs the radar that the IOS processor has started via signal IOSRUN. Following activation of IOSRUN, the IOS interface informs the radar that processing is complete and the IOS is waiting for data, via PAUSE control signal. The radar responds to the processor data request following the filling of the radar mantissa and exponent buffer discussed in Section 4.4. When the mantissa and exponent buffers are filled with new data, the radar informs the processor that data is ready by issuing the interface control signal CLRPAUSE. The PAUSE signal and CLRPAUSE signals insure that the data transfers are synchronized and new data is transferred. PAUSE is active until cleared by radar, that is, the array processor must complete all processing and data transfers within one interpulse period, and must wait until radar data is ready. The IOS then requests data, utilizing the leading edge of control signal IOSIN. Data input request is acknowledged by radar, utilizing control signal IOSACK, and the data is transferred (in handshake fashion) on the trailing edge of IOSIN. A total of 128 complex word transfers takes place in 154 μs, then processing is initiated. Three control lines were used to monitor radar data integrity and insure that the MAP did not drop a pulse by missing a data matrix, or transfer data as the radar data buffer was being updated.

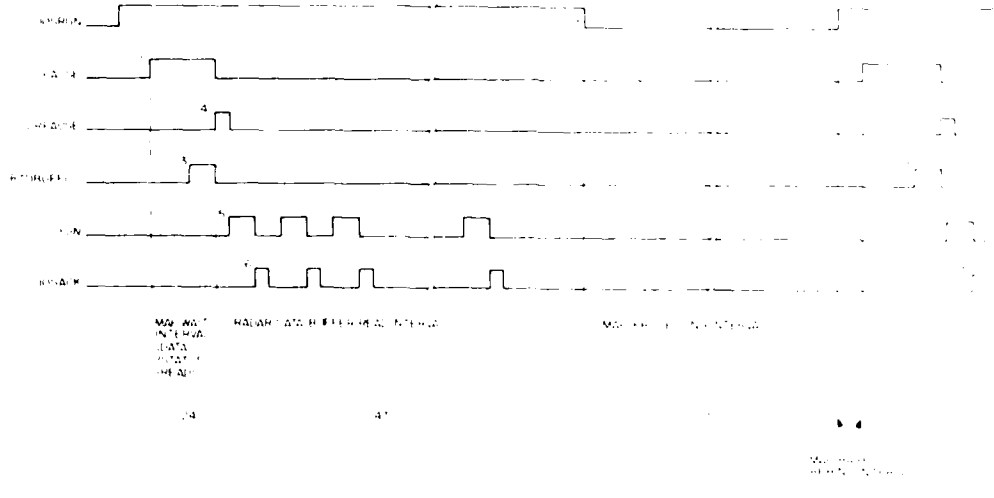

Figure 31. Radar IOS Interface Control and Timing Signals. Only the most significant control and timing signals are shown. Active signal levels shown do not accurately reflect interface. Positive logic was used for discussion purposes.

Table 10. Radar IOS Interface Control and Timing Signals
Active interface logic levels are not necessarily as shown

Edge Number	Name	Classification	Message
1	IOSRUN	MAP IOS interface control	Scroll is running
2	PAUSE	MAP IOS interface control	MAP waiting for data
3	RADBUFFLD	Radar timing	Radar mantissa and exponent buffers start load cycle.
4	CLRPAUSE	Radar interface control	Falling edge of RADBUFFLD indicates buffer load complete. This event triggers CLRPAUSE implying new data available.
5	IOSIN	MAP IOS interface control	Leading edge of IOSIN requests data transfer *from radar.*
6	IOSACK	Radar interface control	Leading edge of IOSACK acknowledges data request causing data transfer on trailing edge of IOSIN.
7	IOSRUN	MAP IOS interface control	Radar to MAP data transfer complete, scroll is halted.

4.6.3 DATA STATUS INDICATOR

Three data status lines are provided under radar control to indicate data integrity. NEMRAD Doppler processing requires a constant time lapse from data group to data group; therefore, the loss of one pulse data group during a coherent processing interval is intolerable. If the array processor requires more than one interpulse period for beam formation and Doppler filter processing, invalid data will be transferred into the MAP. The radar is tasked with monitoring data integrity and reporting data status to MAP. Radar interface logic monitors transfer control signals and internal timing commands to determine data status. If the IOS requires *more than 546 μs between data requests,* the radar hardware writes over data stored in the radar buffer.

New radar data may become available at the ADC output as the MAP transfers data under IOS control. In this situation, new data would be shifted in the mantissa

[illegible] exceed buffers under [illegible] IOS [illegible]. At least [illegible] radar buffer [illegible]. The radar data is lost. [illegible] read interval [illegible]. A read interval [illegible] radar data buffer read was in progress [illegible] IOS [illegible].

[illegible] available [illegible] the radar buffer [illegible] before the IOS [illegible] starts running, data is said to be [illegible] the MAP processing interval. Radar buffer loaded (RADBUFLD) generates the CLRPAUSE signal, which normally would kick the IOS [illegible] and start data transfer if the IOS were in a software wait loop (that is, PAUSE ACTIVE). When CLRPAUSE is issued and PAUSE is not active, the CLRPAUSE pulse is [illegible] the IOS; therefore, the IOS is not aware that new data has been loaded [illegible]. Later, the Scroll starts running and activates the PAUSE signal. The PAUSE [illegible] not be cleared until the radar buffer is once again filled [illegible] CLRPAUSE [illegible] generated. At least one data pulse will be lost under this [illegible]. [illegible] nature is referred to as a *process interval error*.

If radar data becomes available after the IOS [illegible] the IOS has exerted PAUSE, the MAP is said to be [illegible]. [illegible] CLRPAUSE is issued before PAUSE is active, [illegible] PAUSE waits until the next radar buffer load for a CLRPAUSE [illegible].

4.7 Receiver Simulator Hardware

Receiver simulator hardware was developed for the purpose of [illegible] interface hardware and software diagnostics. [illegible] removed from the IOS data input port. Simulated radar data [illegible] received data at the IOS input port by interchanging the [illegible] board 18, with the receiver simulator card (Figure [illegible]) [illegible] of Figure 32.

The receiver simulator card provides a [illegible] Interface. Typically, the data matrix may be characterized by 128 [illegible]; 15 range cell voltage magnitudes are small compared to [illegible] total cells. Every phase angle contained within the simulated [illegible], or I equals Q for all 16 range cells. Every range cell signal is constant in amplitude and phase from pulse to pulse; however, the cell with relatively large amplitude may be moved to any of the 16 cells by the use of a series of four toggle switches numbered 0 through 3 shown in Figure [illegible]. Voltage magnitudes [illegible] within the simulated data matrix may be altered, and are determined by [illegible] 16-pin header chips mounted on the simulator card shown in Figure [illegible].

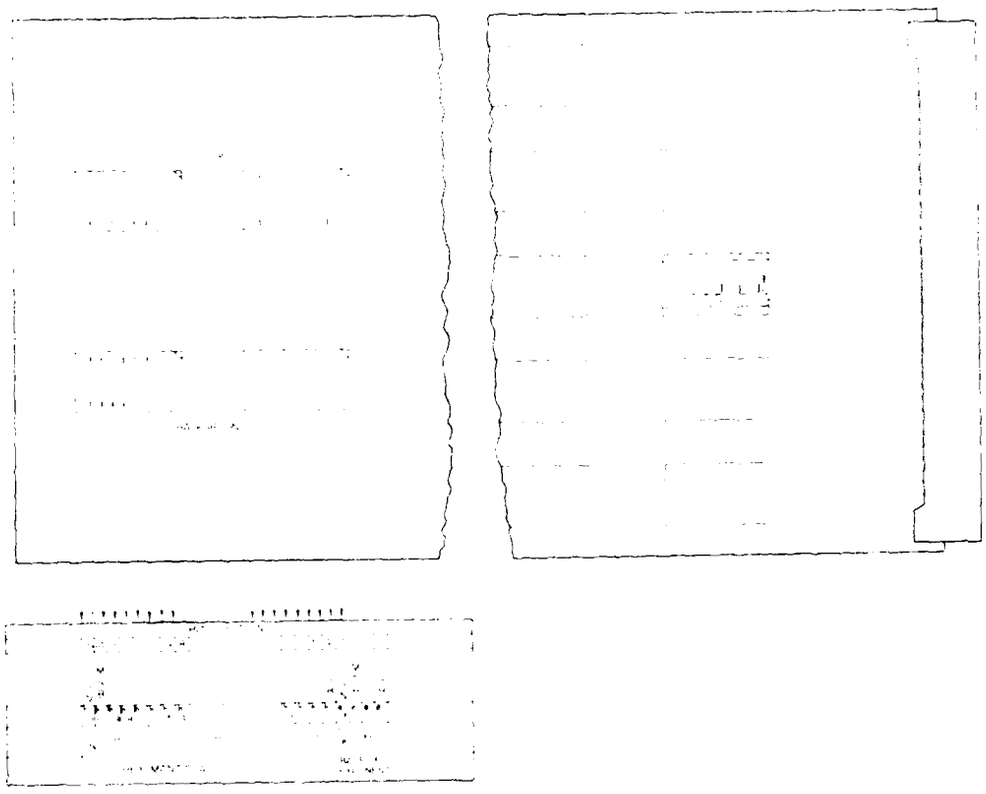

The [illegible] leaders [illegible] of the single relatively [illegible] range cell of the [illegible]. The [illegible] establish the magnitude of the remaining 1 cells. A leader [illegible] shifting [illegible] establishes [illegible] corresponding bit position. The leader chip bit configuration is shown in Figure [illegible] and the MAP [illegible] data format is defined in Table 9. The leader [illegible] the magnitude of both I and Q components; therefore, the complex range magnitude observed by the MAP equals √2 times the data word as defined by the leader [illegible] part. The function of each digital circuit board is defined in Table 11.

Table 11. Digital Circuit Board Function Definition

Board	
1	System [illegible] 1
2	System [illegible]
[illegible]	Channel 1-8 [illegible]
4	Channel 1 Mantissa Buffer
[illegible]	Channel 2 Mantissa Buffer
[illegible]	Channel 3 Mantissa Buffer
7	Channel 4 Mantissa Buffer
8	Channel 1-8 Mantissa [illegible]
[illegible]	Channel 5 Mantissa Buffer
10	Channel 6 Mantissa Buffer
11	Channel 7 Mantissa Buffer
12	Channel 8 Mantissa Buffer
14	Mantissa Sign Magnitude Format Conversion
[illegible]	Radar [illegible] Interface
[illegible]	Base 16 Format Conversion
[illegible]	[illegible] Test Control

5. SYSTEM SOFTWARE

System processing functions are implemented in the CSP-30 [illegible] computer and MAP-300 array processor. CSP-30 and MAP-300 processors [illegible] operate as system maintenance tools. Maintenance and real-time operational software is presented throughout the following discussion.

The Computer Signal Processor (CSP) minicomputer is a 16-bit [illegible] with 32 K of interleaved core memory contained within the mainframe. [illegible] 1900s solid-state memory overlay the lower core sectors [illegible]. Peripherals [illegible] used in support of CSP-30 operation and software development include a [illegible] disk, line printer, [illegible] reader, cartridge tape units, [illegible]. The CSP-[illegible] [illegible] [illegible] (SD).

Six processors are contained within the MAP-300 [illegible]. [illegible] six processors [illegible] MAP [illegible] [illegible] handles [illegible] the MAP-300. A second [illegible] processor, the host interface module (HIM), [illegible] transfer from CSP-30 to MAP-300. A third processor (CSPU) [illegible] processor activity for the remaining [illegible] processors [illegible] report their status via flags to the CSPU. [illegible] six processors [illegible] arithmetic operations. The [illegible] processor units (APU's) [illegible] and are tasked with beam formation and Doppler filtering [illegible] the real-time radar operating environment. The remaining processor, the address processor [illegible] (APS), generates addresses for the APU's.

System initialization, real-time operation, and maintenance software are [illegible] Sections 5.1 through 5.4.

5.1 CSP-30/MAP-300 System Initialization Software

The purpose of initialization software is to measure the gain and phase differences of channels 2 through 8 to that of channel 1. A stationary reflector is placed [illegible] to the eight-element receive array (reflector [illegible]). A point source [illegible] on the receive aperture. There are 64 pulse returns averaged, [illegible] illuminating the target. The phase and gain differences of channels 2 through 8 are calculated with reference to channel 1. Channel [illegible] are calculated in the form of complex multipliers. These gain and phase correction factors are used as linear multipliers to modify the system [illegible] coefficients. The experimental layout for system initialization is described in section [illegible].2.1.

During the course of system initialization, the MAP processor is tasked with averaging 64 pulse returns. After 64 pulses are averaged by the MAP, the largest voltage magnitude from channel 1 is chosen *from* the group of 16 range bins. The range cell containing the largest voltage amplitude is the range cell containing the stationary reflector used for channel 2 through 8 normalization. The range cell containing the reflector is first determined, and *then* the eight complex average voltages chosen from the range cell containing the reflector are transferred to the host minicomputer.

These averaged voltages represent a planewave parallel to the face of the eight-element receive array. This voltage data is used by CSP-30 software to calculate an amplitude and phase correction factor. The software correction factors are normalized to channel 1 (that is, the remaining seven channels are normalized in phase and amplitude to channel 1). Once the CSP-30 receives the eight-element voltage array, the CSP-30 software calculates antenna weight correction factors normalized to channel 1. The eight-element receive array scattering matrix and the average voltage array transferred to the host by the MAP are used to determine the antenna weight correction factors.

CSP-30 software modifies AMTI and NEMRAD beam-forming coefficients to reflect system channel gain *and phase* variations, and then transfers the modified beam-forming coefficients and the Doppler filter coefficients to the MAP processor. The CSP-30 function during initialization is to supply the MAP with corrected beam-forming coefficients and *Doppler filter coefficients (Doppler coefficients are not* altered during initialization).

5.2 CSP 30/MAP 300 Real-Time Operation

In real-time operation, the MAP-300 APUs are responsible for AMTI and NEMRAD beam-formation calculations. Typically, a beam-forming calculation over a single range cell would involve eight complex multiplications and a summation of complex products over eight channels. The APUs are also tasked with Doppler filter implementation. Two identical Doppler filters are implemented within the MAP; one filter is for NEMRAD and one is for AMTI processing. To implement a single filter over one range cell requires 64 pulse returns, 64 complex multiplications and a circular-buffer sum for a single range cell.

The IOS is responsible for transfer of receiver data from the radar into MAP memory. The HIMI is tasked with the transfer of processed radar data from MAP memory into CSP-30 memory.

A summary of MAP real-time functions indicates this group of six MAP processors is tasked with NEMRAD/AMTI beam formation, NEMRAD/AMTI Doppler processing, and data transfer from the radar and into the CSP-30.

CSP-30 real-time processing functions consist of detection processing, processed data recording, and driving a CRT display. Under real-time operating conditions, the CSP-30 signal processor is almost exclusively utilized to record processed NEMRAD and AMTI voltage magnitudes, and data batch status. Processed data is recorded to cartrifile tape for more sophisticated detection processing at a later time. Detection processing is discussed in detail in Section 6.2.4.

5.3 Maintenance Software

Maintenance software consists of a group of programs designed to aid in receiver hardware troubleshooting and diagnosis. Using the array processor in conjunction with the host minicomputer and line printer, hardware diagnosis software is used to insure that the eight-channel receiver is operational. If a problem is detected, maintenance software is used as a troubleshooting tool.

MAP maintenance software consists of a straightforward transfer of receiver data from the receiver into the host minicomputer. MAP-300 maintenance software transfers one 128 complex word array of radar data into a block of MAP memory, then the HIM transfers the entire block of unprocessed data into CSP-30 memory. During system maintenance, the MAP serves only as a receiver data funnel. No numerical processing responsibilities are placed on the MAP during the maintenance mode of operation.

CSP-30 maintenance software consists of several programs. One program entitled MDS (Minimum Detectable Signal) is written to run with the receiver in a maintenance configuration. The function of this software is the generation of an I/O transfer characteristic for each receiver channel. Typically, low-power RF CW is coupled into each channel of the RF front end. The RF energy phase and power level is under control of external test hardware (phase shifter and wave guide attenuator). Data is collected over a range of input power levels from approximately -100 dBm to -10 dBm. At the conclusion of the test, eight I/O curves are produced, relating receiver input power to output power or voltage.

A second maintenance routine, entitled BITCHECK, was written to gain insight into receiver operation with constant power input. Generally, the receiver input may be RF CW at constant phase and power, or noise. Independent samples are taken and compiled over an extended period of time, and a histogram is produced showing the number of observations as a function of the output voltage magnitude. An example of this routine operation is as follows: With no signal present, only noise is present at the output of the receiver. By noting how much ADC dynamic range is consumed by the system noise, the dynamic range lost due to noise may be determined.

5.4 MAP Software

Repeating the MAP architecture for use in Section 5.4 discussion, there are six processors within the MAP-300, all of which operate asynchronously: the host interface module (HIM) for communication between the CSP-30 host machine and the MAP-300, the I/O scroll (IOS) for communication between the radar and the MAP-300, the central signal processing unit (CSPU) for overseeing the entire task and controlling the other processors, the two arithmetic processing units (APU) which run in parallel, and the addresser processing scroll (APS) which generates a stream of input and output addresses for the APU. The various processors are loaded with the necessary programs, started by the CSPU, and their status is reported to the CSPU by the setting or clearing of flags.

5.4.1 MAP INITIALIZATION

The system initialization function and purpose is described in Section 5.3.1. Section 5.4.1 reviews MAP processor activity when the system initialization program is executed.

Initially, the host signals initialization code to the MAP-300 to load the program containing all 1's. The CSPU zeros a 512-word block of memory (called IOS-1) which will be used for numerical summation. The CSPU then loads the IOS with a radar-to-MAP data transfer program, loads the APU with a data averaging program, and loads the APS with the corresponding addressing program.

For 64 times, the CSPU turns on the IOS, waits for the radar to transfer data (the IOS program turns off the IOS at the end of the transfer), turns on the APS which in turn starts the APU, and waits for an APU done flag to be set. This operation divides each data element by 64 and sums them for 64 pulses. This complex voltage averaging process takes place with the radar and reflector stationary. The reflector signal is large when compared to the signals in the remaining 15 range cells. The phase and amplitude of the stationary target return signal are averaged for 64 pulses. The receiver channels are to be balanced in gain and phase to channel 1. This average phase and amplitude data is used as the basis for receiver channel normalization.

Next, the CSPU loads the APU with a vector-magnitude program and the APS with the proper addressing program. The APS is turned on and the APU.

The CSPU waits for the APU done flag to be set, at which time the 16 32-bit vector magnitudes on Memory Bus-2 from memory location 2200 to 223F (hex). The 16 vector magnitudes are calculated from the average complex voltages collected over the range cells of channel 1. The following MAP task determines the range cell with the largest voltage magnitude, and declares this range cell to contain the stationary initialization target.

The CSPU loads the APU with a program to determine which range bin of the radar data contains the greatest magnitude, and next loads the APS with the addressing program. The APS is started and the CSPU waits for the APU done flag to be set (it was necessary to introduce additional timing delay to allow time for the result to be placed in memory).

The CSPU loads the HIM with a program to transfer eight I and Q voltages to the CSP-30 host. The host uses this average voltage data to normalize the gain and phase of channels 2 through 8 to channel 1. A complex normalization factor is calculated in the host by using the eight-element receiver array scattering matrix and the average voltage array transferred from the MAP. The normalization factors are used to modify the AMTI and NEMRAD beam-forming coefficients resident in CSP-30 core memory.

The CSPU loads the HIM with a program to transfer the modified NEMRAD beam-forming coefficients, or antenna weights (eight complex factors), the modified AMTI antenna weights (eight complex factors), the NEMRAD filter coefficients (65 complex factors), and the AMTI filter coefficients (65 complex factors) from the host to the MAP. The CSPU waits for a host ready flag to be set to allow the host machine to compute these quantities and place them in the correct host memory area. When the CSPU senses that the host is ready, it starts the HIM processor, and the antenna weights are placed in identical memory areas on MAP Memory Bus-2 and Bus-3. The filter coefficients are placed on MAP Memory Bus-1. After the data has been transferred to the MAP, the CSPU loads the processors for real-time processing and then waits for another host ready signal before proceeding. This completes system initialization.

4.4.2 MAP REAL-TIME PROCESSING

Assuming that the MAP has performed system initialization and is waiting for the host, all that is necessary to begin real-time processing is for the host to set the host ready flag. Once real-time processing has begun, the host can halt the MAP with an I/O reset, otherwise the MAP runs indefinitely, [illegible] by the availability of radar data.

If the MAP has been halted by an I/O reset from the host, but not powered down, its memory is not disturbed and real-time processing can be [illegible] having to go through system initialization by sending the MAP [illegible] ring a number greater than "1."

The APU program multiplies eight complex receiver voltages (I and Q) [illegible] range bin by the NEMRAD antenna weights (I and Q) and sums the eight [illegible] products. The complex result of the summation is then [illegible] The [illegible] ment is that pulse one added to pulse two, [illegible] and so forth, [illegible] is required for the [illegible] NEMRAD [illegible].

Beam formation and Doppler filtering is repeated for AMTI processing, using identical radar data, identical Doppler filter coefficients, and AMTI antenna weights. The APU and APS run continuously for a block of 64 radar pulses (if they should finish calculating before more data is available, they wait in waiting loops).

$$B_{n,p} = \sum_{i=1}^{8} N_i \cdot A_{i,n,p}$$

$$C_n = \sum_{p=1}^{64} W_p \cdot B_{n,p}$$

N Beam forming coefficients (eight complex antenna weights)

A Complex receiver voltage from radar (eight complex voltages x 512 range bins per pulse)

B Synthesized beam pattern (16 complex voltages per pulse)

W Doppler filter coefficient (64 real or complex weights)

i i^{th} antenna element (eight elements receive array)

n N^{th} range bin (512 range bins)

p P^{th} radar pulse (64-pulse Coherent Processing Interval (CPI))

C Doppler filter output (one complex voltage per range bin per CPI)

After 64 radar pulses, the APU and APS are turned off, switched to the complex vector-magnitude program, and turned back on. Following each coherent processing interval, the magnitude of the 16 output filter voltages is calculated and transferred to the host for storage and display.

The radar data enters the MAP as 16-bit floating point numbers. All calculations are performed using 32 bits, and the final vector magnitudes are converted to 16-bit floating point format on MAP memory Bus-2. The HIM program transfers 16 NEARAD vector magnitudes, 16 AMTI vector magnitudes, a word containing zero, and an I/O status word (a total of 34 16-bit words) to the host computer after processing 64 radar data pulses. The CSPI codes do not test to see if the host machine takes the data, but proceeds to set up for the next block of data.

The I/O status word sent to the host contains information concerning the data transfer. The status word indicates data validity, and 3 types of data condition codes. There are three separate invalid data codes possible. They are:

a. Radar data became available during IOS read (data the IOS read was invalid because as the IOS read data from the radar data buffer, the radar data buffer was being written over with new data).

b. The IOS was running a few microseconds behind the radar (in this case one pulse of radar data was dropped).

c. Radar data becomes available while the MAP was processing and before the IOS started running (at least one pulse of radar data was dropped).

If no data status error or combination of errors occurred during the CPI, the CPI is said to be valid. For the purpose of definition, the CPI output combined with the status word is referred to as a batch.

In order for MAP processing to keep up with the radar data, it was necessary to employ a double buffering input scheme and to have a very efficient APU program. Some of the specific features which were necessary were:

a. The IOS is turned on and the radar data, when ready, is transferred to MAP Memory Bus-2.

b. The APU-APS is readied to process data on Bus-3.

c. As soon as the data has been transferred, the IOS turns itself off and the CSPU sets a flag to break the APU out of an idling loop to process that data.

d. The IOS is switched to Memory Bus-2 and enabled, waiting for the next pulse of data which will occur before the APU has finished processing Bus-3 data.

e. After the data has been transferred to Memory Bus-2 and the IOS turns off, the CSPU sets a flag to switch the APU to process Bus-2 data. If the APU has not finished Bus-3 data, it continues to process Bus-3 data until it does finish, at which time it immediately begins to process Bus-2 data. If the APU has finished Bus-3 data before Bus-2 data is ready, it sets in an idling loop waiting for the flag to switch it to Bus-2 data. The IOS is readied after setting the APU Bus-2 flag to transfer radar data to Bus-3. The CSPU chooses an APU flag to ensure that the APU has finished with the data in a particular memory bus before allowing the IOS to overwrite that data with another pulse of radar data.

f. This routine continues until [illegible] the IOS status word is OR'd with [illegible] of the programming [illegible] the [illegible] the rest. "IOSTAT" is sent [illegible] to the host.

g. At the end of the analysis, the APU and APS are stopped. The CSPU sets a flag to calculate vector magnitudes, turns on the APS and APU, then waits for the APU to perform the calculations. As soon as the APU is done, the CSPU enables the IOS to transfer radar data to Memory Bus-3 and turns on the HDX processor to transfer results to the host machine. It then clears some output memory summing locations and turns on the APS and the APU (which is awaiting

flag was cleared by the APU before turning off) to process another 65 pulses of radar data.

5.4.3 MAP SOFTWARE TEST MODE

If the host sends the MAP a mode word less than zero, the CSPU executes a test program that does everything the real-time program does *except for the radar*-to-MAP data transfers. The MAP Bus-2 and Bus-3 memory locations used for radar data are filled instead with simulated test data from the host machine. The MAP performs all calculations on this test data. The MAP is now synchronized by the data coming from the host machine and will run at a much slower rate.

The host machine is tasked with simulating the radar data matrix and transferring the test data to the MAP for beam formation and filter processing. In the Software Test Operating Mode, the MAP looks to the host for radar data, independent of the operational status of the radar. The simulated test data is generated based on simple target and clutter models. The host calculates a new test matrix on a *simulated pulse-to-pulse* basis. The host first calculates a test matrix, then transfers the simulated data into the MAP. As the MAP is processing simulated test data, the host also processes the simulated test data in a fashion identical to the MAP. When the host has completed processing of the test data, the MAP transfers processed results back to the host. The host then compares both sets of results and reports any significant errors to the operator. The next sequential simulated data pulse is calculated by the host and transferred to the MAP, and the test process repeats until halted by the operator.

The Software Test Mode of Operation allows a check of the digital processing software and hardware independent of the operational status of the radar.

5.5 MAP-300 Double Buffered Input

In a rigorous real-time radar operation, the time required to transfer the radar data plus the time required to process the data must be less than one interpulse period. This constraint may be loosened somewhat by implementing a double buffer input scheme.

Radar data is double buffered at the input of the MAP-300. Double buffering allows additional time for processing during the radar interpulse period. As will be shown, double buffering allows the processing time to extend through the data transfer interval and extend beyond one interpulse period. Real-time software requires a few microseconds more than one interpulse period to complete the processing of one data pulse; therefore, this additional processing time is essential.

Radar data is loaded into two separate buffers located on two data busses, specifically 2 and 3. Odd-numbered pulses are loaded into Bus-2, and even-numbered pulses are loaded into Bus-3. Data can be loaded into the

Bus-2 as data from memory Bus-3 is actively processed; therefore, double buffering is that data transfers and data processing proceed simultaneously. The data transfer interval appears transparent to the MAP architecture; however, this double buffering scheme does have serious limitations if the processing extends beyond one interpulse period. Data is accumulated, and eventually data will be written to memory. The data rate is determined by the number of processing elements (PE's) and the speed of the PE's. With the current design, the MAP can process 256 range cells in 51.2 microseconds (see Figure 3). With the current design, the MAP can process 256 range cells in 51.2 microseconds (see Figure 3). With the current design, the MAP can process 256 range cells in 51.2 microseconds (see Figure 3).

Figure 4. Double Buffered Input Timing

Double buffering also introduces several side effects. The processing of radar signals does not begin until the first interpulse period. The processing scheme must be pipelined to keep the data input rate balanced. Double buffering

input scheme provides the additional time necessary to complete inter-pulse processing for 65 pulses, while not dropping pulses due to APU execution speed limitations.

To quantitatively determine the additional available processing time due to double buffering the input data, refer to Figure 34. The time available for real-time processing (p) without double buffering equals the *interpulse period* (IPP) minus the time required to *transfer one pulse of radar data* (T), or

$$p \leq IPP - T \quad . \tag{5}$$

The additional processing time per pulse due to the double buffering input scheme may be found by the use of Figure 34. From the double buffered input timing diagram in Figure 34

$$2IPP = T + W + P + B \quad .$$

Also note

$$W = (n-1)L$$

$$P = IPP + L$$

To insure that MAP memory is not destroyed, constrain $B > 0$.

$$IPP - T - (n-1)L - L > 0 \quad .$$

Solving for the lag time (L) beyond one interpulse period (IPP), the processing can extend:

$$L < \frac{IPP - T}{n} \quad .$$

Letting n equal the number of pulses contained within one CPI yields

$$L < \frac{IPP - T}{CPI} \quad . \tag{6}$$

Therefore, the time allowed for processing with double buffering is

$$P < IPP + \frac{IPP - T}{CPI} \quad . \tag{7}$$

Subtracting the available processing time without double buffering from the processing time available with double buffering yields (Eq. (7) minus Eq. (5)) Eq. (6).

Let

Δt = Additional process time due to double buffering

$$\Delta t = P - p = T + \frac{IPP - T}{CPI}$$

$$\Delta t = T + \frac{p}{CPI} \quad . \tag{8}$$

The processing time gained by double buffering made real-time possible using the MAP-300. Double buffering allowed the processing time to be expanded by the data transfer interval plus a fraction of the processing time available without double buffering (p). The fraction of p decreases as the CPI increases. The limit of the processing improvement as the CPI approaches infinity is T.

For the NEMRAD(AATT) processing application:

CPI = 65

IPP = 546 μs

T = 154 μs .

Therefore

$$\Delta t = 154 + (546 - 154)\ 65 = 160\ \mu s \quad .$$

With 546 μs between pulses, up to 552 μs may be used for data processing with a 65-pulse CPI.

6. FIELD INSTALLATION AND TESTS

Section 6.1 describes the equipment used in experimental tests and the results obtained from the radar and test equipment calibration. Section 6.2 describes the radar installation and test. The test results, antenna scans, and receiver dynamic range are discussed in Section 6.3. The calibrated radar target used in the moving target experiments is discussed in Section 6.4. The straight target alignment technique to measure antenna beamwidth and sidelobe ranges is presented, and in conjunction with a description of the passive flat plate reflector, used as the radar target.

Section 6.2 reviews the four phases of field testing. Section 6.2.1 discusses the method used to measure two-way antenna patterns. Section 6.2.2 discusses the method used to measure the Doppler tuner characteristics. Section 6.2.3 and 6.2.4 review the NEXRAD's transmitted and received [illegible] respectively.

6.1 Experimental Set Up

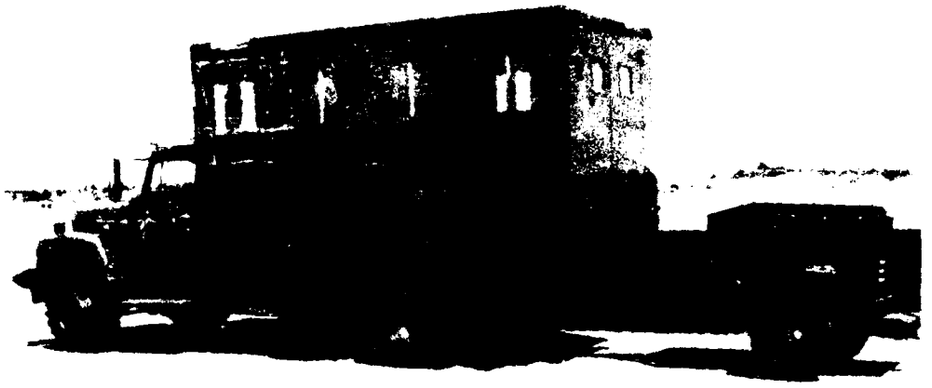

Figure 35. Radar Van Installation with Generator

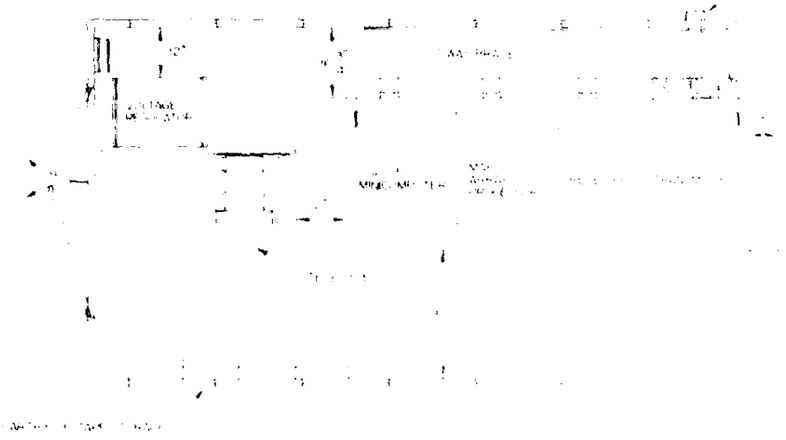

Figure 36. Radar Equipment Layout Diagram

AD-A099 079 ROME AIR DEVELOPMENT CENTER GRIFFISS AFB NY F/G 17/9
NULL FILTER MOBILE RADAR (NFMRAD): CONCEPT VERIFICATION,(U)
OCT 80 W BUCHANAN, H GODLEWSKI, F S HOLT
UNCLASSIFIED RADC-TR-80-306 NL

2 OF 2
AD A
099079

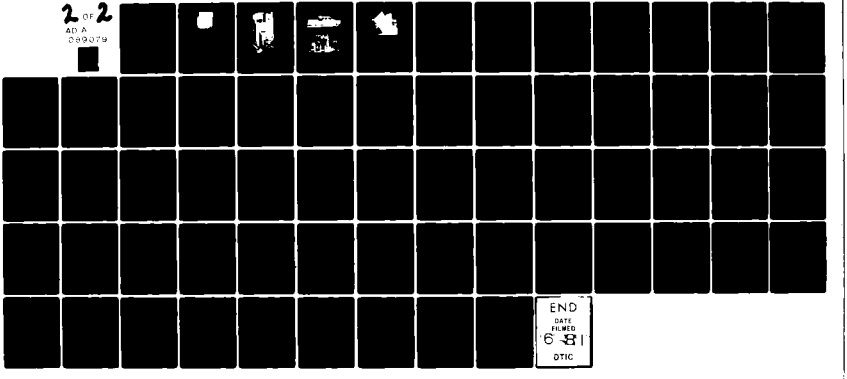

END
DATE FILMED
6-81
DTIC

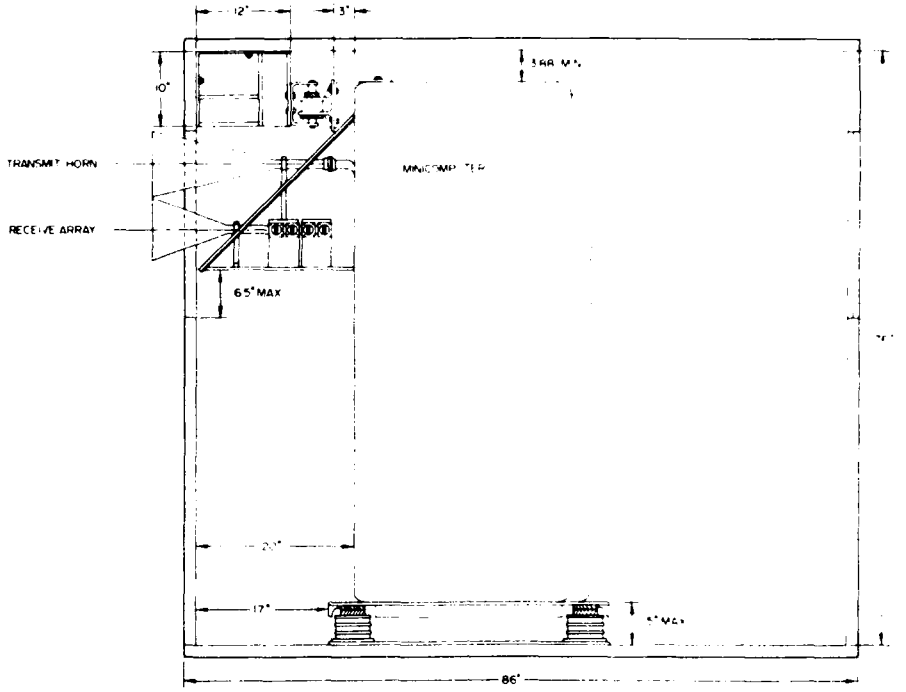

Figure 37. Radar Equipment Layout (End View of Van)

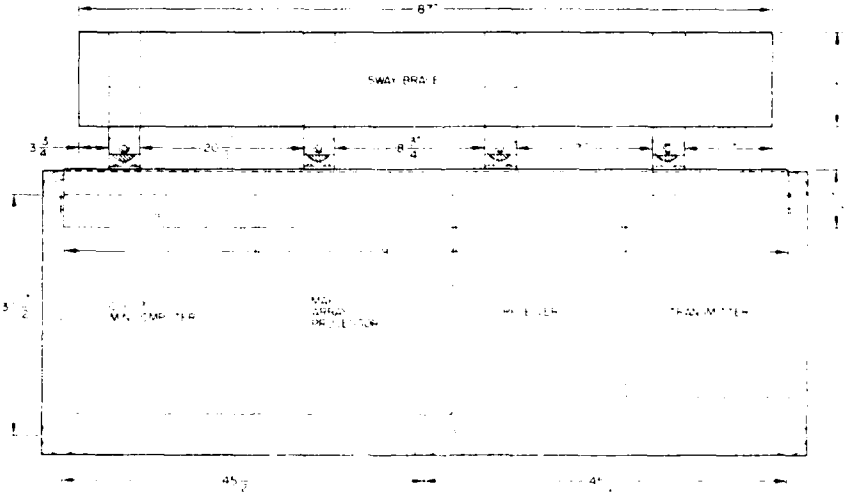

Figure 38. Floating Radar Platform with Shocks and Sway Braces (Top View)

Figure 39. Base Plate Shocks

6.1.3 ENHANCED RADAR TARGETS

6.1.3.1 Pickup/Corner Reflector Combination Target

The enhanced radar target utilized in moving target experiments described in Section 6.2.4 consisted of a large corner reflector mounted on the passenger side of a six-passenger pickup (see Figure 42). The corner reflector is depicted in Figure 43. A technician riding in the radar target vehicle insured that the target vehicle was positioned broadside to the radar van as the two vehicles traverse taxiways "Raytheon" and "Whiskey" shown in Figure 48. This was accomplished by the use of a boresight mounted adjacent to the large target corner reflector. A spotlight mounted above the radar van receive array served as an optical alignment aid for use with the boresight.

6.1.3.2 Flat Plate Reflector

The 12-in. (30.5-cm) square flat metal plate shown in Figure 44 was tripod mounted and used for system initialization. An optical alignment procedure insured broadside flat plate positioning. A light source held adjacent to the rifle scope seen in Figure 44 was used to insure broadside flat plate alignment relative to the receive array face. The experimental layout for system initialization is similar to that shown in Figure 45. Approximately 293 ft (89.3 m) from the radar van, a series of metal plates canted skyward were dispersed to break up the specular multipath component. Figure 45 shows the flat plate 450 ft (137 m) away from the radar

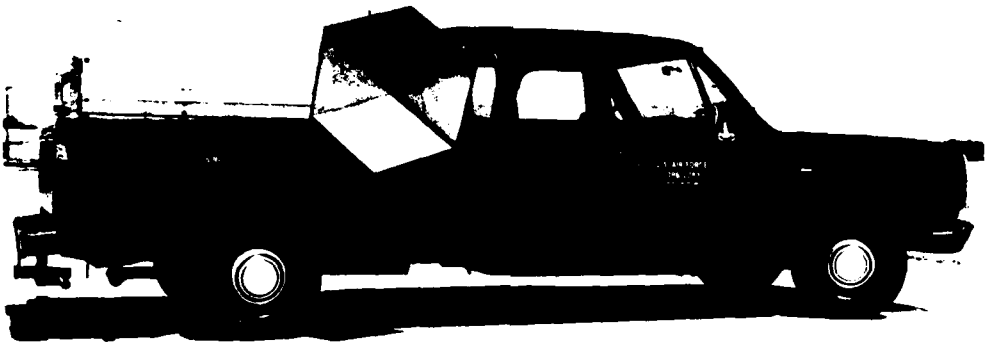

Figure 41. Remote Test Facility

Figure 42. Enhanced Radar Target

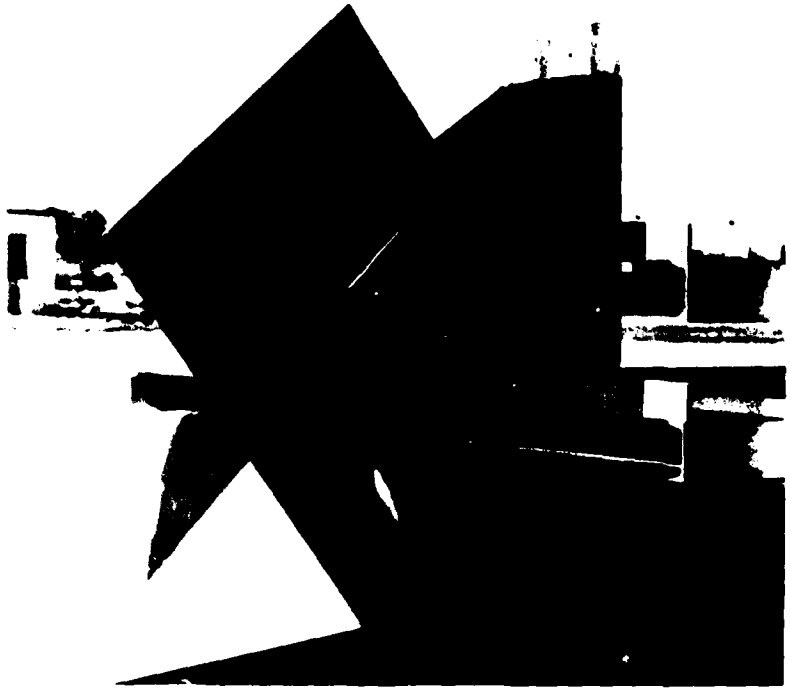

Figure 43. Corner Reflector

van used as a target for two-way antenna pattern measurements or for system initialization. Typically, the flat plate or corner reflector (Section 6. 1. 3. 1) would be used as a stationary target for antenna pattern measurements or system initialization. Due to the fact that the corner reflector provided a substantially larger radar cross section over a broader beamwidth, the corner reflector was used as a target most often.

6.2 Field Tests

NFMRAD {AMTI} field testing was divided into four separate phases. Phase 1 of field testing yielded two-way antenna patterns for the experimental radar system. Phase 2 consisted of experimentally verifying Doppler filter performance. A Doppler filter transfer characteristic was obtained with the radar position held constant measuring radar performance for converging and diverging targets traversing the radar main beam. In phase 3, target detection theshold voltages were determined. After target detection thresholds were established, phase 4 involved

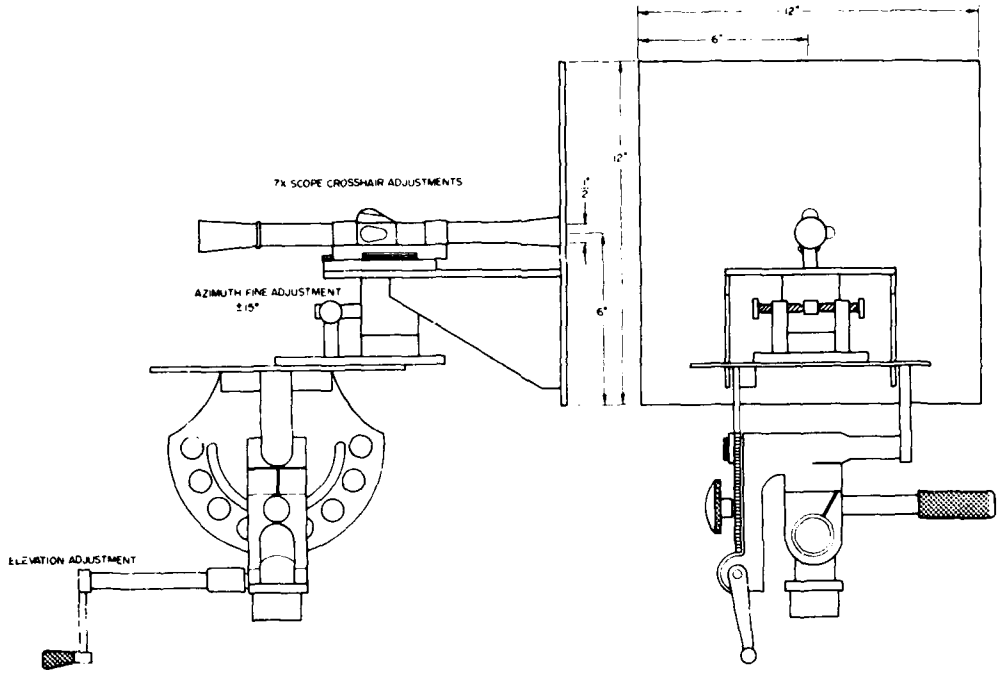

Figure 44. Flat Plate Reflector

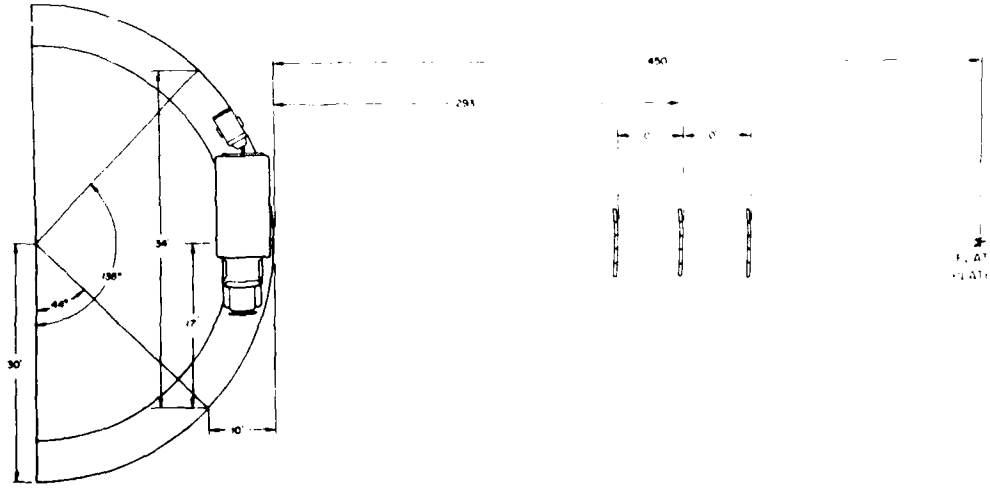

Figure 45. Field Site Used for Antenna Pattern Measurements (Top View)

moving target data collection in an effort to establish the probability of detection (P_d) for NEMRAD processing and conventional AMTI processing.

The discussion that follows will clarify the experimental details involved with generation of the data described above. Conditions in which the experimental antenna patterns, filter characteristics, target thresholds, and P_d curves were obtained will be discussed.

5.2.1 MEASUREMENT OF TWO-WAY ANTENNA PATTERNS

[illegible] the generation of the antenna patterns [illegible]

Several [illegible] measurement techniques were tried before a final scheme was adopted for antenna pattern generation. Initially, with the radar van stationary, a flat plate reflector was moved in azimuth at constant range. Pattern data was accumulated and stored on tape. Typically, the target was moved 2° in azimuth, realigned optically with respect to the radar van receive array, and pattern data was recorded on tape. The cycle would repeat from 0° to 180° bearing angle. An antenna pattern measurement consumed 4 hours; therefore, the measurement scheme was modified. The modified measurement scheme involved moving the receive array with respect to a stationary passive flat plate or corner reflector.

The modified scheme involved displacing the radar van in azimuth and holding the reflector stationary. Figures 45 and 46 depict the experimental layout utilized when transmit/receive patterns were measured. The van and receive array would advance 2° in azimuth and stop, pattern data was recorded on magnetic tape, the truck would then be positioned forward 2°, and the cycle repeated. This modified antenna pattern measurement scheme was not without drawbacks, however.

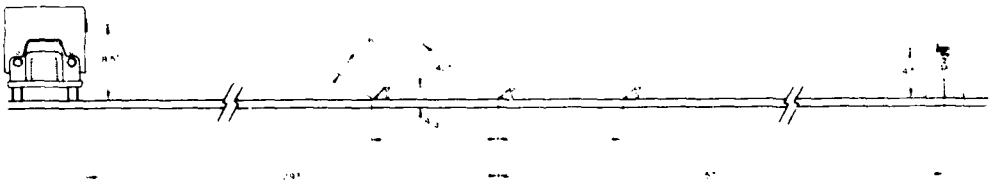

Figure 46. Field Site Used for Antenna Pattern Measurements (Side View)

There was concern the van would move outside the beamwidth of the stationary reflector. A second concern was multipath interference due to the low reflector and receiver array height. The terrain over which pattern data was collected was not flat, which lead to concern over vertical beam deflection as two-way patterns were measured. When advancing the van over unlevel concrete, the reflector

height would stay constant; however, as the truck advanced through arc, the relative height and tilt of the antenna array face with respect to the stationary reflector surface would vary slightly. The reflector illumination would vary due to multipath lobes formed in the beam; therefore, the pattern measured would typically be a composite of an antenna pattern generated primarily by radar azimuthal position but modulated by radar vertical displacement. The passive reflector was located at a range of approximately 450 ft (137 m). The van was driven in a tight turning arc. The radar van was displaced radially approximately 10 ft (3 m) from the reflector as data was collected over azimuth bearing angles of 44^{O} through 136^{O}. The receive array displacement parallel to the reflector was approximately ±17 ft (±5.2 m) referenced to broadside of the reflector. Every 8^{O} of arc, the flat plate was optically aligned and the multipath reflector wall repositioned. Flat plate height relative to the ground was 4.5 ft (1.37 m). Height of the receive/transmit antenna array was 8.5 ft (2.57 m). (When using the corner reflector shown in Figure 43 for making pattern measurements, it was not necessary to adjust reflector position as the radar van advaced through arc. The reflected power variation due to the van displacement was less than 1 dB.) The illuminated multipath patch of earth was masked as seen in Figure 45. The earth surface between the radar van and target was not prefectly flat, which presented a problem when trying to accurately ascertain the ground patch significantly contributing to multipath interference. A shotgun approach was adopted and a large ground patch was masked, using long metal reflectors canted skyward and X-band absorber material.

Single-element patterns were measured for each of the eight-receiver channels. Two-way patterns, measured as described above, were obtained by uniformly weighting each receive channel and summing over the eight-element array to form one composite pattern (hereafter referred to as the AMTI pattern). Finally, each receive channel was weighted to form the NFMRAD pattern. Theoretical and experimental patterns are presented in Sections 7.1 and 7.2. Patterns previously discussed in Section 6.2.1 are referenced in Chapter 7 as AMTI and NFMRAD.

Typically, antenna patterns were measured using common real-time operating software with modified antenna weights and Doppler filter coefficients. For example, to measure an antenna pattern for channel 1, the following software modifications are required. Channel 1 antenna weight is set to 1+j0; weights for channels 2 through 8 are set to 0+j0. Doppler filter coefficients are modified to form a dc pass filter, or all 65 filter coefficients are uniformly weighted to 1.65+j0. The resulting software zeros channels 2 through 8 receiver data and sums the weighted receiver data over all eight channels. After 65 pulses, an average channel 1 receiver output is generated for use as data in channel 1 single-element antenna pattern.

Similarly, to generate an AMTI antenna pattern, antenna weights in each channel are set to 1/8+j0. Doppler filter coefficients are uniformly weighted to form a dc pass filter just as in the single-element pattern.

One additional concern is the requirement for the eight-receiver channel I Q characteristics to appear uniform in phase and amplitude from channel to channel; all phase path lengths and gains must be uniform channel to channel. In practice, this constraint is not realized; therefore, the receiver channels are normalized in to insure channel uniformity before each series of measurements. The channel weight correction is a software normalization of channels 2 through 8 to channel 1. Before data is collected for processing, a channel normalization takes place within the software. Specifically, the gain and phase of all receiver channels are normalized to channel 1. A correction factor for each channel is calculated based on receiver response to an incident planewave parallel to the eight-element array aperture. The correction factor assures channel to channel uniformity by modifying each channel weight approximately, and assumes linear time invariant receiver operation. Before radar data is collected for processing, the channel normalization procedure is performed.

A flat plate or corner reflector is used as the signal source in the normalization procedure. A reflector is set normal to the receiver array and aligned optically. A multipath wall is constructed over an appropriate ground patch. Data is accumulated to determine gain and phase differences of each channel, and then the channels are normalized to channel 1. Antenna weights are modified by the appropriate correction factors, and the normalization procedure is complete.

To calculate an antenna patter, generally several (5 to 15) records of data were obtained per azimuth bearing angle. For the purpose of system term definition, one record consists of 60 data batches. One data batch is output following the processing of 65 received pulses over which the coherent processing interval extends. Every data batch contains processed data resulting from two radar processing techniques operating on a common radar data base. In the case of normal real-time radar operation, NFMRAD and AMTI processing would be implemented; consequently, the batch output would consist of NFMRAD and AMTI processed data. In addition to processed output data, the data batch also contains a batch status work indicator. This status word is an indication of data validity (that is, did the MAP processing stay ahead of the radar or was data lost over the 65-pulse coherent processing interval?). If a data pulse was dropped or written over, or if the MAP ran "barely behind" the radar during the coherent processing interval, the status word indicates the integrity of each processing interval. Every data batch is written to cartrifile tape in groups of 60. Sixty batches make up a record. In normal radar operation, one data batch consists of 16 NFMRAD range bin words (one voltage magnitude per range bin, no phase information) followed by 16 AMTI

range bin magnitudes. The final word in the data batch serial string is the status word. Table 12 depicts the contents of one tape record during normal real-time radar operation. Generally, several records were averaged per bearing angle or velocity to obtain an antenna pattern or Doppler filter characteristic. A record is constructed of 1980 words or 60 batches, and is defined for normal radar operation as shown in Table 12.

Table 12. Tape Record Obtained during normal real-time radar operation

NFMRAD voltage magnitude, range bin 1, batch 1
NFMRAD voltage magnitude, range bin 2, batch 1
.
.
.
NFMRAD voltage magnitude, range bin 16, batch 1
AMTI voltage magnitude, range bin 1, batch 1
AMTI voltage magnitude, range bin 2, batch 1
.
.
.
AMTI voltage magnitude, range bin 16, batch 1
STATUS word indicator 65 pulse interval, batch 1
NFMRAD voltage magnitude, range bin 1, batch 2
.
.
.
AMTI voltage magnitude, range bin 16, batch 2
STATUS word indicator 65 pulse interval, batch 2
NFMRAD voltage magnitude, range bin 1, batch 3
.
.
.
.
.
AMTI voltage magnitude, range bin 16, batch 60
STATUS word indicator 65 pulse interval, batch 60

6.2.2 MEASUREMENT OF DOPPLER FILTER CHARACTERISTICS

Measurements were made in an effort to verify digital Doppler filter performance. Theoretical filter characteristic is shown in Section 7.3, Figure 52. For a radar moving platform speed of 32 mph (14.3 m/s), the 3 dB bandpass velocities extend from 7.75 mph (3.47 m/s) diverging through 14 mph (6.25 m/s) diverging, with a peak centered around 11.25 mph (5.03 m/s). Bandreject velocities extend from approximately 4 mph (1.79 m/s) converging to 4 mph (1.79 m/s).

Experimental Doppler filter characteristics were determined by measuring steady-state radar response to moving target signal returns [illegible] velocities varying from 0 to approximately 32 mph (14.3 m/s) [illegible] approaching and diverging directions. Typically, several records of data were taken with the moving target centered in radar main beam. Figure 47 indicates the experimental layout used when measuring the radar Doppler filter characteristic.

Figure 47. Field Site Used for Measurement of Doppler Filter Characteristic (Top View)

One record extends over 60 coherent processing intervals (65 pulses per interval). An average of 1 pulse is lost when a batch output is transferred from the MAP-300 to CPS-30 minicomputer for tape storage. Approximately 3960 pulses are transmitted during one record at a prf of 1831; therefore, approximately 2.16 s expire during the accumulation of one record. The problem of multipath was not addressed when measuring Doppler filter data. The change in target height relative to the radar was also assumed to be negligible (due to the short distance traveled over one record and the apparent flatness of the surface traversed).

Each experimental P_d point in Figure 42 was averaged over many hours to obtain the characteristic shown. Each point on the experimental curve represents an average over many coherent processing intervals with the number of CPIs per data point a function of the target velocity. Figure 47 presents the approximate range and sampling interval over which data was accumulated for the filter characteristic. The stationary radar recorded the target behavior as the target traversed through the test section.

The target vehicle was a six-passenger [illegible] The [illegible] of the truck and reflector was [illegible] The [illegible] was [illegible] as a consequence of [illegible] target cross section [illegible] The [illegible] The [illegible]

[illegible] The [illegible] was [illegible] the MAP [illegible] The [illegible] The [illegible] P_d [illegible] P_{fa} [illegible] 7 [illegible] 4 [illegible] 1.7 [illegible] 8) averaging, and [illegible] 7.7 [illegible] 2.47 [illegible] 0.2 [illegible]

4.4.1 TARGET DETECTION THRESHOLD VOLTAGE DETERMINATION

The approach in Figure 46 includes the Rayleigh and Whiskey taxiways [illegible] being [illegible] P_{fa} data.

The purpose of [illegible] testing was the establishment of target detection thresholds as a function of false alarm rates for use in calculating P_d data. A large set of base-pass data for use in determining NEURAD CANTEC target thresholds, $V_T = f(P_{fa}) = V_T(P_{fa})$.

Initially, data was collected by [illegible] the radar van west to east across taxiway Whiskey at 32 mph (14.3 m/s) with no moving target vehicle present. This was to establish a background profile of the terrain in which the moving target would eventually be embedded. A substantial data base was collected with the vehicle moving at V_T = 32 mph (14.3 m/s) west to east, while no target was present on the Rayleigh taxiway.

Channel normalization was carried out in controlled repeatable fashion [illegible] the extent of the testing. Data collected was assumed to be spatially related [illegible] batch level from pass 1 down taxiway Whiskey through the final pass down Whiskey taxiway taken days later. Threshold data collection on taxiway Whiskey was [illegible]

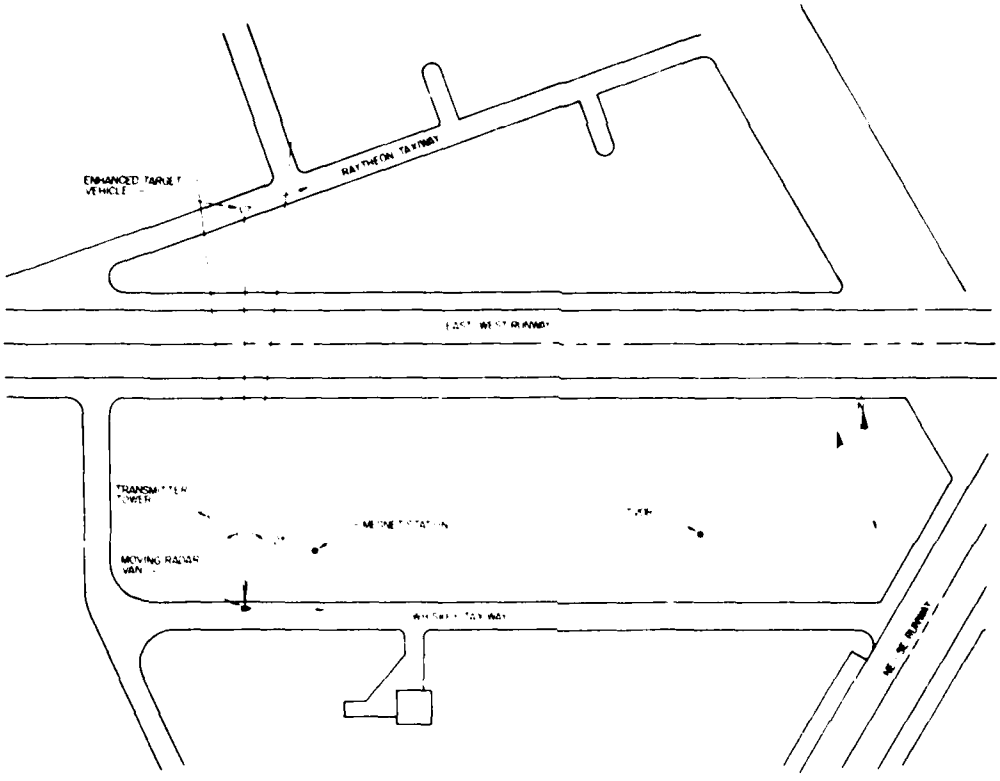

Figure 48. Field Site Used to Determine NFMRAD (AMTI) Threshold Voltages and NFMRAD (AMTI) P_d Curves (Top View)

only if the radar van had reached v_o before passing the transmitter tower shown in Figure 48. Typically, 10 records were accumulated per pass down taxiway Whiskey. The pass length extended for 1015 ft (309.4 m) and took approximately 22 s. Due to the roughness of the taxiway runway intersection, data collection was terminated before the intersection. The effort to obtain data starting position repeatability was driven by the need to have data from pass to pass related on a batch-to-batch, record-to-record basis (that is, batch 1, record 1, of pass 1 was measured overlooking the same terrain as batch 1, record 1 of pass 2). This constraint was imposed by the analysis method employed when calculating target thresholds and P_d curves.

Samples were gathered in an effort to obtain a data base with sufficient information to insure false alarm rates as low as 1 in 24 K. Approximately 2.4×10^5 samples were collected for the threshold data base.

Three separate analyses for determining target thresholds were implemented. Each scheme utilized a common data base for threshold calculation. The receiver detection threshold voltage is chosen to achieve the desired false alarm probability, P_{fa}. The false alarm probability of method 1 and method 2 may vary as the receiver gain and noise level drift; however, for analysis, the system was assumed time invariant. Method 3 utilizes a constant false alarm rate (CFAR) average; therefore, uniform drift in receiver gain and noise levels are of little consequence to the detection process (drift does affect system performance by causing channels to not be uniform).

Method 1 involved compiling, sorting, and tabulating range bin voltage data, and forming a histogram. Histograms were necessary for AMTI and NFMRAD data; therefore, two separate histograms were formed and separate thresholds were obtained. All range bins were lumped into one common data group, yielding a histogram containing 16·R·B·P samples where R = total number of records per pass, B = total number of batches per record, and P = total number of data collection passes. There are 960 NFMRAD {AMTI} voltage magnitudes contained within one record after lumping every NFMRAD {AMTI} range sample together. A single pass down taxiway Whiskey yields 9600 NFMRAD {AMTI} voltage samples, assuming 10 valid records. To achieve false alarm rates of 1 in 10^6, 1050 data collection passes are required. Clearly, so many Whiskey data runs is outside practical limits. A total of 105 passes are required to obtain sufficient data to insure false alarm rates of 1 in 10^5. This figure was determined to be beyond tolerable hardware limits; therefore, in the interest of all concerned, 25 passes were run to develop the voltage threshold data base. 240 K samples were collected, yielding a false alarm rate of 1 in 24 K. The data contained within this data base is filtered radar data; each batch represents one coherent processing interval. One might argue that since each voltage magnitude represents a weighted summation of 65 voltages, the false alarm rate should be 1 in 1.56×10^6 instead of 1 in 24 K.

Target thresholds are determined for NFMRAD {AMTI} by selecting voltages with magnitudes sufficiently large to realize the desired false alarm rate. Since no target is present, any voltage above the threshold voltage chosen should be considered a false alarm. Typically, NFMRAD {AMTI} voltage thresholds, $V_t^{NFMRAD}(P_{fa})$ $\{V_t^{AMTI}(P_{fa})\}$, are specified given a probability of false alarm P_{fa}; for example, a NFMRAD false alarm rate of 1 in 10^6 yields a threshold voltage written as $V_t^{NFMRAD}(10^{-6})$.

The second method implemented for threshold selection is a modified version of the first. Data is grouped on a range bin basis, forming 16 histograms for NFMRAD and 16 histograms for AMTI. Sixteen threshold voltages are chosen for

NFMRAD {AMTI} detection processing, resulting in one threshold voltage per range bin. The threshold selection scheme is similar to that described earlier. The significant difference in this scheme is the reduction in relative size of available threshold data base. The gain of method 2 is a spatially localized threshold level. Thresholds derived from method 2 are referenced using a k index, for example, range bin 2, NFMRAD probability of false alarm, $P_{fa} = 10^{-3}$, may be written as

$$V_{T(k)}^{NFMRAD}(P_{fa}) \quad V_{T(2)}^{NFMRAD}(10^{-3}) .$$

Method 3 employs a form of CFAR average. For a given NFMRAD {AMTI} data batch, 16 samples are averaged and multiplied by a constant α^{NFMRAD} $\{\alpha^{AMTI}\}$, resulting in a batch dependent threshold

$$V_{T}^{NFMRAD}(x, p) \{V_{T}^{AMTI}(x, p)\} .$$

Separate NFMRAD {AMTI} α values are required. Following CFAR averaging, detection processing is performed. If the threshold value, $V_{T}^{NFMRAD}(x, p)$ $\{V_{T}^{AMTI}(x, p)\}$, is less than any range bit voltage magnitude, $V_{RB(k)}^{NFMRAD(p)}(x)$ $\{V_{RB(k)}^{AMTI}(x)\}$, a false alarm is counted in the corresponding k^{th} range bin. This procedure is repeated every R·B·P batches. The number of false alarms is calculated following the conclusion of R·B·P batches. If the number of false alarms is larger than the number of false alarms specified, α^{NFMRAD} and α^{AMTI} are incremented, and the averaging continues until an α is established that produces the desired false alarm rate (given the constraint of data base size limitation). The calculated α values are used to determine the probability of detection when operating on the moving target data base. The CFAR averaging and threshold decisions are performed utilizing data that contains both background terrain and target data. After calculation α for a given P_{fa}, a P_d curve is calculated utilizing a separate data base containing the enchanced moving target.

6.2.4 NFMRAD {AMTI} P_d DETERMINATION

The map of Figure 48 indicates taxiway Whiskey utilized in Section 6.2.3, Target Detection Threshold Voltage Determination, is also used in Section 6.2.4. Data collected for determining detection probability was gathered by using two moving vehicles. In addition to the radar van traversing taxiway Whiskey, an electromagnetically enhanced target vehicle travels Raytheon taxiway in the direction shown. Radar moving platform velocity, V_o, equals 32 mph (14.3 m/s), as in Section 6.2.3 testing; however, Section 6.2.4 differs from Section 6.2.3 in that an

enhanced target vehicle travels broadside to the moving radar platform at v_t of 34.6 mph (15.5 m/s) (see Figure 48 for velocity directions). Raytheon taxiway 19° diverging angle is such that target radial velocity (v_r) is approximately 11.25 mph (5.03 m/s), the center frequency of Doppler filter passband.

Data collection begins after the radar van passes taxiway Whiskey transmitter tower if the moving platform velocity (v_o) and target radial velocity (v_r) are achieved before passing transmitter tower and the target vehicle possition is broadside to eight-element receive array mounted on moving platform. The target position was aligned optically with respect to the moving platform eight-element receive array.

Typically, v_o was achieved before reaching the transmitter tower. Shortly thereafter, the moving target position was aligned followed by stabilization of v_r. If v_r was realized before passing the transmitter tower, data collection was initiated and continued until moving platform approached runway 23 of Figure 48. Radio communications were established between the moving radar platform and target vehicle to insure experimental coordination. An optical bore sight alignment technique was implemented in the target vehicle to insure proper broadside target positioning. A bore sight mounted in the target vehicle was used for broadside target alignment in conjunction with a narrow-beam light source mounted on the moving radar platform. An observer riding adjacent to the large corner reflector mounted on the target vehicle monitored broadside target position. Verbal feedback from passenger position monitor to target vehicle driver was utilized in conjunction with radio communications to the moving platform. In summary, verbal and optical feedback coupled with nighttime testing made for a somewhat oscillatory (overshoot/undershoot) target position and velocity control. These experimental errors were due to accuracy limitations of vehicle speedometer readings, coupled with optical and verbal velocity and position control. However, velocity variations of v_r (v_r deviations related to fluctuations in v_t, v_o, and bearing angle θ) fall within the 3-dB Doppler passband characteristic of Figure 52. The theoretical NFMRAD and AMTI patterns of Figures 51 and 50 indicate NFMRAD performance is more sensitive to target position fluctuation at broadside than is AMTI, due to the forward canter of the NFMRAD main beam.

Real-time software used in Section 6.2.4 measurements was identical to software used in Section 6.2.3; however, the significant difference is the presence of an enhanced moving target traversing Raytheon taxiway broadside to radar moving platform.

Data accumulated pass to pass is again considered to be related batch to batch, record to record (as in Section 6.2.3). Approximately 25 passes were made down taxiway Whiskey, collecting data in Section 6.2.4 testing. Analysis of moving target data base toward the calculation of P_d values for NFMRAD and AMTI was implemented as described in the following discussion.

Section 6.2.4 data collected traversing taxiway Whiskey was compiled by grouping data batches as a function of taxiway Whiskey position in x, as shown in Figure 49. For purposes of this data analysis discussion, let

P ≡ data collection passes = 25

B ≡ data batches per tape record = 60

R ≡ records accumulated per data collection pass = 10

K ≡ range bins involved in detection processing

SF ≡ distance scale factor

p ≡ integer data collection pass index where $1 \leq p \leq P$

b ≡ integer batch index where $1 \leq b \leq B$

r ≡ integer record index where $1 \leq r \leq R$

$\bar{x}$ ≡ normalized Whiskey taxiway position where $0 \leq \bar{x} \leq 1$

x ≡ Whiskey taxiway position relative to transmit tower where $0 \leq x \leq SF$

k ≡ integer range bin index

STATWD ≡ data batch status word

$V_{t(k)}^{NFMRAD}(P_{fa})$ $\{V_{t(k)}^{AMTI}(P_{fa})\}$ ≡ NFMRAD {AMTI} threshold voltage as function of P_{fa}

P_{fa} ≡ probability of false alarm

$V_{RB(k)}^{NFMRAD(p)}(x)$ $\{V_{RB(k)}^{AMTI(p)}(x)\}$ ≡ NFMRAD {AMTI} range bin voltage magnitude where $1 \leq k \leq K$ and $1 \leq p \leq P$.

$P_d^{NFMRAD}(x, P_{fa})$ $\{P_d^{AMTI}(x, P_{fa})\}$ ≡ NFMRAD {AMTI} probability of detection as function of Whiskey taxiway position and probability of false alarm

$\alpha^{NFMRAD}\{\alpha^{AMTI}\}$ ≡ CFAR real coefficients

$V_\alpha^{NFMRAD}(x, p)$ $\{V_\alpha^{AMTI}(x, p)\}$ ≡ CFAR batch dependent voltage threshold

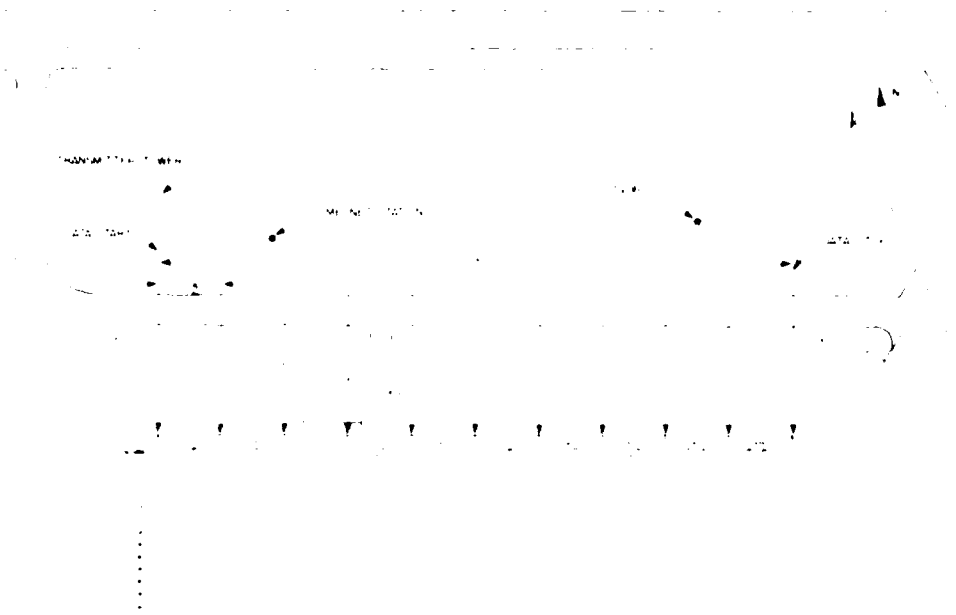

Figure 43. Taxel-to-Whisker Divided into Tape Records. Ten tape records are [illegible]

We now take $\bar{x}$ to be the vector $\bar{x}$ as a function of t and τ. The variable $\bar{x}$ may be expressed in terms of the vector $\bar{x}$ as follows:

$$\bar{x}(t, \tau) = \frac{\bar{x}(t)}{\|\bar{x}(t)\|}$$

where t and τ are chosen so that $1 \leq t \leq 10$ and $1 \leq \tau \leq 10$.

$$x = s\bar{x}$$

where x is a scalar. Given t and τ, establish $\bar{x}$. For example, let t and τ fixes moving platform position relative to Taxel-to-Whisker 1 which is fixed to the right of transmitter tower. In other words

$$\bar{x} = \bar{x}(1, 1) = \frac{1}{300}$$

or at $\bar{x}(1, 1)$, 1 500 total taxiway pass has been completed. At b B and r R,

$$\bar{x} \quad \bar{x}(b, r) \quad \bar{x}(B, R) \quad \frac{(60)\ (10)}{(60)\ (10)} \quad 1$$

or a $\bar{x}(B, R)$ total taxiway pass has been completed. For any Whiskey position, $\bar{x}(b, r)$, P data batches are used to calculate $P_d(\bar{x})$. The p^{th} batch specified at $\bar{x}$ contains 16 NFMRAD voltage magnitudes, $V_{RB(k)}^{NFMRAD}$, 16 AMTI voltage magnitudes, $V_{RB(k)}^{AMTI}$, and 1 batch status word, STATWD. The status word is used only to insure data integrity; STATWD is not used in detection processing. If STATWD indicates batch data is invalid, batch data is not processed. If the p^{th} data batch at x(b, r) is valid, detection processing is performed over K NFMRAD range bins and K AMTI range bins. Three separate detection procedures are implemented in an effort to determine $P_d(x)$ sensitivity to the detection procedure utilized. Target threshold voltages, $V_t^{NFMRAD}(P_{fa})$ and $V_t^{AMTI}(P_{fa})$, established as a function of P_{fa} in Section 6.2.3 testing, are used in detection processing implemented in Section 6.2.4. Three separate detection methods were implemented as follows.

Method 1, described in Section 6.2.3 yields $V_t^{NFMRAD}(P_{fa})$ and $V_t^{AMTI}(P_{fa})$. Given probability of false alarm, P_{fa}, one NFMRAD threshold and one AMTI threshold voltage are produced following method 1 detection threshold analysis.

Method 1 detection processing utilized $V_t^{NFMRAD}(P_{fa})$ $\{V_t^{AMTI}(P_{fa})\}$ to ultimately calculate P_d^{NFMRAD} $\{P_d^{AMTI}\}$ as a function of moving platform taxiway Whiskey position x(b, r). NFMRAD {ATMI} probability of detection P_d^{NFMRAD} $\{P_d^{AMTI}\}$ for a specified probability of false alarm P_{fa} at taxiway position x(b, r) may be written as

$$P_d^{NFMRAD}(x(b, r)P_{fa}^{NFMRAD}) \quad P_d^{NFMRAD}(x, P_{fa}^{NFMRAD}) \quad \{P_d^{AMTI}(x(b, r), P_{fa}^{AMTI}) \quad P_d^{AMTI}(x, P_{fa}^{AMTI})\} \ .$$

A typical analysis to evaluate $P_d^{NFMRAD}(x, P_{fa})$ at x' x(b', r') and P_{fa} P_{fa}' follows:

Given:

b', r' (establishes taxiway position on Whiskey as x')

P_{fa}' (establishes probability of false alarm)

x(b', r') is equivalent to P data batches collected a x'.

If $V_{RB(k)}^{NFMRAD(p)}(x') > V_t^{NFMRAD}(P_{fa}')$ for any k such that $1 \leq k < K$ and $p = 1$, then a single target hit is counted.

If $V_{RB(k)}^{NFMRAD(p)}(x') < V_t^{NFMRAD}(P_{fa}')$ for all k such that $1 < k < K$ and $p = 1$, then no hit is counted.

Pass counter p is incremented and the detection procedure is repeated for $p = 2, 3, 4, \ldots P-1, P$. Following detection processing conclusion at $x(b', x')$, the total number of hits over P passes are totaled. A target is assumed present at x' P hits. Total hit count at x' is divided by P passes to obtain probability of detection $P_d^{NFMRAD}(x', P_{fa}')$. To calculate $P_d^{NFMRAD}(x, P_{fa}')$ from $\bar{x} = x$ to $x = \bar{x} - 1$, P_{fa}' held constant and x is varied over the entire Wiriskey taxiway $x(0 < x < \bar{x})$. A parallel procedure is utilized to calculate $P_d^{AMTI}(x, P_{fa}')$.

Method 2, described in Section 6.2.3, yields $V_{t(k)}^{NFMRAD}(P_{fa}')$ $\{V_{t(k)}^{AMTI}(P_{fa}')\}$ where $1 < k < K$. Given P_{fa}', K threshold voltages are produced for NFMRAD {AMTI}. Method 2 detection processing utilizes $V_{t(k)}^{NFMRAD}(P_{fa}')$ $\{V_{t(k)}^{AMTI}(P_{fa}')\}$ and $V_{RB(k)}^{NFMRAD(p)}(x)$ $\{V_{RB(k)}^{AMTI(p)}(x)\}$ to calculate $P_{d(k)}^{NFMRAD}(x, P_{fa}')$ $\{P_{d(k)}^{AMTI}(x, P_{fa}')\}$ where $1 < k < K$; generally $K = 16$. In summary, Section 6.2.3 method 2 analysis yields K NFMRAD thresholds and K AMTI thresholds. The results from method 2 analysis yield K NFMRAD {AMTI} P_d curves for a single P_{fa} value; generally, one pair of P_d curves per range bin. Method 2 processing yields K P_d curve pairs, or one NFMRAD AMTI curve pair per range cell for specified P_{fa}'.

Method 1 detection processing analysis yields one composite NFMRAD AMTI curve pair per P_{fa}'.

Method 2 analysis to evaluate $P_{d(k)}^{NFMRAD}(x, P_{fa}')$ for range cell 1 follows. Determine NFMRAD probability of detection at $x = x'$, $P_{fa} = P_{fa}'$, $k = 1$. Obtain $V_{t(1)}^{NFMRAD}(P_{fa}')$ from method 2 voltage threshold detection analysis.

If $V_{RB(1)}^{NFMRAD(p)}(x') > V_{t(1)}^{NFMRAD}(P_{fa}')$ where $p = 1$, then a target is declared for range bin 1, on pass 1.

If $V_{RB(1)}^{NFMRAD(p)}(x') < V_{t(1)}^{NFMRAD}(P_{fa}')$ where $p = 1$, then no target is recorded for pass 1, range bin 1, at x', P_{fa}'. Pass counter p is incremented and the detection procedure stated above is repeated for $p = 2, 3, 4, \ldots, P-1, P$. Following P detection calculation decisions, the total number of range bin 1 target hits at x', P_{fa}' is summed. If target was known to be present in range bin 1, it is assumed present for P taxiway passes. The total number of target hits divided by P yields

$P_{d(1)}^{NFMRAD}(x', P_{fa}')$. If target was known to be outside range cell 1, all target hits are counted as false alarms, and a P_{fa} curve is calculated.

The total number of samples taken for range cell 1 equals 65 R B P/16. Let total samples taken for k^{th} range cell equal $sample_{tot}$. To calculate false alarm probability, total false alarm count is divided by $sample_{tot}$. The procedure outlined above yields P_d or P_{fa} calculated at x' only. To generate entire curve over x, x must vary over entire taxiway, or from 0 through SF.

Method 3 described in Section 6.2.4 yields α^{NFMRAD} and α^{AMTI} given P_{fa}. These α values are used in implementing a form of CFAR averaging. Typically, α^{NFMRAD} $\{\alpha^{AMTI}\}$ is multiplied by the average of $V_{RB(k)}^{NFMRAD(p)}(x)$ $\{V_{RB(k)}^{AMTI(p)}(x)\}$ where $1 \leq k \leq K$ over P passes. The resultant product is treated as a batch-dependent threshold voltage. To calculate NFMRAD batch-dependent threshold $V_{t\alpha}^{NFMRAD(p)}(b, P_{fa})$:

$$V_{t\alpha}^{NFMRAD(p)}(b, P_{fa}) \quad \frac{\alpha^{NFMRAD}}{K} \sum_{k=1}^{K} V_{RB(k)}^{NFMRAD(p)}(x)$$

where $p = 1, 2, 3, \ldots P$. The batch-dependent threshold was treated in method 3 detection analysis as in method 1. A single composite curve pair is generated given P_{fa}, and 16 curve pairs are generated in a fashion similar to method 2.

7. EXPERIMENTAL RESULTS AND CONCLUSIONS

7.1 Two-Way Antenna Patterns

7.1.1 UNIFORMLY WEIGHTED ANTENNA PATTERN

The antenna pattern shown in Figure 50 was measured as described in Section 6.2.1. Figure 50 depicts the two-way experimental antenna pattern with crosshatches, and the theoretical pattern with a solid line. Experimental pattern data was collected over bearing angles ranging from 44° to 136°. Experimental error in azimuth resolution was estimated to be less than 2°. The experimental pattern shown is averaged over many tens of data batches, or each crosshatch represents an average of several data records. The theoretical nulls at 68° and 112° were contributed by the transmit pattern; however, the forward null at 68° and the aft null at 112° were not experimentally verified, as seen in Figure 50.

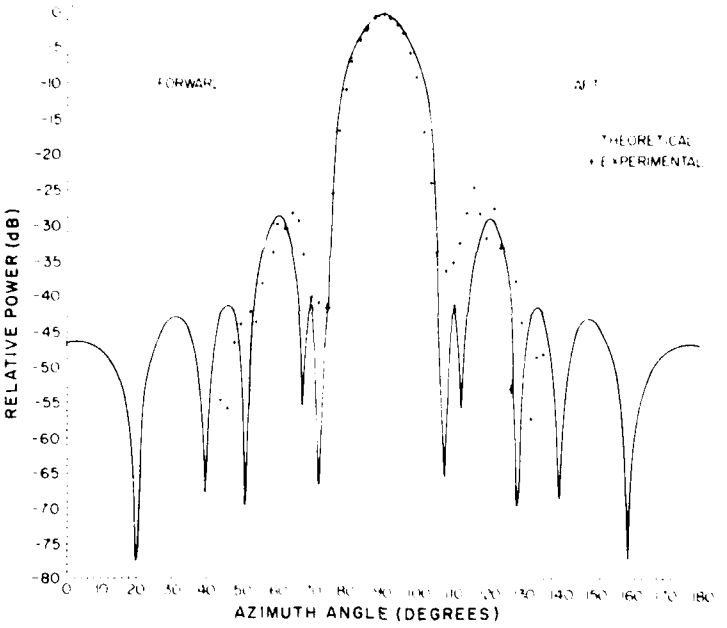

Figure 50. AMTI Two-Way Azimuth Pattern (Theoretical and Experimental)

7.1.2 NFMRAD ANTENNA PATTERN

The antenna pattern shown in Figure 51 was measured as described in Section 6.2.1. Figure 51, like Figure 50, depicts the experimental two-way antenna pattern with crosshatches, and the theoretical pattern with a solid line.

The experimental NFMRAD pattern shows the most serious problem encountered thus far during field testing. Results indicate the experimental NFMRAD (AMTI) radar is unable to synthesize a broad antenna pattern null. Theoretically, the NFMRAD null should extend from approximately 104° to 118°; however, this broad null has thus far not been obtained. Narrow -45 dB nulls have been measured; however, they generally are not repeatable. For the NFMRAD processing scheme to realize performance improvement over AMTI processing, the 14° antenna pattern null is essential. A solution to this problem is now being implemented.

The minicomputer software is being modified to include an adaptive beam-forming algorithm. Beam-forming coefficients will be dynamically updated and the null will be formed adaptively.

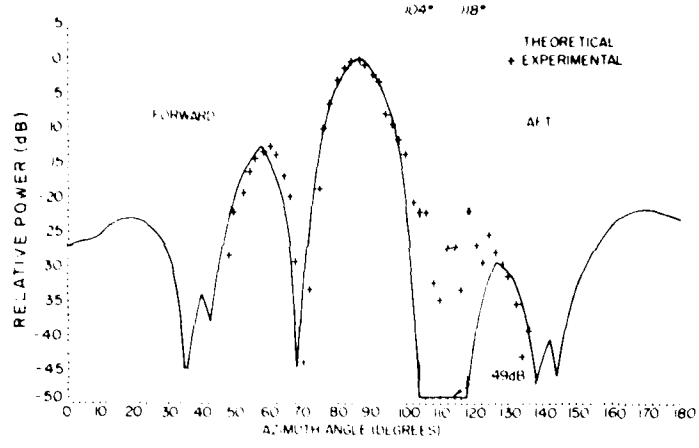

Figure 51. NFMRAD Two-Way Azimuth Pattern (Theoretical and Experimental)

7.2 Doppler Filter Characteristics

The Doppler filter characteristic, shown in Figure 52, was measured as described in Section 6.2.2. Experimental filter data was collected over a range of target velocities from 32 mph (14.3 m/s) converging to 32 mph (14.3 m/s) diverging. The experimental data outside the bandstop bandpass region of the filter characteristic is approximately 15 dB higher than the theoretical response.

7.3 Threshold Voltage Determination

Data described in Section 6.2.3 was obtained for determining appropriate target thresholds as a function of false alarm rate; however, our inability to realize a broad repeatable antenna null insured the collected data was inadequate to prove the NFMRAD concept.

7.4 Receiver I/O Characteristic

Figure 53 shows a typical receiver I/O characteristic. RF power varying from -96 dBm to -26 dBm was fed to each of the eight receiver channels. The receiver output voltage was measured, using the MAP and CSPI processors. This typical characteristic exhibits a linear receiver dynamic range of approximately 64 dB. The receiver theoretical dynamic range (assuming no noise) is 90 dB. As seen in Section 7.5, noise due to the RF front end may consume up to 6 bits or 30 dB of dynamic range. Generally, 24 dB of receiver dynamic range is consumed by the mean noise voltage.

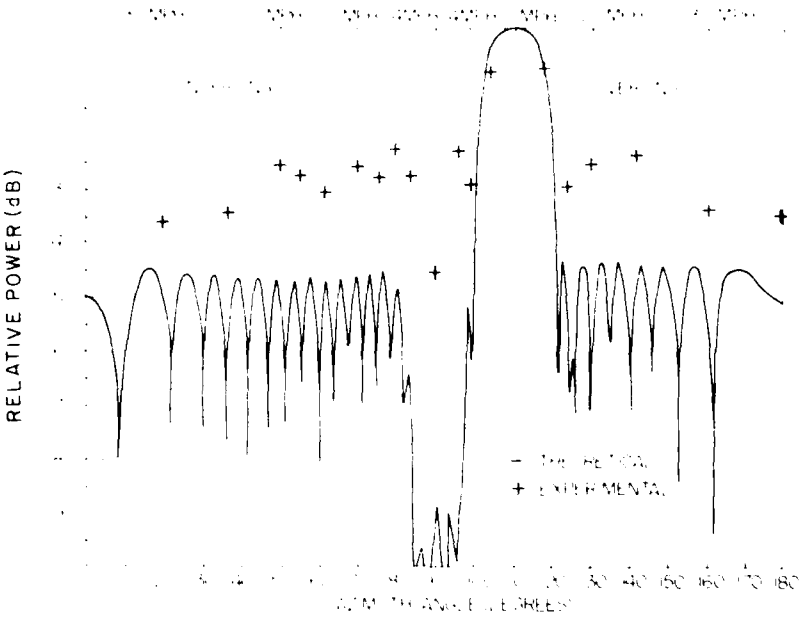

Figure 52. Doppler Filter Characteristic

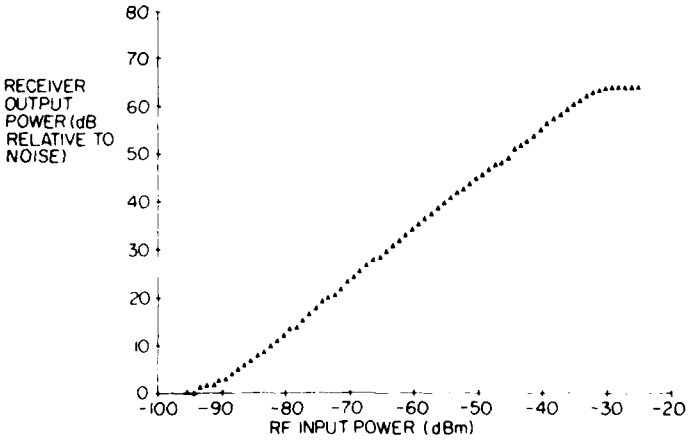

Figure 53. Receiver I/O Characteristic

7.5 Receiver Noise Histogram

Figure 54 is a typical histogram of receiver channel noise. The noise amplitude was calculated for 1000 complex independent voltage samples. One may approximate the number of bits consumed by receiver noise using Figure 54. For worst-case analysis, assume the noise voltage is equal the Q voltage component, and the I voltage component is zero. The mean noise voltage over all eight channels was calculated to be 80 mV. ADC input sensitivity of 10 mV/change of ADC output state; therefore, eight changes of state occur at the output of the ADC. Thus, the mean noise voltage consumes 4 bits of the ADC dynamic range (worst case). From Figure 54, a noise magnitude of 200 mV occurred 10 times out of 1000 samples or 1 percent of the total number of samples. Worst-case analysis of this case yields 20 changes of ADC output state or 5 ADC bits may be consumed by receiver noise (7 mantissa bits total given a constant base 2 exponent).

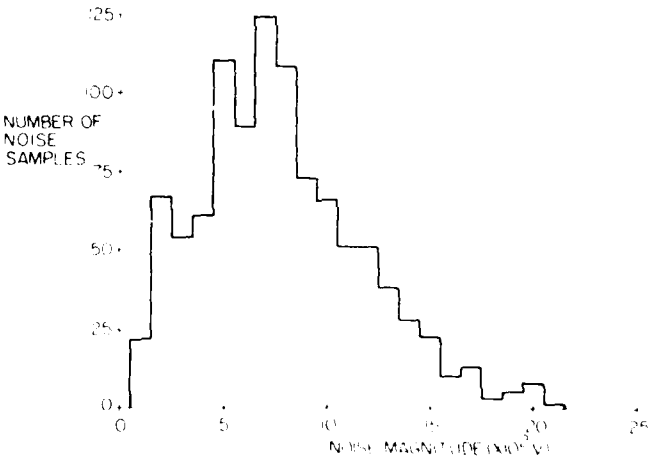

Figure 54. Receiver Noise Histogram

A noise histogram, generated using integer I and Q voltage components, will contain voids around 1.5 and 4.5 x 10^{-2} V. This apparent problem concerns the histogram generation algorithm and the quantized voltage data, not the statistical nature of the noise data. For an explanation, let n be the noise voltage magnitude or

$$n = \sqrt{I^2 + Q^2}$$

where I and Q are integers. Then the case above I, Q = 1, 2 and 4, Q = 0 does not exist for any integer I and Q combination. The discrete nature of the quantized voltage data and the histogram search and sort algorithm are the causes for the receiving noise distribution.

7.6 Preliminary Conclusions and Future Direction

Thus far, we have seen that it is extremely difficult to form broad ($\pm 4^{\circ}$) and deep (-40 dB) notches in our receive antenna pattern.

Our beam formation approach assumed an accurate knowledge of the receive array scattering matrix. One explanation of our experimental problem is that the broad antenna null may lie in the accuracy to which the scattering matrix is known. Figure 55 shows the sensitivity of null depth to small distributed errors in the scattering matrix. With relatively small errors in the scattering matrix, the null between 104° and 108° rapidly fills. The scattering matrix is suspected because it was measured in an anechoic chamber using the receive array as the transmit beam or to be flat. It seems reasonable to assume that the scattering matrix will be altered somewhat due to the interaction between the receive array elements and the skin of the van (the elements between the array and the van skin).

An assumption we have considered is that the channel noise characteristics of the scattering matrix and the calculated steering vector phase channel errors are factors. Scattering matrix errors therefore may partially explain both the experimental antenna pattern and Doppler filter discrepancies.

The channel normalization procedure seemed reasonable; however, it was not conclusively shown to be adequate. Typically, the correction factors were repeatable to within one or two decimal digits when compared over as long as 4 hours. Generally, after 4 hours of operation, dc drift would be sensed at the output of one or more of the receiver channels. The problem was compounded by having 16 I and Q components to check and calibrate. Following calibration, channel normalization would be run.

Efforts are now underway to develop software that will adaptively form the receive antenna pattern. The modified system will sample its environment and then adjust its own weights to optimize the SNR. This work should provide a means to adaptively form the broad antenna pattern null required for NEXRAD processing.

An effort to remeasure the scattering matrix of the receive array is under the radar van is also being pursued.

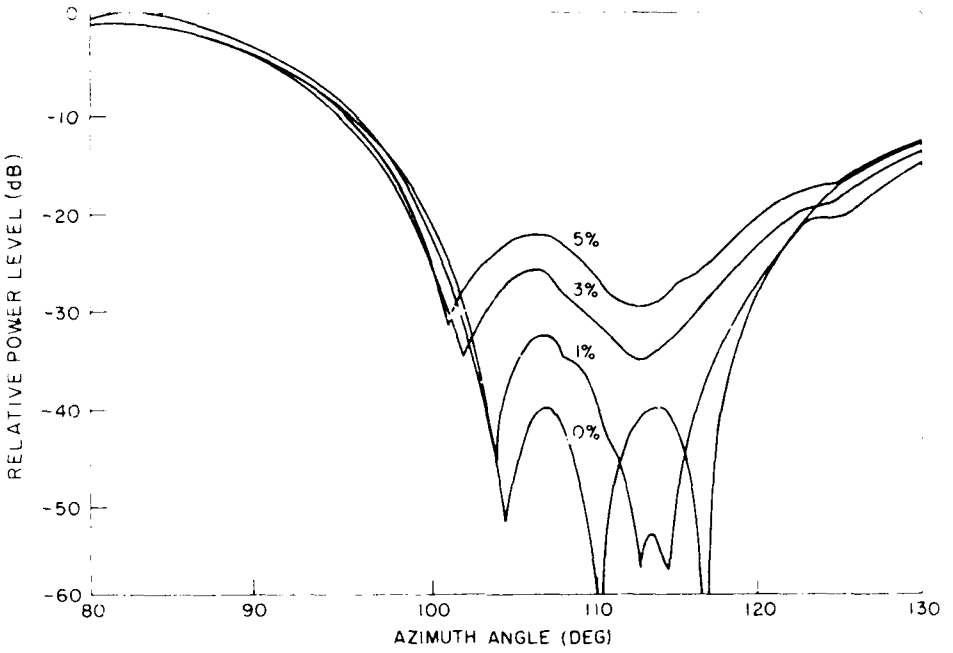

Figure 55. Effect of Uniformly Distributed Error in the Scattering Matrix on the Null Region of Receive Pattern. Errors indicated are maximum percent error

References

1. Goggins, W.B., Jr., Sletten, C.J., and Holt, F.S. (1974) New concepts in AMTI radar: Nulling effect of Doppler filter multielement horn array, Microwave J. 17(No. 1):29-33.

2. Brown, Dr. Gary S., and Curry, William J. (1979) An Analytical Study of Wave Propagation Through Foliage, RADC-TR-79-359.

3. Cherry, D.K., and Tseng, F.I. (1965) Gain optimization for arbitrary antenna arrays, IEEE Tr. AP AP-13(No. 6):973.

4. Drane, C.J., Jr., and McIlvenna, J.F. (1969) Gain Maximization and Controlled Null Placement Simultaneously Achieved in Aerial Array Patterns, AFCRL-69-0257, AD

5. Goggins, W.B., Jr., and Schindler, J.K. (1974) Processing for Maximum Signal-to-Clutter in AMTI Radars, pp. 15-21, AFCRL-TR-74-0577, AD

6. Collin and Zucker, eds. (1969) Antenna Theory, Part I, McGraw Hill, pp. 621-630.

Appendix A

Complex Recursive Infinite Impulse Response (IIR) Digital Filters

A1. FILTER SPECIFICATIONS AND NORMALIZED REAL LOW-PASS FILTER DESIGN

It is desired to design digital filters that have a single passband or a single stopband in the frequency interval $-\Pi f_p \leq \Omega \leq \Pi f_p$ where f_p is the pulse repetition frequency. Except for the special cases where the passbands or the stopbands are centered at dc, it will be necessary to use filters whose transfer functions are complex.

For any particular design, the following specifications are needed:

(1) Passband (or stopband) extend $\omega_1 \leq \omega \leq \omega_2$

(2) Upper bound on ripple in the passband

(3) Filter discrimination (ratio of maximum signal power passed to maximum signal power in the reject region)

(4) Rolloff or rate of transition from the pass regions to the reject regions of the filter

(5) Filter response time

(6) Sampling period ($T = 1/f_p$).

Two methods were used to develop desired IIR digital bandpass and bandstop filters. The first method proceeds as follows:

Let $0 < \omega_1 < \omega < \omega_2$ be the desired passband (or stopband). Using the design procedures described by Gold and Rader,[A1] frequencies ω'_{A1}, ω'_{A2}, ω'_{A0} and ω'_{AC} are defined by the relations

$$\omega'_{A1} \quad \tan\left\{\frac{\omega_1 T}{2}\right\}$$

$$\omega'_{A2} \quad \tan\left\{\frac{\omega_2 T}{2}\right\}$$

$$\omega'_{A0} \quad \left\{\frac{\omega_2 - \omega_1}{2}\right\}$$

$$\omega'_{AC} \quad \left\{\frac{\omega_1 + \omega_2}{2}\right\} .$$

Based on the specifications of ripple in the passband, discrimination, and rolloff rate, the nomographs described in Christian and Eisenmann[A2] determine suitable filter types (that is, Butterworth, Chebycheff, or Cauer), and for each type the associated voltage transfer loss function, H(S), $S = \Sigma + j\Omega$ that will meet the specifications in a normalized lowpass filter. A plot of a typical power transfer loss function $A(j\Omega) = 10 \log_{10}|H(j\Omega)|^2$ for a normalized lowpass filter is shown in Figure A1. The quantity A_{max} is the maximum attenuation in the passband and is a measure of the ripple in the passband. A_{min} is the minimum attenuation in the reject region, and hence the difference $A_{min} - A_{max}$ is a measure of the filter discrimination. The frequency Ω_s is related to the rolloff rate and, in particular, the quantity $(\Omega_s - 1)/2$ is the ratio of the width of the transition region at one edge of the passband to the full width ($-1 \leq \Omega \leq 1$) of the passband. The tables in Christian and Eisenmann[A2] specify the voltage transfer loss function A(S) by tabulating the zeros Ω_{o1}, Ω_{o2}, ... and poles $\Omega_{\infty 1}$, $\Omega_{\infty 2}$, ... of H(s) (see Figure A1). The voltage transfer function F(S) for the normalized lowpass filter is given by

$$F(S) = 1/H(S) .$$

Filters with a single passband or a single stopband can be generated from the same normalized lowpass filter by means of well known transformations described in the next section.

A1. Gold, B., and Rader (1969) Digital Processing of Signals, McGraw Hill, New York.

A2. Christian and Eisenmann (1966) Filter Design Tables and Graphs, John Wiley and Sons, New York.

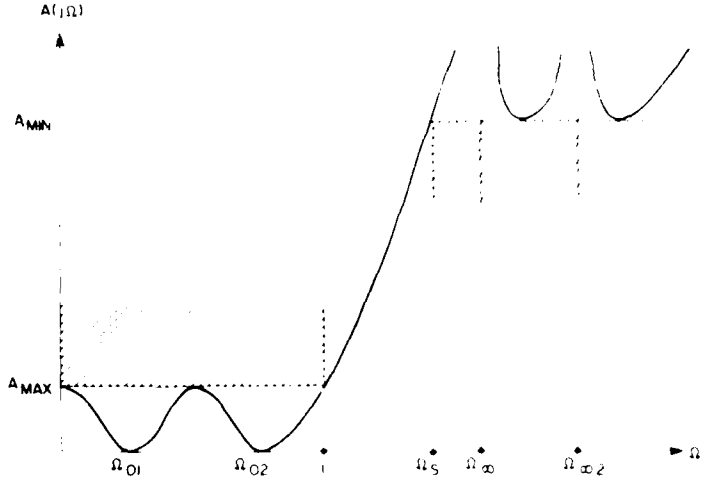

Figure A1. Power Transfer Loss Function for a Cauer C04a Type Filter

A2. TRANSFER FUNCTIONS FOR SINGLE PASSBAND COMPLEX FILTERS

The transformation

$$S = \frac{\omega'_{A1}\,\omega'_{A2} + (S')^2}{S'(\omega'_{A2} - \omega'_{A1})}, \quad S' = \sigma' + j\omega'$$

converts the normalized lowpass filter into a bandpass filter with voltage transfer function

$$F_{bp}(S') = F\left\{\frac{\omega'_{A1}\,\omega'_{A2} + (S')^2}{S'(\omega'_{A2} - \omega'_{A1})}\right\}$$

and symmetrical passbands

$$0 < \omega'_{A1} \leq \omega' \leq \omega'_{A2}$$

and

$$-\omega'_{A2} \leq \omega' \leq -\omega'_{A1} < 0$$

and will be denoted by B and -B respectively.

In carrying out the present design procedure, it will be necessary eventually to identify the roots and poles of $F_{bp}(S')$. The voltage transfer function F(S) for the normalized lowpass filter is ordinarily prescribed by means of its roots and poles, and it is advisable to transform this function factor by factor in order to be able to determine the roots and poles of $F_{bp}(S')$. Thus each factor $S - S_o$ transforms into a rational fraction as follows:

$$S - S_o \quad \frac{(S' - r^+)(S' - r^-)}{S'}$$

where

$$r^{\pm} = \frac{(\omega'_{A2} - \omega'_{A1})S_o}{2} \pm \sqrt{\frac{[(\omega'_{A2} - \omega'_{A1})S_o]^2}{4} - \omega_{A1}\omega_{A2}}$$

and

$$p = 0 .$$

Since $F_{bp}(S')$ is real on the real axis, its roots and poles will occur in conjugate pairs, and the behavior of the filter in the region $\omega' > 0$ that contains the passband B will be due primarily to those roots and poles that lie in the upper half-plane. Conversely, the behavior of the filter in the region $\omega' < 0$ that contains the passband -B will be due primarily to the roots and poles of $F_{bp}(S')$ that lie in the lower half-plane.

Discarding the roots and poles of $F_{bp}(S')$ that lie in the lower half-plane creates a complex voltage transfer function that represents a filter with only the single passband B. Conversely, discarding the roots and poles in the upper half-plane results in a complex voltage transfer function that represents a filter with only the single passband -B.

This method can be used to generate a single passband filter, provided that the passband does not overlap $\omega' = 0$. If $\omega' = 0$ is overlapped and $\omega'_{A2} = -\omega'_{A1}$, then a single real lowpass filter will be sufficient. The case where $\omega' = 0$ is overlapped and $\omega'_{A2} \neq -\omega'_{A1}$ will be discussed later.

The single passband filter can be normalized in different ways, resulting in several different forms (see Figure A2). The form shown in Figure 2(b) has been normalized to the average value in the passband.

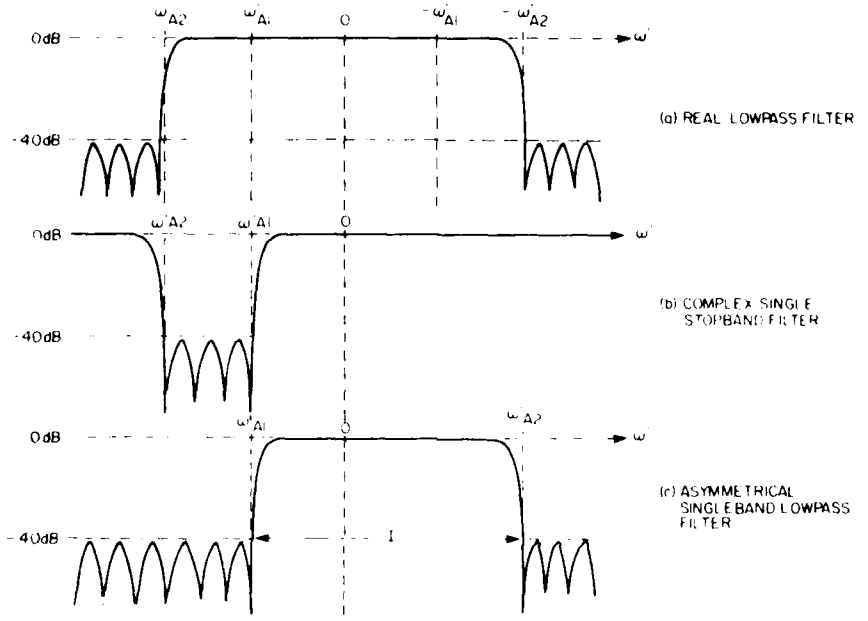

Figure A2. Power Transfer Functions of Filters Used to Realize an Asymmetrical Single-Band Lowpass Filter. Filter (a) cascaded with filter (b) produces filter (c)

A3. TRANSFER FUNCTIONS FOR SINGLE STOPBAND COMPLEX FILTERS

The transformation

$$S \quad \frac{\Omega_s(\omega'_{A2} - \omega'_{A1})S'}{\omega'_{A1}\,\omega'_{A2} + (S')^2}$$

converts the normalized lowpass filter with voltage transfer function F(S) into a bandstop filter with voltage transfer function

$$F_{bs}(S') \quad \pm \left\{ \frac{\Omega_s(\omega'_{A2} - \omega'_{A1})S'}{\omega'_{A1}\,\omega'_{A2} - (S')^2} \right\}$$

and symmetrical stopbands B and -B.

As with the bandpass filters, it is desired to identify the roots and poles of $F_{bs}(S')$, and to this end it is advisable to transform the voltage transfer function F(S) factor by factor in order to determine the roots and poles of $F_{bs}(S')$. Thus each factor $S - S_o$ transforms into a rational fraction as follows:

$$S - S_o \quad \frac{(S' - r^+)(S' - r^-)}{(S' - p^+)(S' - p^-)}$$

where

$$r^{\pm} \quad \frac{\Omega_s(\omega'_{A2} - \omega'_{A1})}{2S_o} \pm \sqrt{\frac{\{\Omega_s(\omega'_{A2} - \omega'_{A1})\}^2}{\{2S_o\}^2} - \omega'_{A1}\,\omega'_{A2}}$$

$$p^{\pm} \quad \pm j\sqrt{\omega'_{A1}\,\omega'_{A2}} \quad .$$

The zeros and poles of $F_{bs}(S')$ will as before occur in conjugate pairs, and the behavior of this filter in the regions $\omega' > 0$ which contains the stopband B is due principally to the roots and poles that lie in the upper half-plane. Also, the behavior of the filter in the region $\omega' < 0$ which contains the stopband -B is due principally to the roots and poles that lie in the lower half-plane.

Discarding the lower half-plane roots and poles in $F_{bs}(S')$ creates a complex voltage transfer function with only the one stopband B. Conversely, discarding the roots and poles of $F_{bs}(S')$ that lie in the upper half-plane creates a complex voltage transfer function with only the one stopband -B.

This procedure can be applied as long as the desired stopband does not include $\omega' = 0$. If the desired stopband contains $\omega' = 0$ and the interval is symmetric with respect to $\omega' = 0$, then a real lowstop filter will be the solution. The design of filters for asymmetrical intervals including $\omega' = 0$ is discussed below.

A4. TRANSFER FUNCTIONS FOR SPECIAL CASES

Assume $\omega_2 > 0$, $\omega_1 < 0$ and $\omega_2 > -\omega_1$; then $\omega'_{A2} > 0$, $\omega'_{A1} < 0$, $\omega'_{A2} > -\omega'_{A1}$ and the interval I given by $\omega'_{A1} < \omega' < \omega'_{A2}$ is asymmetrical and contains $\omega' = 0$ (see Figure A2(c)). The transfer function for a complex bandpass filter with bandpass I can be generated by multiplying the transfer function for a real lowpass filter with passband $-\omega'_{A2} < \omega' < \omega'_{A2}$ by the transfer function for a complex bandstop filter with stopband $-\omega'_{A1} < \omega' < \omega'_{A1}$ (see Figure A2). The transfer function for a complex bandstop filter with stopband I (see Figure A3(c)) can be generated by multiplying the transfer function for a real lowpass filter with stopband $-\omega'_{A1} < \omega' < \omega'_{A1}$ by the transfer function for a complex bandstop filter with stopband $-\omega'_{A2} < \omega' < \omega'_{A2}$ (see Figure A3).

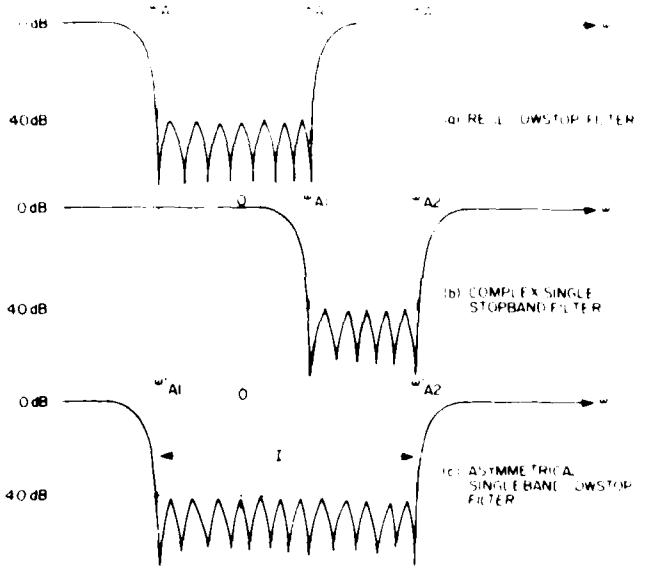

Figure A3. Power Transfer Functions of Filters Used to Realize an Asymmetrical Single-Band Lowstop Filter. Filter (a) cascaded with filter (b) produces filter (c)

If $\omega_2 > 0$, $\omega_1 < 0$, and $\omega_2 > -\omega_1$, then $\omega'_{A2} > 0$, $\omega'_{A1} < 0$, and $\omega'_{A2} > -\omega'_{A1}$ and the interval I given by $\omega'_{A1} < \omega' < \omega'_{A2}$ is asymmetrical and contains $\omega' = 0$. Procedures similar to those described above can be used to produce transfer functions for complex bandpass or bandstop filters with I as the passband or stopband.

A5. DIGITAL FILTER REALIZATION

Whether bandpass or bandstop, each of the voltage transfer functions of the single-band filters created by the methods described above is of the form of a ratio of polynomials in S', the coefficients in general, being complex. The generating function $G(Z)$ for producing the digital realization of a given voltage transfer function $F(S')$ is obtained by means of the transformation

$$S' = \frac{Z - 1}{Z + 1} .$$

This transformation maps the imaginary axis in the S' plane onto the boundary of the unit circle in the Z plane. In particular, it maps the points $S' = j\omega'_{A1}$ and $S' = j\omega'_{A2}$ into the points $Z = e^{j\omega'_1 T}$ and $Z = e^{j\omega_2 T}$ respectively. Thus

$$G(Z) = F\left\{\frac{Z - 1}{Z + 1}\right\}$$

and $G(Z)$ will be a ratio of polynomials in Z. The coefficients of these polynomials determine recursive forms of digital realizations of $F(S')$.[A1]

A6. IMPROVED DESIGN PROCEDURE

An improved design procedure for deriving digital filter [illegible] for single-band bandpass or bandstop filters has been developed. [illegible] method, the normalized lowpass filter is selected as before. [illegible] filter, and the bandpass or bandstop filter is obtained by the S' plane [illegible] plane. The results are specified in terms of [illegible] A. Numerical procedures are used for [illegible] and the call for [illegible] Typically, [illegible]

[illegible] $F(S')$ [illegible]

where

$$\omega'_{\Delta} = \tan \frac{\omega_2 - \omega_1}{4} T .$$

This produces a voltage transfer function $F_{bp}(S')$ for a lowpass filter with passband $-\omega'_{\Delta} < \omega' < \omega'_{\Delta}$.

The transformation

$$S' = \frac{Z' - 1}{Z' + 1}$$

converts $F(S')$ to a generating function in the Z' plane for a lowpass filter with passband

$$-\frac{\omega_2 - \omega_1}{2} < \omega < \frac{\omega_2 - \omega_1}{2} .$$

The transformation

$$Z' = Z e^{-j(\omega_1 + \omega_2)T/2}$$

rotates the center of the lowpass filter to the center of the bandpass filter at $(\omega_1 + \omega_2)/2$. The generating function is then given by

$$G_{bp}(Z) = F\left\{ \frac{1}{\omega'_{\Delta}} \cdot \frac{Z e^{-j(\omega_1 + \omega_2)T/2} - 1}{Z e^{-j(\omega_1 + \omega_2)T/2} + 1} \right\} .$$

For bandstop filters with [illegible] $F(S)$ [illegible]

$$= \frac{\omega'_{\Delta}}{S'}$$

[illegible]

$$= \frac{1}{1} \frac{S'}{} [illegible]$$

[illegible]

$$S' = \frac{Z' - 1}{Z' + 1}$$

and

$$Z' = Z e^{-j\left\{\frac{(\omega_1 + \omega_2)T}{2}\right\}}$$

as before, shift the Z plane and rotate the stopband of the lowstop filter to the proper location. The generating function $G_L(Z)$ is then given by

$$G_L(Z) = 1 \left\{ [illegible] \right\} .$$

A7 CONCLUSIONS

[illegible] method of deriving the generating function, further choices remain [illegible] of the IIR recursive-type digital procedure to be used in the realization of the filter. For the NEMRAD tests, the application of the "direct" form[A1] led to a digital realization that was highly sensitive to the accuracy of the constants involved. It was later determined that the "cascaded canonical" form[A1] was much superior to the "direct" form as it produces very satisfactory filter reproduction with much reduced sensitivity to the accuracy of the constants.

Many NEMRAD receiver patterns were calculated using the transfer functions [illegible] filters derived [illegible] C04 type [illegible] realized filters [illegible]. The [illegible] results were reasonable, but [illegible]. Plots [illegible] shown [illegible] filter pulses, [illegible] NEMRAD [illegible] and [illegible] IIR

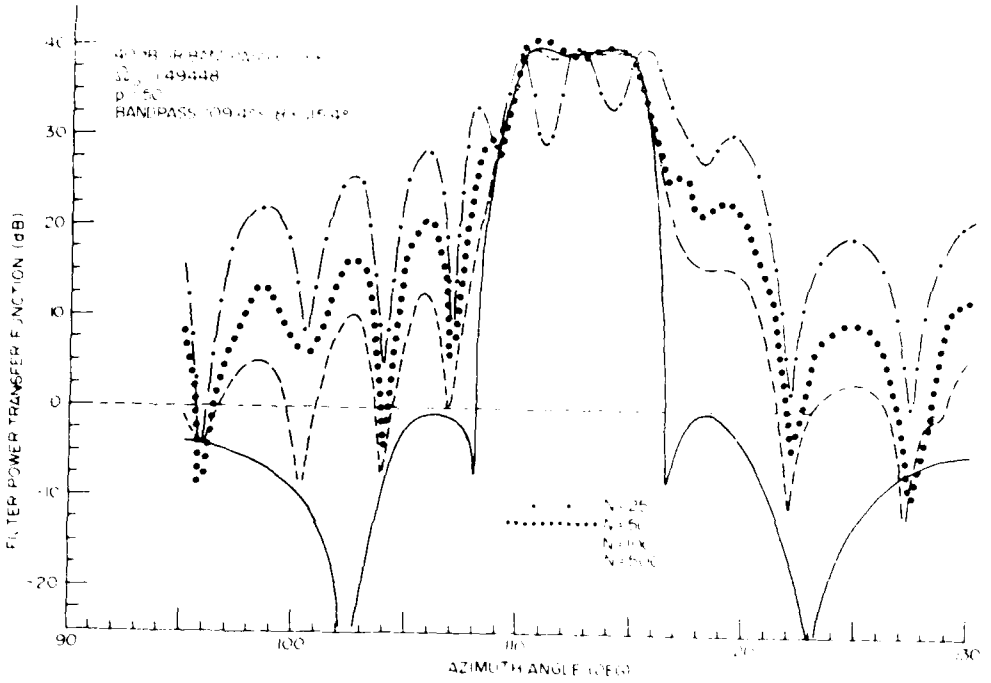

Figure A4. IIR Digital Filter Response Times

Appendix B

Complex Nonrecursive Finite Impulse Response
FIR Digital Filters

B1. FREQUENCY SAMPLING DESIGN METHOD

[illegible]

[illegible]

[illegible]

[illegible] in the passband.

It is the nature of digital filters that their response functions are periodic in frequency with period equal to the sampling rate, in this case the NEMRAD pulse repetition frequency. Choosing the prf greater than or equal to twice the maximum expected clutter Doppler frequency insures that for a single passband (or stopband) digital filter, there is only one passband (or stopband) within the clutter Doppler frequency interval. For the NEMRAD truck experiment, the prf is 1333 Hz [illegible] is always exactly twice the maximum clutter Doppler frequency of 945.2 Hz.

B2. MODIFICATIONS TO PRODUCE COMPLEX FILTER AND CASCADING

To achieve a complex single passband filter of the type needed for NEMRAD, a real lowpass FIR filter of the desired bandwidth and discrimination is designed and then rotated in the z plane to position the passband at the desired center frequency. For a single stopband filter, a real lowpass FIR filter whose reject region has the desired stopband width is designed and then rotated in the Z plane by the amount necessary to locate the stopband at the desired center frequency. The Z plane rotation needed for the stopband filter is essentially that which corresponds to the frequency difference between half the pulse repetition frequency (prf/2) and the Doppler clutter frequency at the center of the antenna transmit beam.

The action of an n-point bandpass FIR filter, together with an n-point bandstop FIR filter, can be achieved by cascading to form a single (2n-1) point FIR filter. For FIR filters with n = 17, 33, or 65, the response time is far less than for the IIR filters described earlier. For this reason, cascaded FIR filters were used on all subsequent investigations.

In the work that follows, FIR filters are designated according to their design. Figure B1 shows the design of a 33-point FIR bandpass with 5 points in its bandpass and 2 transition points, T1 and T2. The designation code for this filter, FBP33-5-2, translates as follows:

BP		bandpass filter (BS = bandstop filter)
33	NP	total number of points in the filter
5	NBW	measure of width of the passband (number of points in the passband = 2·NBW - 1
2	NT	number of transition points.

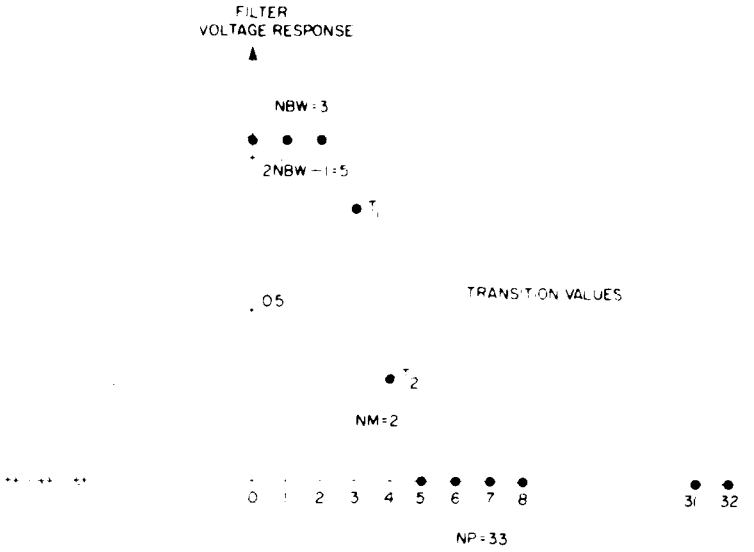

Figure B1. Specification of Filter Response Values for a BP33-3-2 FIR Filter

Table B1 shows some of the filters that were used in the theoretical investigations associated with NFMRAD.

Table B1. FIR Filters Used in NFMRAD Investigation

Bandpass Filters	Bandstop Filters
BP15-1-1	BS15-7-1
BP33-1-1	BS33-12-1
BP33-2-1	BS33-13-1
BP33-3-2	BS33-14-1
BP65-3-1	BS65-25-1
BP65-3-2	

Appendix C

Control Panel Operational Range Equations
Range Cell Width = 131.15 ft (40 m)
Range Coverage ≃ 2100 ft (640 m)

Figure C1 depicts the three operational range modes of the radar: NEGATIVE, SHORT, and LONG. The position of switches E and F select one of the radar range modes as defined in Table C1.

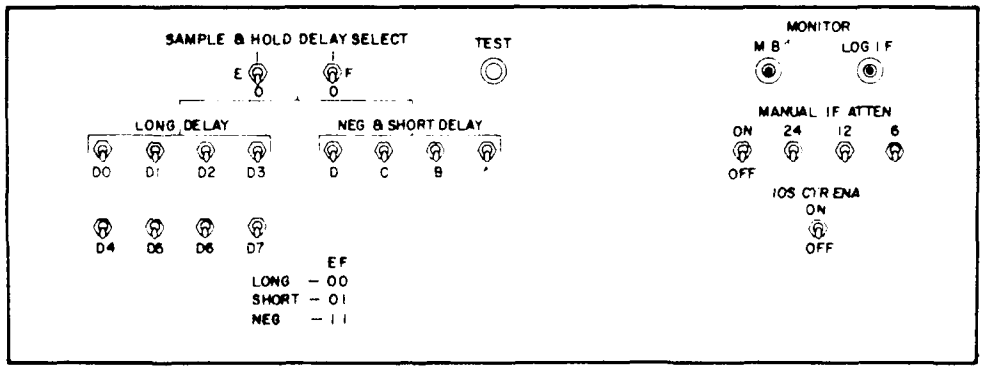

Figure C1. Radar Control Panel

Table C1. Radar Operating Range Mode

	E	F
LONG	0	0
SHORT	0	1
NEGATIVE	1	1

Equations (C1), (C3), and (C5) express the radar search range as a function of range bin (RB) and control panel configuration ($DCBA_{10}$, D7, etc.). The radar operational range mode is determined by the position of control panel switches E and F.

C1. LONG DELAY RANGE EQUATION

Equation (C1) expresses radar search range (γ) as a function of D0, D1, ... D7 control panel switch position, and the range bin (RB) of interest when in the LONG delay range mode. D_{set} is the control panel switch (D7, D6, D5, ... D0) set during radar operation. To calculate γ when in the LONG delay range mode: Let D7 = 7, D6 = 6, D5 = 5 ... D0 = 0, and RB is an integer representing the range bin of interest such that $1 \leq RB \leq 16$.

LONG Delay Range Equation

$$\gamma = 65.5763(15(D7-D_{set}) + 10 + 2\ RB)\ ft - 517.25\ ft \qquad (C1)$$

The time delay (Δt) between the transmitter MAIN BAND and the radar 16-bit SAMPLE command is given by Eq. (C2).

LONG Delay Time Equation

$$\Delta t = \frac{2}{15\ MHz}(15(D7-D_{set}) + 10 + 2\ RB) \qquad (C2)$$

C2. SHORT DELAY RANGE EQUATION

Equation (C3) expresses radar search range (γ) as a function of A, B, C, D control panel switch positions and the range bin (RB) of interest when in the SHORT delay range mode. Control switches A, B, C, D are binary weighted when calculating γ as shown in Table C2.

Table C2. $DCBA_{10}$ Equivalent for Range Calculations

Control Panel Switch Position D C B A	Base 10 Equivalent
0 0 0 0	0
0 0 0 1	1
0 0 1 0	2
0 0 1 1	3
.	.
.	.
.	.
1 1 1 1	15

SHORT Delay Range Equation

$$\gamma = 131.1525(16.375 + RB - DCBA_{10}) \text{ ft} - 517.25 \text{ ft} \quad \text{(C3)}$$

Δt may be calculated as expressed in Eq. (C4).

SHORT Delay Time Equation

$$\Delta t = \frac{4}{15 \text{ MHz}} (16.375 + RB - DCBA_{10}) \quad \text{(C4)}$$

C3. NEGATIVE DELAY RANGE EQUATION

Equation (C5) expresses the radar search range (γ) as a function of A, B, C, D and RB when in the NEGATIVE delay range mode. A negative result from Eqs. (C5) and (C6) indicates the 16-bit SAMPLE command of interest occurs before the transmitter MAIN BANG. A positive result indicates the SAMPLE command occurs after the MAIN BANG.

NEGATIVE Delay Range Equation

$$\gamma = 131.1525 (1/2 + RB - DCBA_{10}) \text{ ft} - 517.25 \text{ ft} \quad \text{(C5)}$$

NEGATIVE Delay Time Equation

$$\Delta t = \frac{4}{15 \text{ MHz}} (1/2 + RB - DCBA_{10}) \quad \text{(C6)}$$

Appendix D

ADC Alignment Procedures

The purpose of this procedure is to ensure that the ADC assembly is calibrated and will not introduce additional errors into the receiver/processor system. All comments and adjustments will be made with reference to the I side of the assembly; however, they apply equally to the Q side.

Recommended Equipment

Dual trace oscilloscope
Signal generator
0-5 V dc variable power supply
LED display box (or eight-channel logic analyzer)
BNC to SMA adapters as required
Digital multimeter (DMM)
Two 18-wire ribbon connectors (MI PAC 3552040-01 or equivalent).

D1. 8-BIT ADC ALIGNMENT

D1.1 Initial Setup

Connect an 18-wire cable from the 4-bit ADC power distribution block to the 8-bit ADC assembly under test. The cable must be connected to the 8-bit ADC board row C, pins 19-36. Ensure the black white pair of wires at the ADC board (pins 19-20) is connected to the 4-bit power distribution block (pins 1-2 or 19-21).

Reversing the supply sequence can cause serious damage to the ADC (refer to Figure D1).

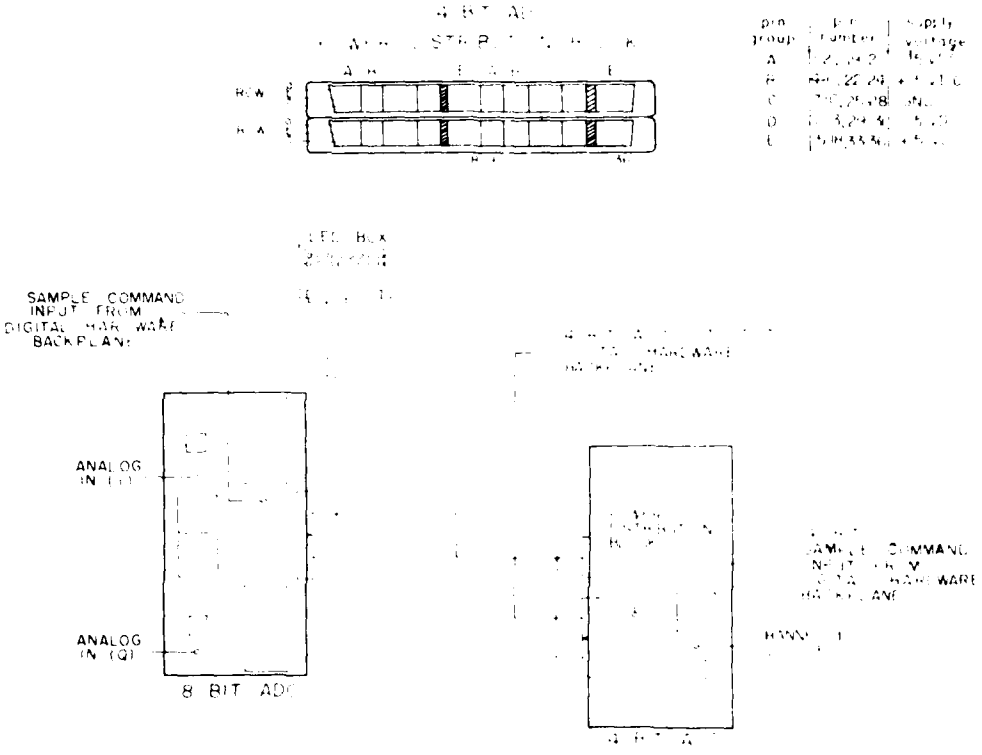

Figure D1. 8-Bit ADC Alignment Configuration

Connect a coax cable to the 8-bit SAMPLE command input port from the receiver digital hardware backplane (refer to Figure D2).

Connect the dual trace scope as follows:

1. Trace "A" to the analog input
2. Trace "B" to the input of the ADC (pins 17 and 18)

(Refer to Figure D3(a) for pin locations.)

Connect the signal generator to the analog input port of the ADC under test.

Turn rack power on.

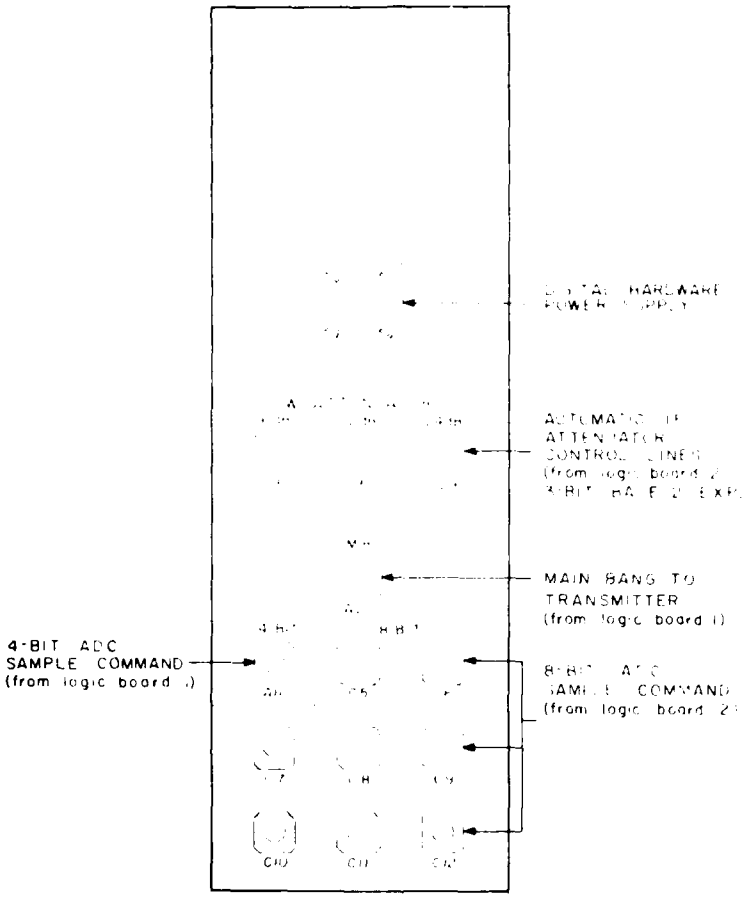

Figure D2. Receiver Digital Hardware
(Backplane Connector Panel)

D1.2 ADC Assembly Gain Adjustment (Refer to Figure D3(b))

Ensure the analog input (signal generator) is set for 100 mV peak to peak at 250 KHz as measured with the scope (trace A).

Monitor the input to the ADC (trace B) and adjust the GAIN pot of the wide-band amplifier for a gain of 6.3 (630 mV) output.

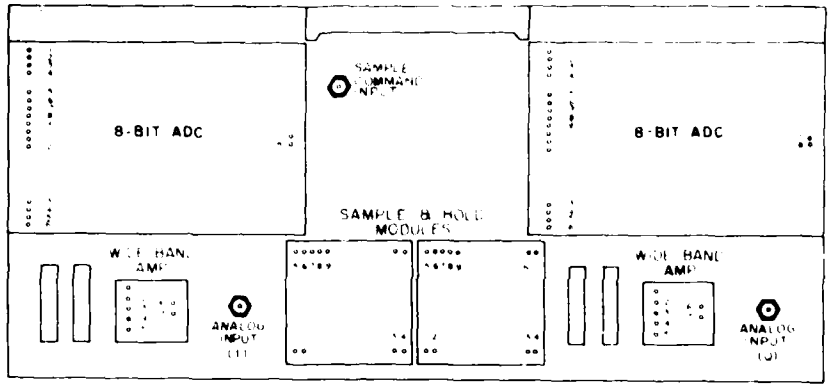

(a) Pin Locations (Top View)

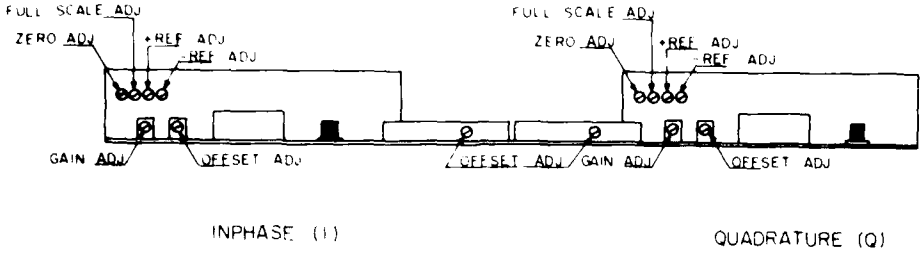

(b) Calibration Adjustments (Side View)

Figure D3. 8-Bit ADC Assembly

D1.3 ADC Assembly Offset Adjustment (Refer to Figure D3(b))

The purpose of this adjustment is to ensure the analog input has a 0 V dc offset (with respect to ground) as measured with an oscilloscope. Any dc offset to the analog signal will cause the ADC output to shift a proportional amount and invalidate any gathered data.

Monitor scope trace A and adjust the analog input (signal generator) for 0 V dc offset.

Remove the trace B probe from the ADC (pins 17 and 18) and connect it to the sample and hold unit input (pins 10 and 11). (Refer to Figure D3(a) for pin locations.)

Monitor the scope (trace B), and adjust the OFFSET pot of the wide-band amplifier for 0 V dc offset.

[illegible]

DL.4 8-Bit ADC Output Calibration Setup (Refer to Figures D4 and D5)

[illegible] (Refer to Figure D4 for location of ADC assembly. Refer to Figure D5 for location of ADC output test points. All [illegible] ADC output test points. All [illegible] the off-state [illegible].)

Connect an 18-inch cable from the LED display box to J[illegible] on the ADC assembly to be calibrated (J2, pins 1-10). Ensure that the [illegible] both ends of the cable is connected to pins 1 to 1. (This [illegible] output from both I and Q sides; however, calibration [illegible] to the I side only.)

Connect +5 V dc to the LED display box using a 48-in. [illegible] BNC connector on one end and alligator clips on the other. Route the alligator clips through the ADC deck to the rear of the rack. Connect the center [illegible] clip to +5 V dc on the backplane of the receiver digital hardware and the [illegible] to ground. Connect BNC connector to the LED display box.

Remove both scope probes and the signal generator from the ADC assembly. Remove the sample and hold unit from the side to be calibrated.

Connect the 0-5 V dc variable power supply to the input of the ADC (pins 17 and 18).

Connect the DMM to the input of the ADC (pins 17 and 18).

Turn rack power on. Allow 10-min warmup time for the ADC to stabilize.

DL.5 8-Bit A/D Adjustments (Refer to Figure D3(b) for Location of Pots)

Monitoring the DMM, adjust the variable power supply to -1.115 V dc.

Adjust the -REF ADJ pot until the LED display indicates the following:

(red LED's represent I side, Green LED's represent Q side)

N7, N6, N5 should be on

N4 should be blinking.

As the voltage is decreased to -1.110 V dc, N4 should be on, and as the voltage is increased to -1.120 V dc, N4 should be off.

Monitoring the DMM, adjust the variable power supply to -1.125 V dc.

Adjust the +REF ADJ pot until the LED display indicates the following:

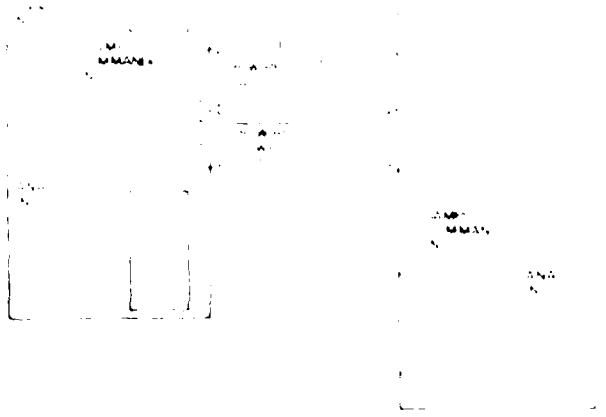

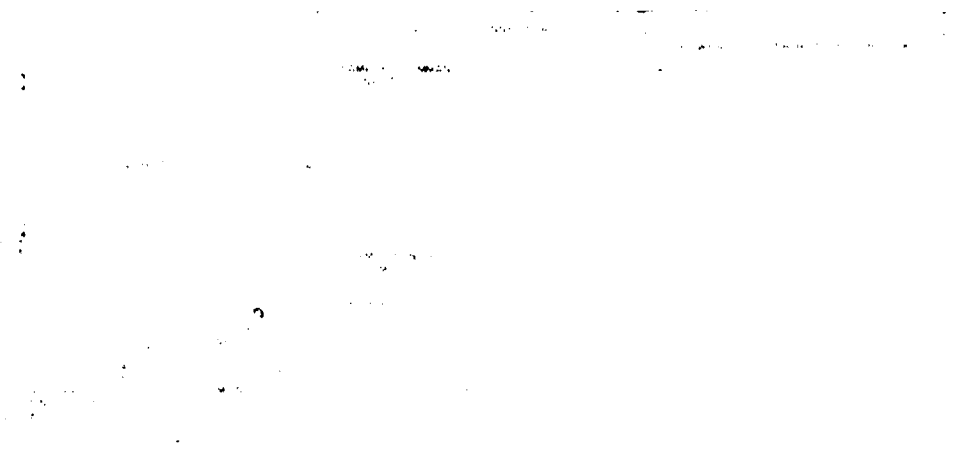

Figure D2. 4-Bit ADC Assembly

Install analog test signal cable to 20-pin connector J1.

Monitor scope trace A and adjust the offset control for 0 V dc offset (AGND respect to ground).

Monitor the scope trace B and adjust the sample and hold offset control for 0 V offset (AGND respect to ground).

D2.3 4-Bit ADC Gain Adjustment

Remove shorting cap from the 4-bit ADC analog input test.

Connect a signal generator to the analog input. Ensure that the generator is set for 2.50 kHz at 100 mV peak to peak.

Monitor scope trace A and adjust the signal generator for 0 V dc offset.

Monitor scope trace B and adjust the gain control for 0.87 (87 mV peak to peak).

D2.4 4-Bit ADC Output Calibration (Refer to Figures D4 and D6)

In the following procedure, the LED Display Box is used to allow visual monitoring of the actual ADC output. An oscilloscope or logic analyzer may be used if desired (refer to Table D1 for the 4-bit ADC output representation).

Turn clock power off.

Disconnect the oscilloscope probes and signal generator from the 4-bit ADC test jig.

Connect an 18-wire cable from the ADC output connector (rear B pins 1-18) to the LED Display Box (rear B pins 1-18).

Table D1. 4-Bit ADC Output

Analog Input (volts)	Digital Output
-2.400	1111
-1.920	1100
-1.280	1000
-0.160	0001
0.000	0000

(Note: The most negative analog input voltage that is still within the full scale output)

Connect a 5 Vdc to the LED display box using a 40-in. piece of wire with a BNC connector (male) connected and alligator clips on the other. Run the red and white alligator clips through the ADC 5 V to the rear of the rack. Connect the center conductor clip to ground. Connect the BNC (male) connector to the LED display box.

Remove the cover and locate the 4-bit ADC assembly.

Connect the 0-5 V dc variable power supply to the input of the ADC (pins 17 and 18).

Connect the DVM to the input of the ADC (pins 17 and 18).

Turn on the power and allow 10 min for warm-up time.

Without the DVM, adjust the variable power supply to -2.400 V dc.

Adjust the -REF pot until the LED display indicates the following:

S7, S6, S5, S4 should be on

(the 4-bit ADC uses only these four LED's).

Monitoring the DVM, adjust the variable power supply to -1.920 V dc. The LED display should indicate the following:

S7, S6, S5, S4 shall be off,

(since the 4-bit ADC is not a bipolar unit, only the -REF adj is available).

Turn the power off and remove all test equipment.

D3. 4-BIT ADC DC BIAS ADJUSTMENT (Refer to Figure D7)

The purpose of this procedure is to ensure the output of the 4-bit ADC is such that the automatic attenuators begin switching in at the correct power level. If the attenuators switch in too late, the input to the 8-bit ADC's may saturate, causing erroneous data.

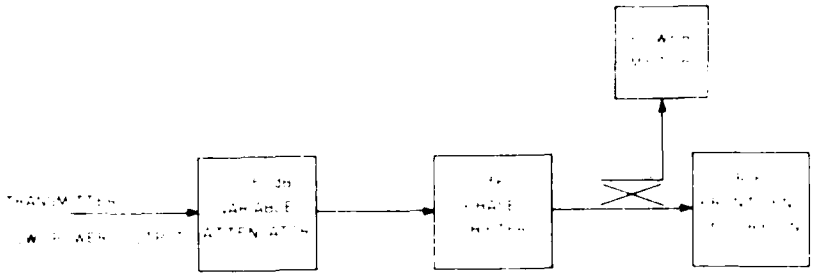

Figure D7. 4-Bit ADC Bias Adjustment

Additional Equipment:

Waveguide attenuator (FXR MDL No. [illegible] or equivalent)

Waveguide phase shifter (H.P MDL No. [illegible] or equivalent)

Waveguide sections as required.

Power meter and thermistor mount.

1. Configure the ADC deck for test equipment as follows:

   a. Remove all test equipment.

   b. Reinstall all assemblies and cables removed in previous procedures.

   c. Ensure that all SAMPLE [illegible] and cables are connected.

   d. Ensure that all ADC output [illegible] are connected. (See Table D2 for listing).

   e. Ensure that all analog input [illegible] are connected. (If the I and Q cables for any ADC are removed, the data will be invalid.)

2. Configure the transmitter for test [illegible]:

   a. Ensure both waveguide [illegible] are set for [illegible] (0-50 dB test position).

   b. At the rear of the transmitter deck, [illegible] install additional waveguide sections as required [illegible] Figure D7.

   c. Disconnect the diode switch driver [illegible] switches inside the transmitter (this will [illegible] the CW mode).

   d. Set the 0-50 dB variable attenuator for 0 dB. Set the [illegible] attenuator for 50 dB.

3. Turn power on for both transmitter and receiver [illegible]. Allow [illegible] warmup time.

   a. Adjust the transmitter front panel attenuator until [illegible] (1 mW) is obtained on the power meter. Note the [illegible]. (If 0 dBm cannot be obtained, note the power [illegible] attenuation. This will be used at a later [illegible] power level.)

Table D2. ADC to Digital Hardware Backplane Cable List (Refer to Figure 32 for card locations)

From	To
4-bit ADC	Receiver Hardware
row A, B pins 1-18	Card 2 row B pins 1-18
8-bit ADC	
Bit 1 row B 1-18	Card 4 row A pins 1-18
Bit 2 row B 1-18	Card 5 row A pins 1-18
Bit 3 row B 1-18	Card 6 row A pins 1-18
Bit 4 row B 1-18	Card 7 row A pins 1-18
Bit 5 row B 1-18	Card 9 row A pins 1-18
Bit 6 row B 1-18	Card 10 row A pins 1-18
Bit 7 row B 1-18	Card 11 row A pins 1-18
Bit 8 row B 1-18	Card 12 row A pins 1-18

b. Adjust the 0-50 dB attenuator for 50 dB, and the front panel attenuator for maximum attenuation.

c. Connect the oscilloscope to the IF front end as follows (refer to Figure E1(a) for location IF front end):

1. Trace A to the 6-dB test point.
2. Trace B to the 12-dB test point.

d. Determine the front panel attenuator setting to be used (refer to the power reading/attenuator setting taken in step 3).

1. If a 1 mW power level was obtained, add the attenuator setting to -75 dB to obtain the proper value, that is, attenuation setting

$$\begin{array}{r} 2.7\ \text{dB} \\ +75\ \text{dB} \\ \hline 77.7\ \text{dB} \end{array}$$

will be the total system attenuation to be inserted via the 0-50 dB attenuator and the front panel attenuator (0-50 dB set to 50 dB and the front panel attenuator set to 27.7 dB).

2. If a 1 mW power level was not obtained, take the power level reading [illegible] of front panel attenuation and subtract from the total attenuation desired, that is, power level reading at -3.2 dBm.

$$\begin{array}{r} 75.\ .3 \\ -3.2\ \text{dBm} \\ \hline 71.8\ \text{dB} \end{array}$$

total system attenuation.

After the proper attenuation level has been set, monitor the scope and adjust the 4-bit ADC dc bias pot (refer to Figure D6) until the 6-dB IF attenuator line just begins to switch in. Ensure the manual attenuation control on the radar control panel is in the OFF position (*refer to Figures C1 and E1(a) for location.*

Note: By monitoring the 6- and 12-dB IF attenuator lines, you ensure that 6 dB is being calibrated.

D4. DYNAMIC SYSTEM CHECK (Refer to Figure D8)

The dynamic test for each of the I and Q sides is the same for all eight channels. Channel 1Q will be described because of its accessibility.

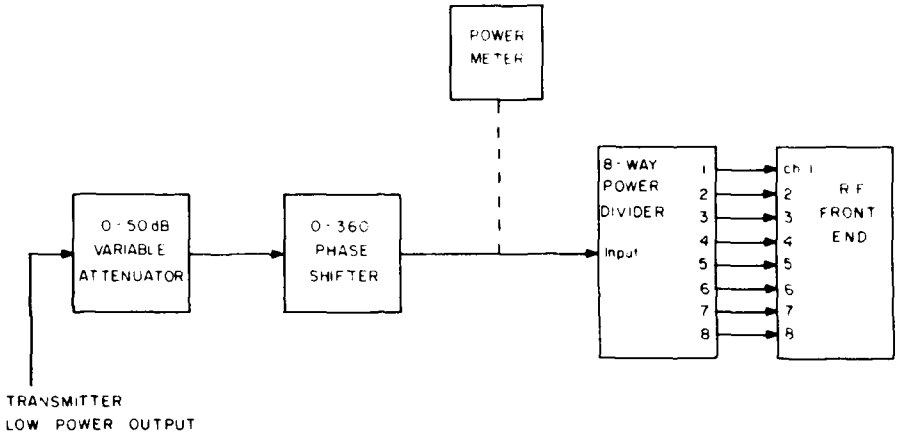

Figure D8. ADC Dynamic Test Configuration

Configure the transmitter for TEST, as outlined in Section D3.2.

Remove the RF input cable from the channel 1 RF input port, and connect this cable end to an eight-way power divider (MERRIMAC PDM-82).

Using eight coax cables (36-in. long), connect each of the output ports of the power divider to the input ports on the RF front end.

In order to determine the saturation point for each of the ADC unit, it may be necessary to measure the total insertion loss of the eight-way power divider from the input cable to each of the eight output cables. This may be accomplished using a network analyzer. (Note: Although use of the eight-way power divider is not mandatory, it does shorten the time required to perform checks on all 16 ADC's.

If not used, the RF input cable must be moved from channel to channel as the test progresses.)

1. On the radar control panel, set the IF attenuator switches to 0 dB of manual IF attenuation.

2. Connect an oscilloscope to the sample and hold input pins (10 and 11) of the ADC under test. (Refer to Figure D3(a) for pin locations.)

3. Set the 0-50 dB attenuator to 50 dB of attenuation. Set the transmitter front panel attenuator to 20 dB of attenuation.

4. Turn rack power on (both transmitter and receiver racks). Allow 10 min for warmup. Turn the transmitter "offset oscillator" on.

5. Monitoring the scope, adjust the $0\text{-}360^{\circ}$ phase shifter for the largest possible signal level (with respect to ground).

6. Set the transmitter front panel attenuator to 50 dB. On the radar control panel, set the auto/manual IF attenuator switch to AUTO.

7. Monitoring the oscilloscope, begin decreasing the amount of attenuation via the front panel attenuator. At the point where the 6 dB IF attenuator begins to switch in, measure the signal level (reading should be less than 1.25 V peak).

8. Continue decreasing the attenuation on the front panel attenuator. As each succeeding IF attenuator begins switching in, note the signal level.

(Note: The full range of 42 dB of IF attenuation may be achieved in the following manner:

After the front panel attenuator has been adjusted through its full range (to 0 dB), set the front panel attenuator to 50 dB and the 0-50 dB attenuator to 0 dB of attenuation. This will give the system another 50 dB of signal range.).

9. Repeat steps 1. through 7. for the remaining 15 A/D sides.

At no point should the signal level measured in the automatic mode of IF attenuation exceed 1.25 V peak. If the signal level does exceed this amount, the ADC's may saturate.

10. If the signal level for any one of the 16 ADC's exceeds 1.25 V peak, repeat the 4-bit ADC bias adjustment procedure outlined in Section D3.

Appendix E

System Component Identification

The purpose of Appendix E is to identify the equipment located in each of the four equipment racks that make up the NFMRAD (AMTI) systems. As each level is identified within an equipment rack, reference will be made to the chapter within this report and/or other documentation for functional descriptions.

E1. RECEIVER (Refer to Figure E1(a))

level 1	
Receiver IF	Ref. Section 3.2.4
level 2	
Radar Control Panel	Ref. Appendix C
level 3	
Receiver Digital Hardware	Ref. 4.1, 4.4 through 4.7
level 4	
Analog to Digital Converter (ADC) Deck	Ref. 4.2, 4.3, Appendix D
level 5 and 6	
Power Supplies	none

level 7

Rack Blower	none

E2. TRANSMITTER (Refer to Figure E1(b))

level 1

Delay Lines	Ref. 3.2.3

level 2

Receiver Front End	Ref. 3.2.2
Transmit/Receive Array	Ref. 2.2

level 3

Transmitter	Ref. 3.1
a. RF Sources	Ref. 3.1.1
b. Pulse Generation	Ref. 3.1.3
c. Pulse Generation	Ref. 3.1.3

level 4

Power Supplies	none

level 5

Traveling Wave Tube Amplifier (TWTA)	Ref. 3.1.4, also Instruction and Maintenance Manual for Instrumentation Traveling Wave Tube Amplifier Model No. 1277H03 TW1, Hughes Aircraft Co., Electron Dynamics Division, 3100 W. Lomita Blvd., Torrance, CA 90509

level 6

Rack Blower	none

E3. CSP 30 MINICOMPUTER (Refer to Figure E2(a))

level 1

Tri-Data Catrifile Unit	Ref. Cartrifile 20 Instruction Manual, Tri-Data, 800 Maude Ave., Mountain View, CA 94040

level 2

Control panel	Ref. CSPI Operation and Maintenance Manual, Doc. No. JP3000-000-04. CSPI, 40 Linnel Cr., Billerica, MA 01821

level 3

Upper Mainframe Cooling Fans	Ref. none

level 4

Mainframe/Card Nest	Ref. see level 2 above

level 5

Lower Mainframe Cooling Fans	Ref. none

level 6

Power Supplies	Ref. see level 2 above

E4. MAP ARRAY PROCESSOR (Refer to Figure E2(b))

level 1

Display Scope Tektronix Type 611	Ref. *Tektronix Operation and Maintenance* Manual, Type 611 Mod. 1620. Tektronix, Inc., P.O. Box 500, Beaverton, OR 97005

level 2

Hard Copy Unit Tektronix Mod. 4601	Ref. Tektronix Operation and Maintenance Manual Mod. 4601.

level 3

MAP Monitor Panel	Ref. Installation and Operation Booklet No. AS7130-000-01.

level 4

Expansion Power Supply	Ref. Operation Maintenance Manual AT 6000-004-PRE4.

level 5

MAP-300 Arithmetic Processor	MAP Programmer's Reference Manual

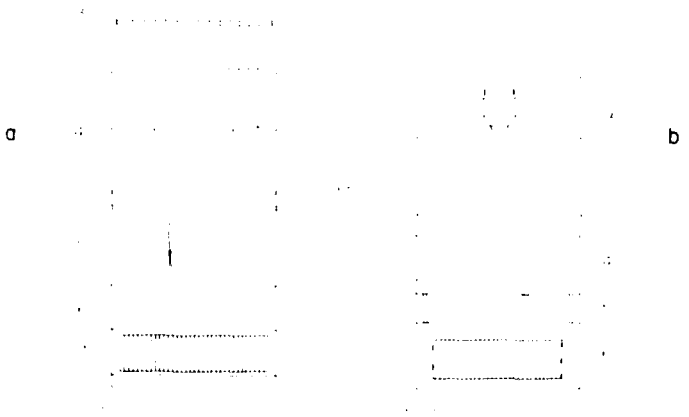

Figure E1. Receiver Transmitter Equipment Racks (a) Receiver, (b) Transmitter

MISSION
of
Rome Air Development Center

RADC plans and executes research, development, test and selected acquisition programs in support of Command, Control Communications and Intelligence (C^3I) activities. Technical and engineering support within areas of technical competence is provided to ESD Program Offices (POs) and other ESD elements. The principal technical mission areas are communications, electromagnetic guidance and control, surveillance of ground and aerospace objects, intelligence data collection and handling, information system technology, ionospheric propagation, solid state sciences, microwave physics and electronic reliability, maintainability and compatibility.

Printed by
United States Air Force
Hanscom AFB, Mass. 01731

END

DATE
FILMED

6-81

DTIC